Shaping of laser-accelerated ion beams for applications in high energy density physics

Formung von laserbeschleunigten Ionenstrahlen für Anwendungen in der Physik mit hoher Energiedichte
Zur Erlangung des Grades eines Doktors der Naturwissenschaften (Dr. rer. nat.)
Genehmigte Dissertation von Martin Metternich aus Hadamar
Tag der Einreichung: 24.01.2023, Tag der Prüfung: 15.02.2023

1. Gutachten: Prof. Dr. Markus Roth
2. Gutachten: Prof. Dr. Vincent Bagnoud
Darmstadt, Technische Universität Darmstadt

TECHNISCHE
UNIVERSITÄT
DARMSTADT

Physics Department
Institut für Kernphysik
Laser- und Plasmaphysik

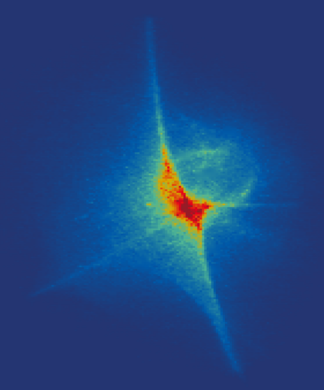

Shaping of laser-accelerated ion beams for applications in high energy density physics
Formung von laserbeschleunigten Ionenstrahlen für Anwendungen in der Physik mit hoher Energiedichte

Accepted doctoral thesis by Martin Metternich

Date of submission: 24.01.2023
Date of thesis defense: 15.02.2023

Darmstadt, Technische Universität Darmstadt

Bitte zitieren Sie dieses Dokument als:
URL: http://tuprints.ulb.tu-darmstadt.de/24395
Jahr der Veröffentlichung auf TUprints: 2023

Erklärungen laut Promotionsordnung

§ 8 Abs. 1 lit. c PromO

Ich versichere hiermit, dass die elektronische Version meiner Dissertation mit der schriftlichen Version übereinstimmt.

§ 8 Abs. 1 lit. d PromO

Ich versichere hiermit, dass zu einem vorherigen Zeitpunkt noch keine Promotion versucht wurde. In diesem Fall sind nähere Angaben über Zeitpunkt, Hochschule, Dissertationsthema und Ergebnis dieses Versuchs mitzuteilen.

§ 9 Abs. 1 PromO

Ich versichere hiermit, dass die vorliegende Dissertation selbstständig und nur unter Verwendung der angegebenen Quellen verfasst wurde.

§ 9 Abs. 2 PromO

Die Arbeit hat bisher noch nicht zu Prüfungszwecken gedient.

Darmstadt, 24.01.2023

M. Metternich

Kurzfassung

Ziel dieser Arbeit war die Erzeugung eines geeigneten Ionenstrahls für spezifische Anwendungen mit einer lasergetriebenen Ionenstrahlführung, welche im Rahmen der Laser Ion Generation Handling and Transport (LIGHT) Kollaboration an der GSI Helmholtzzentrum für Schwerionenforschung GmbH realisiert wurde. Zu diesem Zweck ist zunächst der Einfluss der Strahlformung auf die initialen Eigenschaften des lasergenerierten Ionenstrahls detailliert charakterisiert worden. Außerdem wurden Gleichungen hergeleitet, mit denen die erforderlichen magnetischen und elektrischen Feldstärken der Strahlführungskomponenten für die zu untersuchenden Anwendungen berechnet werden können. Mit diesen Erkenntnissen ist dann der optimale Aufbau der LIGHT Strahlführung für die folgenden drei Anwendungen ermittelt worden:

- Die Injektion des Ionenstrahls in das Schwerionensynchrotron SIS18 der GSI
- Die Erzeugung und Untersuchung von hohen Protonenflüssen
- Die Erzeugung eines geeigneten Ionenstrahls für die Messung des Bremsvermögens von dichten, hochionisierten Plasmen

Anschließend wurden die zu erwartenden Strahlparameter für diese Aufbauten durch numerische Simulationen bestimmt und experimentell überprüft.
Nach den numerischen Simulationen können mit dem derzeitigen Aufbau der LIGHT Strahlführung 3×10^8 Protonen mit einer Energie von 11,4 MeV in das Synchrotron SIS18 der GSI in einem Schuss injiziert werden. Da das Synchrotron mehr als 10^{10} Protonen aufnehmen kann, wurden auch Vorschläge zur Erhöhung der Teilchenzahl für diese Anwendung ausgearbeitet.
Im Hinblick auf die Erzeugung von hohen Protonenflüssen wurde in einer experimentellen Kampagne, die im Rahmen dieser Arbeit durchgeführt wurde, ein Protonenbündel mit $(7{,}72 \pm 0{,}14)$ MeV und einem Teilchenfluss von $(3{,}28 \pm 0{,}24) \times 10^8\,\mathrm{ns^{-1}\,mm^{-2}}$ erzeugt. Besonders hervorzuheben ist dabei die zeitliche Breite dieses Protonenbündels, die nur (742 ± 40) ps (FWHM) betrug. Außerdem ergaben die entsprechenden Simulationen zu diesem Experiment, dass das kreuzförmige Ionenstrahlprofil in gepulsten Hochfeld-Solenoid-Strahlführungen, welches auf dem Titelbild dieser Arbeit abgebildet ist, durch das Magnetfeld der Anschlusskabel der Solenoid-Magnete verursacht wird. Diese Ergebnisse sind in [Metternich et al., 2022] veröffentlicht worden.
Schließlich wurde die Erzeugung eines geeigneten Ionenstrahls für die Messung des Bremsvermögens von dichten, hochionisierten Plasmen untersucht und experimentell mit der LIGHT Strahlführung durchgeführt. Der resultierende Ionenstrahl hatte eine Energie von $(0{,}60 \pm 0{,}02)\,\mathrm{MeV\,u^{-1}}$ und eine zeitliche Breite von $(1{,}23 \pm 0{,}04)$ ns (FWHM). Darüber hinaus konnte abgeschätzt werden, dass $(2{,}0 \pm 0{,}6) \times 10^6$ Kohlenstoffionen dieses Bündels im geplanten Experiment den räumlich homogenen Bereich des zu untersuchenden Plasmas durchdringen werden, also drei Größenordnungen mehr Teilchen als bei vorherigen Messungen an der GSI bei einer vergleichsweise fast fünfmal kürzeren zeitlichen Bündelbreite. Die Messung des Bremsvermögens von dichten, hochionisierten Plasmen mit den in dieser Arbeit erreichten Strahlparametern sollte daher zu wesentlich geringeren Messunsicherheiten führen als bei den bisher durchgeführten Experimenten.

Abstract

The goal of this work was the generation of a suitable ion beam for specific applications with a laser-driven ion beamline, which was realized within the Laser Ion Generation Handling and Transport (LIGHT) collaboration at GSI Helmholtzzentrum für Schwerionenforschung GmbH. For this purpose, the influence of the beam shaping on the initial properties of the laser-generated ion beam has first been characterized in detail. In addition, equations have been derived to calculate the required magnetic and electric field strengths of the beamline components for the applications under investigation. These findings have then been used to determine the optimal setup of the LIGHT beamline for the following three applications:

- The injection of the ion beam into the heavy ion synchrotron SIS18 at GSI
- The generation and investigation of high proton fluxes
- The generation of a suitable ion beam for the measurement of the stopping power of dense, highly ionized plasmas

Subsequently, the expected beam parameters for these setups were determined by numerical simulations and verified experimentally.

According to the numerical simulations, the current setup of the LIGHT beamline can inject 3×10^8 protons with an energy of 11.4 MeV into the SIS18 synchrotron at GSI in one shot. Since the synchrotron can accommodate more than 10^{10} protons, proposals have also been elaborated to increase the number of particles for this application.

With respect to the generation of high proton fluxes, in an experimental campaign that was carried out as part of this work, a proton bunch with (7.72 ± 0.14) MeV and a particle flux of $(3.28 \pm 0.24) \times 10^8\,\mathrm{ns^{-1}\,mm^{-2}}$ was achieved. Of particular note is the temporal width of this proton bunch, which was only (742 ± 40) ps (FWHM). Furthermore, the corresponding simulations for this experiment revealed that the cross-shaped ion beam profile in pulsed high-field solenoid beamlines, which is shown on the cover of this thesis, is caused by the magnetic field of the connecting cables of the solenoid magnets. These results have been published in [Metternich et al., 2022].

Finally, the generation of a suitable ion beam for measuring the stopping power of dense, highly ionized plasmas was investigated and experimentally performed using the LIGHT beamline. The resulting ion beam had an energy of $(0.60 \pm 0.02)\,\mathrm{MeV\,u^{-1}}$ and a temporal width of (1.23 ± 0.04) ns (FWHM). Moreover, it could be estimated that $(2.0 \pm 0.6) \times 10^6$ carbon ions of this bunch will penetrate the spatially homogeneous region of the plasma under investigation in the planned experiment, i.e., three orders of magnitude more particles than in previous measurements at GSI with a temporal bunch width comparatively almost five times shorter. The measurement of the stopping power of dense, highly ionized plasmas with the beam parameters achieved in this work should therefore lead to much lower measurement uncertainties than in the experiments performed so far.

Contents

1. Introduction

Lasers have evolved rapidly since their discovery in 1960 [Maiman, 1960]. They are now firmly established in many sectors such as research, medicine, chemistry, construction, manufacturing and communication. In research this new source of coherent, intense light opened up totally new chances for investigations and the rising laser intensities from advanced techniques like Q-switching [McClung and Hellwarth, 1962] and mode-locking [Hargrove et al., 1964] made it possible to generate and study plasma states in the laboratories that can otherwise only be found in the stars of our universe.

With regard to the maximum achievable laser intensities, the next key innovation was the Chirped Pulse Amplification technique (CPA) [Strickland and Mourou, 1985], which was awarded with the Nobel Prize in 2018. With this technique, intensities higher than $10^{18}\,\mathrm{W\,cm^{-2}}$ became accessible and thus also the regime of relativistic laser-matter interactions. The irradiation of thin foil targets with such powerful laser pulses results in the generation of protons in the MeV range [Snavely et al., 2000; Hatchett et al., 2000; Clark et al., 2000; Maksimchuk et al., 2000] and established the new research field of laser-driven ion acceleration.

1.1. Laser-driven ion acceleration

The cause of the resulting ion acceleration are electrons that gain energy from the relativistic laser-matter interaction. Since the electrons are electrostatically confined to the target, they form a sheath at the targets rear side and the resulting electric field is strong enough to field ionize and accelerate the atoms at this position. This mechanism is designated Target Normal Sheath Acceleration (TNSA) because the ions are directed towards the normal of the targets surface [Wilks et al., 2001].

Since then, the mechanism has been extensively studied and proven to reliably provide multi-MeV ion bunches with a high particle flux and outstanding beam quality [Cowan et al., 2004; Hegelich et al., 2002; Roth et al., 2006; Nürnberg et al., 2009]. It therefore offers the potential to expand the scope of accelerators for applications and research [Cowan et al., 2004; Daido et al., 2012; Macchi et al., 2013]. This applies in particular for applications in High-Energy Density Physics (HEDP), in which they could be used

- as a direct driver in inertial confinement fusion [Roth et al., 2001],
- for generating warm dense matter via isochoric heating [Patel et al., 2003; Snavely et al., 2007; Dyer et al., 2008; Pelka et al., 2010],
- for the exploration of warm dense matter or hot plasma [Apiñaniz et al., 2021],
- as a new kind of ion source for conventional accelerators [Antici et al., 2011; Busold et al., 2014b],
- or as a pulsed neutron source [Roth et al., 2013].

But also in the field of radiation therapy laser-driven ion accelerators are discussed as an alternative ion source [Masood et al., 2014; Schüller et al., 2020], as they can also efficiently accelerate carbon ions

[Hegelich et al., 2002] and have the potential to further improve the methodology by utilizing the lately discovered ultra-high dose rate (FLASH) radiotherapy [Hughes and Parsons, 2020; Schüller et al., 2020]. For many of the mentioned applications the initial TNSA-generated ion beam is not suitable because of its broad energy spread, its large divergence, and the harsh background radiation environment in the form of an ElectroMagnetic Pulse (EMP), x-rays and electrons. For this reason, laser-driven ion beamlines with conventional accelerator elements like dipole magnets, quadrupole magnets, solenoid magnets and plasma lenses are used in various laboratories around the world to shape the TNSA-generated ion beam to the respective requirements [Zhu et al., 2020; Rösch et al., 2020; Brack et al., 2020; Cirrone et al., 2020; Apiñaniz et al., 2021; Kroll et al., 2022]. In this context, an association of several German Helmholtz institutes and universities founded the Laser Ion, Generation, Handling and Transport (LIGHT) collaboration.

1.2. The LIGHT collaboration

The main goal of the LIGHT collaboration is to study the combination of laser-driven ion beams with conventional accelerator components and to utilize this knowledge in order to demonstrate the potential of laser-driven ion beamlines in applications. Therefore, in the early stages of this collaboration, the LIGHT beamline was realized at the experimental area Z6 of GSI [Busold et al., 2014b]. This beamline is the foundation for the investigations of this work. Its setup is shown in Fig. 1.1.

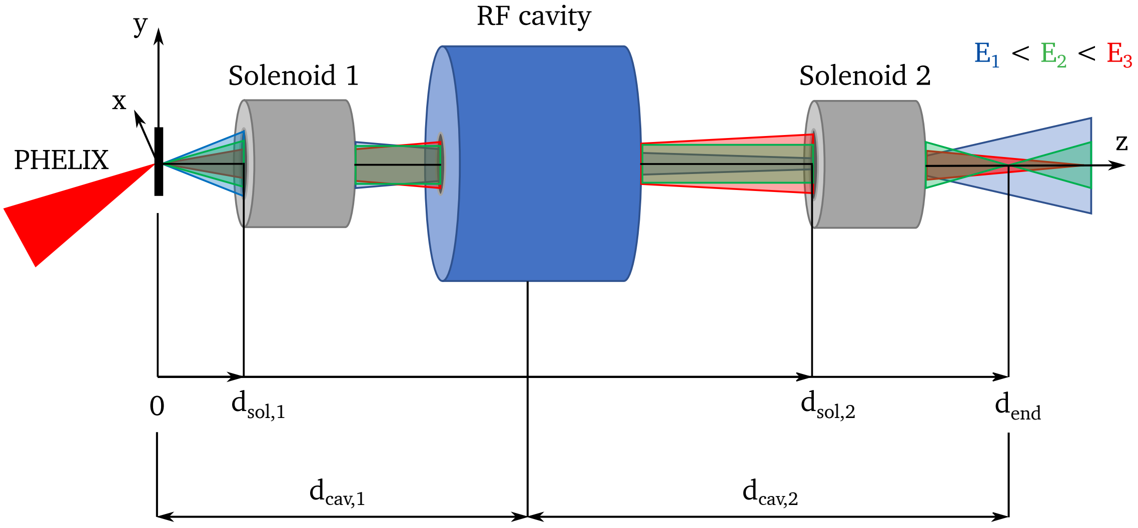

Fig. 1.1: Schematic setup of the LIGHT beamline at the experimental area Z6 of GSI.

As can be seen, at the origin of this beamline the Petawatt High-Energy Laser system for heavy-Ion eXperiments (PHELIX) [Bagnoud et al., 2010] is used for the ion acceleration and the energy selection as well as the ion beam transport is performed by two pulsed, high-field solenoid magnets which were manufactured by the high-field laboratory of the Helmholtz-Zentrum Dresden-Rossendorf (HZDR). Due to the availability of the accelerator infrastructure at GSI it is also possible to operate a RadioFrequency (RF) cavity, which gives the LIGHT beamline the unique possibility to manipulate the energy distribution of the transported, laser-accelerated ion bunches. The achieved beam parameters with the combination of the

TNSA source, the solenoid magnets and the RF cavity at the LIGHT beamline has already led to several publications [Busold et al., 2013, 2014b,a, 2015; Jahn et al., 2019; Metternich et al., 2022].
Meanwhile, applications with the LIGHT beamline are taking center stage. The two main applications that are currently being pursued by the LIGHT collaboration are the measurement of the ion-stopping power in transient plasma targets and the injection of a laser-accelerated ion beam into GSI's heavy ion synchrotron SIS18 (SIS18). Therefore, the main goal of this thesis is to use the LIGHT beamline to generate a suitable ion beam for these applications. For the realization of this goal, the interaction of the magnetic and electric fields of the beamline components with the laser-accelerated ion beam is extensively investigated in this thesis by a comparison of theoretical predictions, numerical simulations and experimental data.

1.3. Thesis outline

This thesis is divided into two parts. In Part I, the different technologies that are used at the LIGHT beamline and their individual implementation are explained and characterized step by step, starting with the ion beam generation with the PHELIX laser via the TNSA mechanism in Chapter 2. After that, an introduction to the field of beam dynamics is given in Chapter 3 as a basis for the subsequent theoretical considerations on the transport and the longitudinal shaping of the TNSA-generated ion beams in the Chapters 4 and 5. Then, in Part II, the investigations and results of three different applications that have been worked on in the course of this thesis are presented, namely

- The injection of a laser-accelerated ion beam in the SIS18 (Chapter 6)
- The generation of high proton fluxes (Chapter 7)
- The generation of a suitable ion beam for stopping power experiments (Chapter 8)

Finally, Chapter 9 concludes this thesis with a summary and an outlook.

Part I.

Shaping of laser-accelerated ion beams

2. Properties of laser-accelerated ion beams

Within the scope of this work, only the Target Normal Sheath Acceleration (TNSA) has been used to generate the ions at the LIGHT beamline, since it is by far the most reliable and most studied laser-based acceleration mechanism. In the following, the theoretical basics of the TNSA mechanism are explained first and then the TNSA source at the LIGHT beamline is characterized. Finally, also the reconstruction of a TNSA-generated ion beam for the numerical simulations of this work is described.

2.1. Target Normal Sheath Acceleration

The following theoretical introduction is based on the information given in [Schollmeier, 2009]. More details on the TNSA mechanism can also be found in [Gibbon, 2005; Mulser and Bauer, 2010; Macchi, 2013].
To accelerate ions with the TNSA mechanism, a laser pulse with an intensity of about 10^{18} W cm^{-2} or higher is focused on a target, which is typically a thin foil with a thickness in the range of nano- to micrometers (see Fig. 2.1).

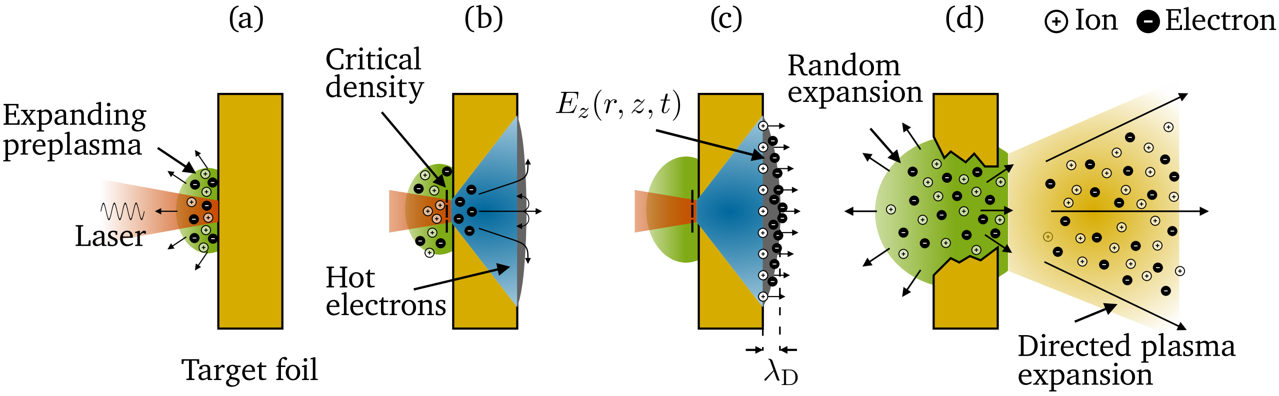

Fig. 2.1: Schematic, step-by-step overview of the TNSA mechanism.

Such high-intensity pulses usually have a slow rising edge and are accompanied by prepulses and Amplified Spontaneous Emission (ASE), which are causing a formation of a preplasma on the front side of the target. Then, various electron heating mechanisms like

- resonance absorption [Gibbon, 2005; Mulser and Bauer, 2010],
- Brunel heating [Mulser and Bauer, 2010; Kruer, 2019] and
- $\mathbf{j} \times \mathbf{B}$ heating [Gibbon, 2005; Mulser and Bauer, 2010]

during the laser-plasma interaction at the critical density lead to the generation of hot electrons, which are mainly directed towards the target. In this process, only the first electrons or those that gain enough energy manage to escape the target on the rear side. The other electrons are electrostatically confined and circulate back and forth through the target, forming electron sheaths on both sides. Since initially there is not a screening plasma at the rear side of the target, the charge separation induces an electric field strong enough ($\sim$ TV m^{-1}) to ionize the target atoms on the surface by field ionization and accelerate them to energies in the MeV range. Unless explicitly removed, there is a contaminant layer on the target surface and the ionized hydrogen of this layer is accelerated most rapidly and efficiently due to its highest charge-to-mass ratio. Due to the short timescale ($\sim$ ps) and the target atoms on the rear side being initially cold, the quality of the resulting beam is very high [Nürnberg et al., 2009; Cowan et al., 2004]. The exact beam parameters depend strongly on the temporal profile and the intensity of the laser pulse, as well as on the target properties. However, since these relations were not investigated within the scope of this work, they will not be discussed further. Instead, the TNSA source of the LIGHT beamline at the experimental area Z6 of GSI is explained and characterized in the following.

2.2. Characteristics of the TNSA source at the LIGHT beamline

To generate laser pulses with intensities above 10^{18} W cm^{-2}, the Chirped Pulse Amplification (CPA) technique [Strickland and Mourou, 1985] is used by the PHELIX laser. The generation and the temporal stretching of the laser pulse with a wavelength of 1053 nm as well as its amplification by Nd:glass amplifiers takes place in the PHELIX building. Then the laser pulse is transported to the experimental area Z6, where it is compressed in time to $\sim$ 650 fs. The maximum aperture of the PHELIX laser is 28 cm, but since the compressor gratings at Z6 can only handle a maximum beam diameter of 12 cm, the full aperture cannot be used at Z6 in case of the short pulse operation mode. Therefore, the pulse energy is limited to 40 J to remain below the destruction thresholds of the optics. After the Z6 compressor, the beam is transported to the Z6 target chamber via the 100 TW beamline. For LIGHT experiments, a coated off-axis glass parabola with a focal length of 300 mm in the Z6 target chamber focuses the beam on the TNSA target. The focal spot on the target has usually a size of 3.5 µm which, in case of a laser pulse with an energy of 40 J and a temporal length of 650 fs, results in an intensity greater than 10^{19} W cm^{-2} on the TNSA target.

In the experimental campaigns of this work, the TNSA target is typically a (5 - 10) µm thick gold or tungsten foil, and the initial proton beam is characterized with the Radiochromic Imaging Spectroscopy (RIS). In RIS, transparent plastic films are used that contain a polymer that turns deep blue by solid-state polymerization in proportion to the irradiation dose received [McLaughlin et al., 1996]. These RadioChromic Films (RCFs) usually consist of a radiation-sensitive layer (active layer) and a protective layer (passive layer), which have a thickness of several µm. The energy deposition in the active layers of an RCF stack is therefore different for the ionizing radiation types generated by the TNSA mechanism. The gamma rays and the electrons penetrate the whole stack and deposit a small amount of their kinetic energy in all active layers, whereas the accelerated ions are getting stopped in the RCF stack and, according to the Bragg curve, deposit a large fraction of their energy in a small region. Since the energy loss per distance of a charged particle in matter is proportional to Z_{eff}^2 of the projectile, all other ion species in the MeV range except protons are getting stopped within the first few µm of the RCF stack. Therefore, the deposited energy of a TNSA source with ions in the MeV range in an RCF stack with many active layers is mainly caused by protons. There is only one exception, and this is when there is no or only a thin passive layer in front of the first active layer. In this case, the deposited energy in the first active layer of the RCF stack is mainly caused by ion species heavier than protons. Since the range of ions in matter can be determined very precisely [Ziegler and Biersack, 1985], the RIS allows a complete spatial and spectral reconstruction of a TNSA-generated proton beam in the MeV range from a single shot [Nürnberg, 2010; Schmitz et al., 2022]. In addition, the inherent insensitivity of RCFs to ElectroMagnetic Pulses (EMP), which are generated during laser-matter interaction, makes the RIS the most commonly used diagnostic for the characterization of laser-accelerated proton

sources in many laboratories. Within the scope of this work, more detailed descriptions of the evaluation of RIS data will be given on the basis of specific measurements, e.g. in the following for the characterization of the TNSA source from an experimental campaign with the LIGHT beamline in January 2021. More information on the distinction between types of ionizing radiation, determination of deposited energy from RCF scans, and calibration of different RCF batches with respect to RIS can be found in [Schmitz et al., 2022].
The configuration of the RCF stack for the TNSA source characterization in the experimental campaign with the LIGHT beamline in January 2021 is shown in Fig. 2.2.

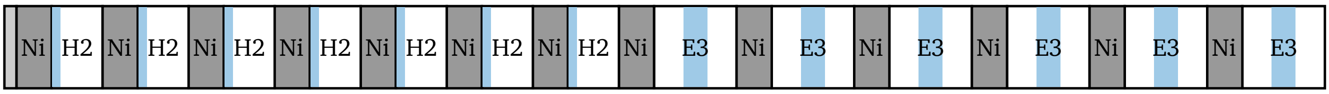

Fig. 2.2: RCF stack configuration for the TNSA source characterization during an experimental campaign with the LIGHT beamline in January 2021.

The first layer is a 12.5 µm thick aluminum (Al) foil, the nickel (Ni) layers have a thickness of 50 µm and the RCFs are of type HD-v2 (H2) and EBT3 (E3) manufactured by the company *Gafchromic*. The active layers (colored blue) of the EBT3 have a thickness of 27 µm whereas the active layers of the HD-v2 only have a thickness of 8 µm. In addition, the active layers of the EBT3 is located between two passive layers (colored white), each with a thickness of 120 µm, and for the HD-v2, there is only one passive layer with a thickness of 97 µm. In the experiment, the RCF stack was placed in front of the first solenoid 40 mm from the TNSA Target. The corresponding normalized deposited energies per pixel of each active layer is shown in Fig 2.3. Since the total deposited energy in the active layers of the same RCF type decreases for higher penetration depths, the normalization ensures that the distribution of the deposited energy can be seen in each active layer. The indicated energies correspond to the kinetic energies of the protons stopped in the respective active layer.

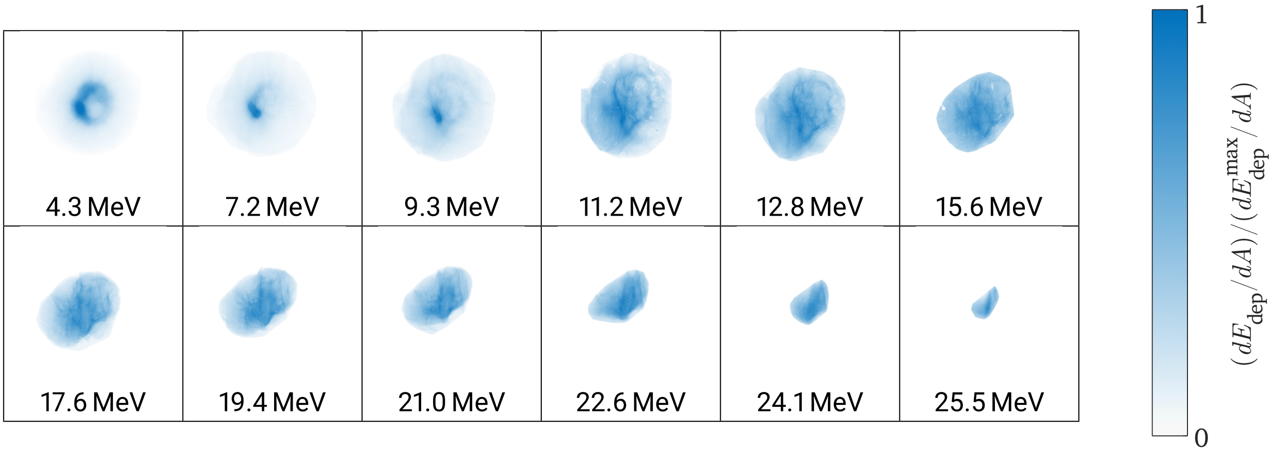

Fig. 2.3: Normalized deposited energies per pixel $(dE_{\mathrm{dep}}/dA)/(dE_{\mathrm{dep}}^{\mathrm{max}}/dA)$ in the active layers of an RCF stack from an experimental campaign which was carried out during this thesis in January 2021. The indicated energies correspond to the kinetic energies of the protons stopped in the respective active layer.

Based on the decreasing size of the beam for higher energies, one can conclude that the initial divergence of protons with higher energies decreases. In addition, the deposited energy in the active layers is higher in the center of the beam than at the edge of the beam. This is mainly due to the fact that protons with higher energies deposit a small fraction of their kinetic energy in all active layers that they penetrate.

The total deposited energy in the active layers is shown by the black dots of the left image in Fig. 2.4. The abrupt increase of the deposited energy at 17.6 MeV is due to the fact that from this energy on the RCFs of type EBT3 were used, which absorb more energy due to their thicker active layer. From RIS data, the energy spectrum and the maximum divergence angle of each energy of the TNSA generated proton beam can be determined by fits. In this procedure, the energy spectrum is not fitted to the measured deposited energies, but is optimized so that its theoretically deposited energy, calculated by the Stopping and Range of Ions in Matter (SRIM) code [Ziegler and Biersack, 1985], matches the measured deposited energy. For a typical TNSA generated proton beam an exponentially decaying energy spectrum

$$\frac{dN}{dE} = \frac{N_0}{E} \cdot \exp(-\frac{E}{k_\mathrm{B}T}) \tag{2.1}$$

and a uniform distribution of the initial deviation angle θ in the range $[0, \theta_\mathrm{max}]$ with a quadratic dependence of the maximum initial deviation angle θ_max on the energy

$$\theta_\mathrm{max} = a_2 \cdot E^2 + a_1 \cdot E + a_0 \tag{2.2}$$

provides a good match to the experimental data [Schmitz et al., 2022]. In Fig. 2.4 the presented experimental data are compared to the corresponding results. The obtained fit parameters $(k_\mathrm{B}T, N_0, a_2, a_1, a_0)$ are given in Table 2.1. Thus, the results show good agreement with the measured data.

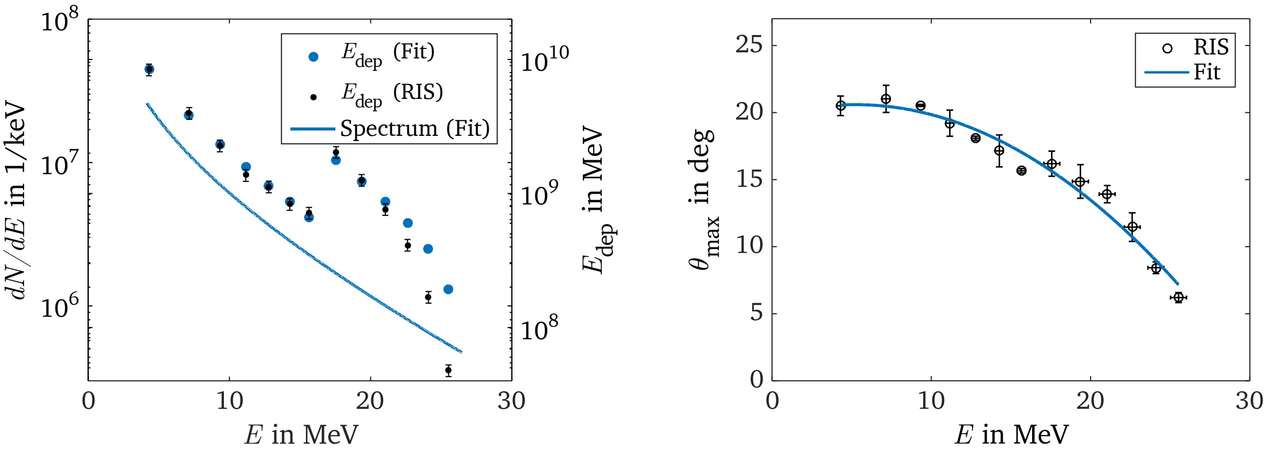

Fig. 2.4: The left image shows the deposited energies in the active layers of a RIS measurement from an experimental campaign conducted as part of this work in January 2021, as well as an exponentially decaying spectrum whose theoretically deposited energy was fitted to the measured data. In the right image, a quadratic fit (see Equation 2.1) to the measured maximum divergence angle $\theta_\mathrm{max}(E)$ is shown. The values obtained by the fits are listed in Table 2.1.

Table 2.1: Corresponding values of the parameters in Equation 2.1 and 2.2 which are determined by fits to the RIS data shown in Fig. 2.3.

N_0	$k_\mathrm{B}T$	a_2	a_1	a_0
1.61×10^{11}	10.35 MeV	-0.03 °/MeV^2	0.34 °/MeV	19.71 °

The deviations at higher energies than 20 MeV in case of the energy spectrum indicates, that the measured spectrum decays more rapidly from this point on. This can be remedied by using a more complex distribution function for the spectrum. However, this will not be further investigated, since the spectrum in this energy range has no relevance for this work and its influence on the spectrum up to an energy of 20 MeV is negligible.

In the simulation studies of this work the introduced parameters $k_\mathrm{B}T$, N_0, a_2, a_1, and a_0 are used to generate the ion beam at the origin of the LIGHT beamline. This process will now be explained in the following.

2.3. Reconstruction of TNSA-generated ion beams

As the first step, an energy is assigned to each particle. As shown in the previous section, the energy spectrum of a TNSA-generated proton beam at the LIGHT beamline can be described by

$$\frac{dN}{dE} = \frac{N_0}{E} \cdot \exp\left(-\frac{E}{k_\mathrm{B}T}\right). \tag{2.3}$$

Such an energy spectrum can be generated by the inverse transformation method [Devroye, 1986], so by inverting the corresponding Cumulative Distribution Function (CDF), which in this case is

$$\begin{aligned}
\mathrm{CDF}(E) &= \frac{N}{\tilde{N}} \int_{-\infty}^{E} \frac{1}{t} \exp\left(-\frac{t}{k_\mathrm{B}T}\right) dt \qquad (2.4)\\
&= \frac{N}{\tilde{N}} \int_{E_\mathrm{min}}^{E} \frac{1}{t} \exp\left(-\frac{t}{k_\mathrm{B}T}\right) dt \qquad (2.5)\\
&= \frac{N}{\tilde{N}} \left[\mathrm{Ei}\left(-\frac{E}{k_\mathrm{B}T}\right) - \mathrm{Ei}\left(-\frac{E_\mathrm{min}}{k_\mathrm{B}T}\right)\right]. \qquad (2.6)
\end{aligned}$$

Thereby N is the number of particles to be generated, Ei the exponential integral, and

$$\tilde{N} = \int_{E_\mathrm{min}}^{E_\mathrm{max}} \frac{N}{E} \cdot \exp\left(-\frac{E}{k_\mathrm{B}T}\right) dE \tag{2.7}$$

the normalizing constant. Let $\mathcal{U}_{[a,b]}$ be uniformly distributed numbers in the interval $[a, b]$, then the energy spectrum can be generated as follows [Devroye, 1986]:

$$E = \mathrm{CDF}^{-1}(\mathcal{U}_{[0,1]}). \tag{2.8}$$

The number of particles can be chosen freely, as well as the maximum energy E_max and the minimum energy E_min. The maximum E_max is usually set as the cut-off Energy E_cut, but it can also be chosen smaller if high energies are not of interest. After assigning an energy to each particle their corresponding maximal initial divergence θ_max is set with Equation 2.2.
To account for the initial beam quality, a random micro divergence $\Delta\theta_{(x,y,z)}$ as well as a random start delay t_0 can be added to each particle. Let $\mathcal{N}_{(x,y,z)}(\mu, \sigma^2)$ be normally distributed random numbers with a mean value μ and a standard deviation σ, then the micro divergence is defined as

$$\Delta\theta_{(x,y,z)} = \Delta\theta_\mathrm{max} \cdot \mathcal{N}_{(x,y,z)}(\mu = 0, \sigma^2 = 0.2) \tag{2.9}$$

and the start delay as

$$t_0 = \mathcal{U}^{t}_{[0,\Delta t_\mathrm{max}]}. \tag{2.10}$$

Now only the source size r has to be characterized. In [Nürnberg, 2010], a real source size between $r_{\text{min}} = 50\,\mu\text{m}$ and $r_{\text{max}} = 380\,\mu\text{m}$, with a linear dependency on the energy was determined. These values have been adopted for the simulation studies of this work. Then the initial values $(x_0, y_0, z_0, \dot{x}_0, \dot{y}_0, \dot{z}_0, t_0)$ are assigned to each particle. Therefore, additional uniformly distributed random numbers are generated:

$$\theta = \sqrt{\mathcal{U}^{\theta}_{[0,\theta_{\text{max}}(E)]}}, \qquad \phi = \mathcal{U}^{\phi}_{[0,2\pi]}. \tag{2.11}$$

So, θ_i is the initial divergence of a particle, which is energy dependent $(\theta_i \in \theta_{\text{max}}(E))$, and $\phi_i \in [0, 2\pi]$ its azimuth direction. With these, the transverse, initial location deviation is obtained by

$$|\mathbf{r}_0| = (r_{\text{max}} - (r_{\text{max}} - r_{\text{min}}) \cdot E/E_{\text{cut}}) \cdot \theta/\theta_{\text{max}} \tag{2.12}$$

and the initial location of the particle is

$$\mathbf{r}_0 = \begin{pmatrix} x_0 \\ y_0 \\ z_0 \end{pmatrix} = |\mathbf{r}_0| \cdot \begin{pmatrix} \cos(\phi) \\ \sin(\phi) \\ 0 \end{pmatrix}. \tag{2.13}$$

The total initial velocity is given by the Lorentz factor

$$|\dot{\mathbf{r}}_0| = c \cdot \sqrt{1 - 1/\gamma^2}, \quad \gamma = \frac{\tilde{E}}{m_0 c^2} \tag{2.14}$$

and the initial direction deviations are then calculated as follows:

$$\dot{\mathbf{r}}_0 = \begin{pmatrix} \dot{x}_0 \\ \dot{y}_0 \\ \dot{z}_0 \end{pmatrix} = |\dot{\mathbf{r}}_0| \begin{pmatrix} \sin(\theta + \Delta\theta_x) \cdot \cos(\phi) \\ \sin(\theta + \Delta\theta_y) \cdot \sin(\phi) \\ \cos(\theta + \Delta\theta_z) \end{pmatrix}. \tag{2.15}$$

Since many simulations of this work were performed before the evaluation of the RIS measurement shown in Section 2.2, the parameters E_{cut}, $k_{\text{B}}T$, a_2, a_1, and a_0 given in [Busold, 2014] are mostly used for the initial proton beam reconstruction in this work. Also, the micro divergence $\Delta\theta_{\text{max}}$ and the start delay Δt_{max} were set to zero, so the initial beam quality is assumed to be perfect. However, in the Appendix A.1 it is exemplarily shown that within the expected deviations of these parameters no influence on the results of the simulations in this work is to be expected.

The considerations in relation to the ion beam generation at the LIGHT beamline have thus been completed. In the next chapter, the theoretical fundamentals of beam dynamics are presented as a basis for the following investigations on the transport and the longitudinal shaping of the TNSA-generated ion beam at the LIGHT beamline.

3. Beam dynamic fundamentals

The interaction of ion beams with magnetic and electric fields is fundamental in accelerator physics. Therefore, the terminology of accelerator physics is used throughout this thesis and will be introduced in this chapter. For this purpose, the motion of a single particle is considered first. Then, the main properties of ion beams with multiple particles are explained, as well as the particle tracking with numerical simulations. Finally, in the last section of this chapter, the influence of space charge effects on the beam dynamics will be discussed.

This chapter is based on the textbooks [Reiser et al., 2008], [Hinterberger, 2008] and [Wille, 1996], where also more details on these topics can be found.

3.1. Coordinate system

In mathematical modeling, it is usually very practical to adapt the coordinate system to the given symmetries of the system under consideration. Accelerator physicists therefore use a coordinate system $K(x, y, s)$ whose origin is co-moving with the so-called reference particle. The trajectory of the reference particle, which is called nominal trajectory or orbit, is given by the beam guiding magnets (solenoids, dipoles, quadrupoles, sextupoles, etc.) of the beamline. The parameter s describes the distance traveled along the nominal trajectory and thereby determines the instantaneous position of the coordinate system. Therefore, the description of a single particle trajectory $r(s)$ only requires the relations $x(s)$ and $y(s)$

$$\mathbf{r}(s) = \mathbf{r}_0(s) + x(s)\mathbf{u}_x(s) + y(s)\mathbf{u}_y(s) \tag{3.1}$$

with the unity vectors $\mathbf{u}_x$ and $\mathbf{u}_y$. In this context, the coordinates x and y are called radial and axial location deviation, or horizontal and vertical location deviation if the magnetic mid-level and the horizontal plane coincide [Hinterberger, 2008].

For a complete characterization of a particle in the six-dimensional phase space and the determination of its trajectory, four additional parameters must be specified. In accelerator physics these are usually the vertical and horizontal direction deviations (x', y'), the longitudinal location deviation l, and the momentum deviation δ, which are defined as follows:

$$x' = \frac{dx}{ds}, \quad y' = \frac{dy}{ds}, \quad l = -v_0(t - t_0), \quad \delta = \frac{p - p_0}{p_0}. \tag{3.2}$$

Thereby v_0 is the velocity, t_0 the time of flight and p_0 the momentum of the reference particle. The coordinate system $K_{\text{curv}}(x, y, s)$ is curvilinear. For some considerations it is reasonable to define a normal (right-handed, Cartesian), co-moving coordinate system $K_{\text{cart}}(x, y, z)$ locally. The two coordinate systems are shown in Fig. 3.1.

The main difference between these two systems is the line element [Hinterberger, 2008]:

$$\begin{aligned} d\mathbf{r}_{xys} &= \mathbf{u}_x dx + \mathbf{u}_y dy + \mathbf{u}_s(1 + hx)ds, \\ d\mathbf{r}_{xyz} &= \mathbf{u}_x dx + \mathbf{u}_y dy + \mathbf{u}_z dz. \end{aligned} \tag{3.3}$$

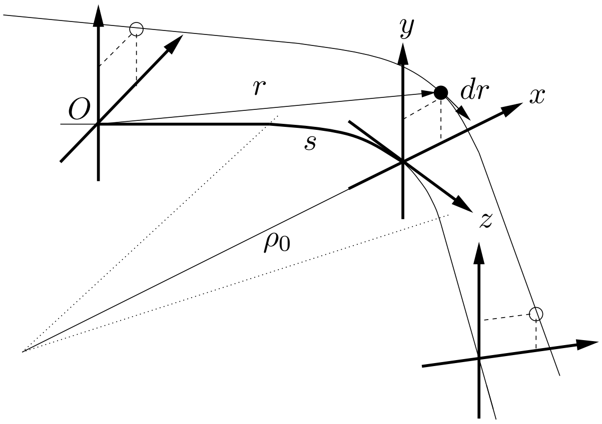

Fig. 3.1: Relation between a curvilinear coordinate system $K_{\text{curv}}(x, y, s)$ and a Cartesian coordinate system $K_{\text{cart}}(x, y, z)$ [Hinterberger, 2008].

The parameter $h = 1/\rho_0$ is the curvature of the nominal trajectory (see Fig 3.1) and therefore a function of s. It applies, that $\mathbf{u}_s = \mathbf{u}_z$ and $z' = 1 + hx$, so the systems are identical if $h = 0$. Since this is always the case in this thesis, further on the following relations are always valid:

$$\begin{aligned} \frac{dx}{dz} &= \frac{p_x}{p_z} = \frac{x'}{z'} = x', \\ \frac{dy}{dz} &= \frac{p_y}{p_z} = \frac{y'}{z'} = y'. \end{aligned} \tag{3.4}$$

Furthermore, x' and y' have typically small values which allows their specification by an angle deviation in paraxial approximation

$$\begin{aligned} \theta \approx \tan\theta &= \frac{dx}{dz} = x', \\ \varphi \approx \tan\varphi &= \frac{dy}{dz} = y'. \end{aligned} \tag{3.5}$$

This results in a very useful mnemonic for the unit mrad, which is

$$\mathrm{mrad} = \mathrm{mm/m}. \tag{3.6}$$

Even though the divergence of the laser-accelerated ion beam in this thesis has a half opening angle of up to 500 mrad, due to the limited aperture of the beamline components, ions with large direction deviations are not transported, and therefore this assumption is largely fulfilled. In contrast, dealing with the relative momentum deviation δ is inconvenient, since it is typically given in promille (‰), which is not suitable in relation to laser-accelerated ion beams. Therefore, instead of the momentum deviation δ and the longitudinal location deviation l, the kinetic energies E_{kin} and the Time of Flight (ToF) t of the particles is specified most of the time. To conclude, here are the parameters with their respective units, that are used in this thesis to characterize particles:

$$\begin{pmatrix} x \\ x' \\ y \\ y' \\ t \\ E \end{pmatrix} = \begin{pmatrix} \text{horizontal location deviation} \\ \text{horizontal direction deviation} \\ \text{vertical location deviation} \\ \text{vertical direction deviation} \\ \text{time of flight} \\ \text{kinetic energy} \end{pmatrix}, \text{ in } \begin{pmatrix} \mathrm{mm} \\ \mathrm{mrad} \\ \mathrm{mm} \\ \mathrm{mrad} \\ \mathrm{ns} \\ \mathrm{MeV} \end{pmatrix}. \tag{3.7}$$

3.2. Multipole expansion

Now the influence of a magnetic field on a charged particle will be considered. If a magnetic field $\mathbf{B} = (0, B_y, 0)$ acts on a charged particle with the velocity $\mathbf{v} = (0, 0, v_s)$ the Lorentz force is balancing the centrifugal force which leads to

$$\frac{1}{\rho_0(x,y,s)} = \frac{q}{p} B_y(x,y,s) \tag{3.8}$$

with the momentum $p = mv_s$ and the charge q of the particle. The fact that the curvature radius $\rho_0(x,y,s)$ is usually small compared to transverse coordinates (x,y) allows the multipole expansion of the magnetic field B_y in the vicinity of the nominal trajectory [Wille, 1996]:

$$\frac{q}{p} B_y(x) = \frac{q}{p} B_{y0} + \frac{q}{p}\frac{dB_y}{dx} x + \frac{1}{2!}\frac{q}{p}\frac{d^2 B_y}{dx^2} x^2 + \frac{1}{3!}\frac{q}{p}\frac{d^3 B_y}{dx^3} x^3 + ... \tag{3.9}$$

Designation, definition and principal effect of the individual multipoles on the motion of the beam are shown in Table 3.1. It is technically feasible to generate magnetic fields with particular multipole strengths in the region of the beam. These magnets are named accordingly (dipole magnets, quadrupole magnets, etc.).

Table 3.1: Designation, definition and principal effects of the individual multipoles in an accelerator, according to [Wille, 1996].

Multipole	Definition	Effect
Dipole	$\frac{1}{\rho_0} = \frac{q}{p} B_{y0}$	Beam steering
Quadrupole	$\kappa = \frac{q}{p}\frac{dB_y}{dx}$	Beam focusing
Sextupole	$m = \frac{q}{p}\frac{d^2 B_y}{dx^2}$	Chromaticity compensation
Octupole	$o = \frac{q}{p}\frac{d^3 B_y}{dx^3}$	Field errors or field compensation

In linear beam optics, only dipole and quadrupole fields are considered and higher order terms are neglected. With this simplification and additional assumptions, some fundamental concepts and quantities of accelerator physics, such as the betatron oscillation and the beam emittance, can easily be derived, which will be done in the following.

3.3. Linear equation of motion

The linear equations of motion form the basis for the calculations in linear beam optics. Therefore, their derivation is briefly described in the following. The given information are based on [Wille, 1996], in which the deviation is shown in more detail.

In case of a magnetic field $\mathbf{B} = (B_x, B_y, 0)$ the Lorentz equation leads to

$$\ddot{\mathbf{r}} = \frac{q}{m}(\dot{r} \times \vec{B}) = \frac{q}{m} \begin{pmatrix} -(1+\frac{x}{\rho_0})\dot{s}B_y \\ (1+\frac{x}{\rho_0})\dot{s}B_x \\ x'\dot{s}B_y - z'\dot{s}B_x \end{pmatrix}. \tag{3.10}$$

A more general equation of $\ddot{\mathbf{r}}$ is obtained by calculating the second derivative of Equation 3.1:

$$\ddot{\mathbf{r}} = \begin{pmatrix} x''\dot{s}^2 + x'\ddot{s} - (1+\frac{x}{\rho_0})\frac{\dot{s}^2}{\rho_0} \\ y''\dot{s}^2 + y'\ddot{s} \\ \frac{2}{\rho_0}x'\dot{s}^2 + (1+\frac{x}{\rho_0})\ddot{s} \end{pmatrix}. \tag{3.11}$$

So it is assumed that the nominal trajectory only has a curvature in the x-z plane. Since the particles are generally moving with relativistic velocities, the change in the longitudinal velocity is negligible. Therefore, only the transverse components are considered and $\ddot{s} \approx 0$. Combining the Equations 3.10 and 3.11 leads to

$$\begin{aligned} x'' - (1+\frac{x}{\rho_0})\frac{1}{\rho_0} &= -\frac{v}{\dot{s}}\frac{q}{p}B_y(1+\frac{x}{\rho_0}), \\ y'' &= \frac{v}{\dot{s}}\frac{q}{p}B_x(1+\frac{x}{\rho_0}). \end{aligned} \tag{3.12}$$

Further, assuming that $\delta \ll 1$, $x \ll \rho_0$ and $y \ll \rho_0$, as well as only considering the terms of the multipole expansion for the dipole and the quadrupole strength ($\frac{q}{p}B_y = \frac{1}{\rho_0} - \kappa x$, $\frac{q}{p}B_x = -\kappa y$), one obtains the linear equation of motion

$$\begin{aligned} x''(s) + \left(\frac{1}{\rho_0^2(s)} - \kappa(s)\right)x(s) &= \frac{1}{\rho_0(s)}\frac{\Delta p}{p}, \\ y''(s) + \kappa(s)y(s) &= 0. \end{aligned} \tag{3.13}$$

With these, a matrix formalism can be derived, which is a very practical tool for calculating the trajectories for a system with many components. The equation of motion and the matrix formalism can be also extended up to the higher orders [Hinterberger, 2008]. But this, as well as the matrix formalism itself, will not be discussed as it was not used in the context of this thesis. Information on these topics can be found in [Wille, 1996] and [Hinterberger, 2008]. Instead, the equation of motion are used in the next section to introduce some essential concepts for ion beams with multiple particles.

3.4. Phase space ellipse and Liouville's theorem

The equations of motion (Equation 3.13) in case of a straight orbit ($1/\rho_0 = 0$) and a particle that has the nominal momentum ($\Delta p/p = 0$) leads to Hill's equation

$$x''(s) - \kappa(s)x(s) = 0. \tag{3.14}$$

A valid solution of this differential equation is an oscillation around the orbit [Wille, 1996]:

$$x(s) = \sqrt{\varepsilon\,\hat{\beta}(s)}\cos(\Psi(s) + \phi_c), \tag{3.15}$$

which is called betatron oscillation. Thereby $\hat{\beta}(s)$ is the beta function, ε the emittance, $\sqrt{\varepsilon\hat{\beta}(s)}$ the envelope of the particle beam, ϕ_c the constant of integration and

$$\Psi(s) = \int_0^s \frac{d\tilde{s}}{\hat{\beta}(\tilde{s})} \tag{3.16}$$

the phase advance. Inserting Equation 3.15 in its derivative $x'(s)$ and defining

$$\hat{\alpha}(s) := -\frac{\hat{\beta}(s)'}{2} \tag{3.17}$$

as well as

$$\hat{\gamma}(s) := \frac{1+\hat{\alpha}(s)^2}{\hat{\beta}(s)} \tag{3.18}$$

results in an ellipse equation in phase space [Wille, 1996]:

$$\frac{A}{\pi} = \hat{\gamma}(s)x^2(s) + 2\hat{\alpha}(s)x(s)x'(s) + \hat{\beta}(s)x'^2(s) = \varepsilon. \tag{3.19}$$

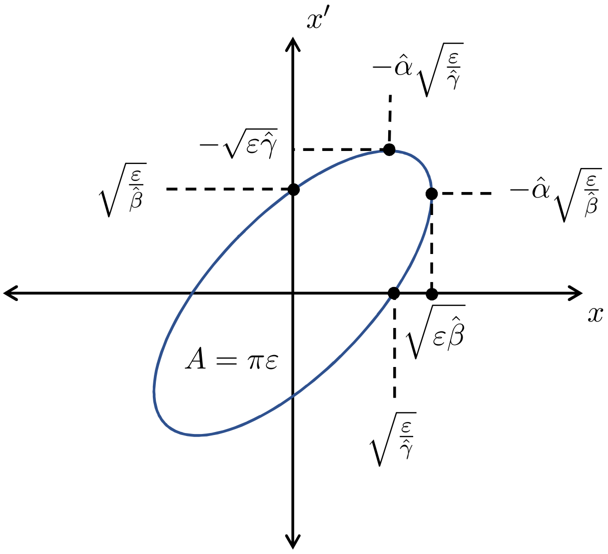

Fig. 3.2: Illustration of the x-x' phase space ellipse given by the Courant-Snyder parameters.

The form and the orientation of the ellipse in x-x' phase space is given by $\hat{\alpha}(s)$ and $\hat{\beta}(s)$ or $\hat{\gamma}(s)$, which are called Twiss or Courant-Snyder parameters (see Fig. 3.2). They can, like $x(s)$, be evolved stepwise through a system with many components. Thereby the area of the ellipse, which is proportional to the emittance, remains constant. This follows from Liouville's theorem, which states that every volume element in phase space is constant in time, as long as the particles obey only the canonical equations of motion. In the context of linear beam optics this condition is always fulfilled, which means that for a given emittance, the beam envelope at any position can be calculated via the evolution of the Twiss parameter along s. However, the following effects can cause a deformation of the ellipsoid shape of the beam as well as a redistribution of the particles [Reiser et al., 2008]:

- Chromatic aberrations
- Spherical aberrations

- Magnetic field errors
- Misalignment of beamline components
- Collisions between the particles of the beam and gases or foils in the beamline
- Random kicks due to RadioFrequency (RF) noise and mechanical vibrations
- Nonlinear space charge effects

This raises the question, how the emittance of randomly distributed particles with a non-ellipsoid shape is determined. Therefore, a statistical definition of the emittance is now introduced, which is most commonly used in accelerator physics.

3.5. Statistical definition of emittance

First, the advantages of a statistical definition of emittance will be explained using the example of the change in directional deviation of a monoenergetic beam by a solenoid magnet with spherical aberration. The initial beam is divergent and represents a perfect ellipse in the x-x' phase space, like the blue beams in Fig. 3.3.

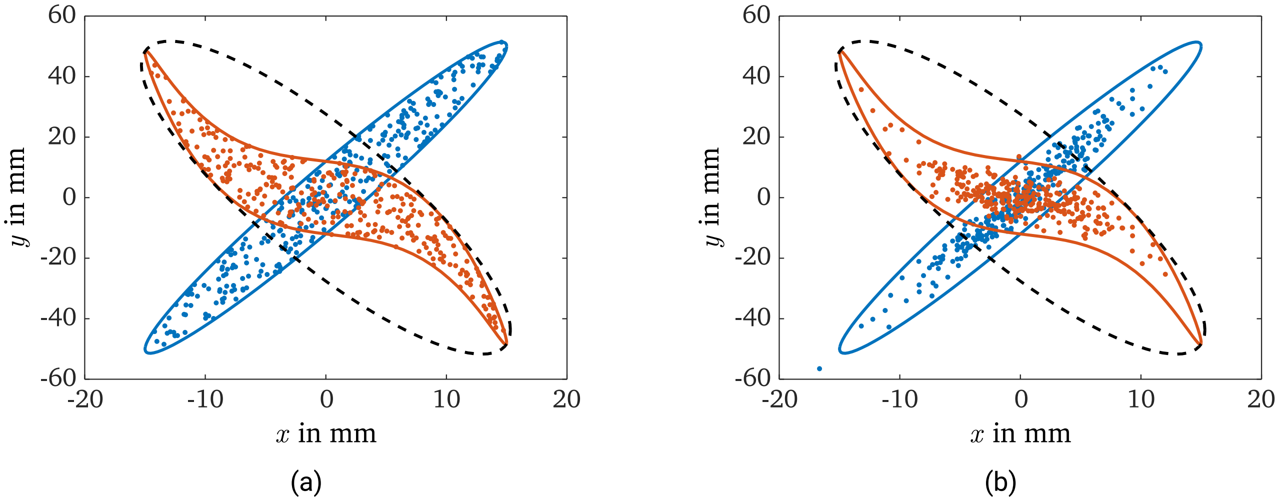

Fig. 3.3: Illustration of a divergent, uniformly distributed beam (blue beam Fig. 3.3a) and a divergent, Gaussian distributed beam (blue beam Fig. 3.3b) in the x-x' phase space. These beams are rotated in phase space by a solenoid magnet (red beams). Thereby the phase space area, that is enclosed by the beam, remains constant, according to Liouville's theorem. But due to the spherical aberration of the solenoid, the elliptical shape of the beams is lost. The area of an ellipse that can enclose the red beams therefore increases, which is indicated by the black dashed ellipses.

The direction deviation caused by the solenoid is [Reiser et al., 2008]:

$$\Delta x' = -\frac{x}{f} - C_\mathrm{s} \cdot x^3, \tag{3.20}$$

with the focal length f and the spherical aberration coefficient C_s of the solenoid magnet, which will both be considered in more detail in Section 4.2. So the solenoid rotates the ellipse in the x-x' phase space and

according to Liouville's theorem, the phase space area, that is enclosed by the beam, remains constant. But due to the spherical aberration of the solenoid, the beam quality deteriorates since the elliptical shape of the beams is lost (red beams in Fig. 3.3). To reflect the degradation of the beam quality, the emittance can be defined by the area of an ellipse that can enclose the whole beam (black dashed ellipses in Fig. 3.3). This definition is well suited for verifying whether the entire beam can be transported by a beamline, provided the acceptance of the beamline is known. But this definition also has its drawbacks, since generally it is difficult to find a uniform criterion for the edge or boundary of a particle beam. Furthermore, this definition does not distinguish between different particle distributions, so the beam quality of the red beams in Fig. 3.3a and 3.3b would be identical even though the particles of the Gaussian distributed beam (Fig. 3.3b) are more clustered around their center.
Therefore, the Root Mean Square (RMS) emittance of the beam is specified most of the time, which is determined by the variance-covariance matrix:

$$\varepsilon_{\text{RMS}} = \varepsilon_{xx'}^{1\sigma} = \sqrt{\begin{vmatrix} \langle x \cdot x \rangle & \langle x \cdot x' \rangle \\ \langle x' \cdot x \rangle & \langle x' \cdot x' \rangle \end{vmatrix}} = \sqrt{\langle x^2 \rangle \langle x'^2 \rangle - \langle x \cdot x' \rangle^2}. \tag{3.21}$$

In some textbooks the emittance is defined as the area of the ellipse $A_{xx'} = E_x x' = \pi \varepsilon_{xx'}^{1\sigma}$. The unit π mm mrad is an indication for this with the pleasant side effect that the values $E_x x'$ and $\varepsilon_{xx'}^{1\sigma}$ are comparable without having to multiply either of them by π or $1/\pi$. The RMS emittance is refereed to as the 1σ-emittance and the $n\sigma$-emittance $(n \in [1, 2, 3])$ is simply defined as

$$\varepsilon_{xx'}^{n\sigma} = n^2 \varepsilon_{xx'}^{1\sigma}. \tag{3.22}$$

For ion beams, the 2σ-emittance is preferred, which is called effective RMS emittance and is used most of the time in this thesis. For a beam with an elliptical, Gaussian distributed particle distribution in phase space, the effective (2σ) emittance contains 86.47 % of the particles and the 3σ emittance 99.73 %. In this particular case the 3σ emittance therefore corresponds to the enclosed area as can be seen in Table 3.2 in which the emittance and the enclosed area of the beams shown in Fig. 3.3 are given.

Table 3.2: Emittance $\varepsilon_{xx'}^{3\sigma}$ and enclosed phase space area of the beams and ellipses shown in this Fig. 3.3.

Beam	$\varepsilon_{xx'}^{3\sigma}$ in mm mrad	Enclosed area in π mm mrad
Blue uniform beam (Fig. 3.3a)	399	180
Red uniform beam (Fig. 3.3a)	518	180
Black ellipse (Fig. 3.3a)	-	422
Blue Gaussian beam (Fig. 3.3b)	180	180
Red Gaussian beam (Fig. 3.3b)	238	180
Black ellipse (Fig. 3.3b)	-	422.28

In Table 3.2 it can also be seen that aberrations as well as different particle distributions are reflected by the RMS emittance, which makes this parameter a suitable quantity to describe the beam quality. In addition, the definition of the RMS emittance can also be extended to the six-dimensional phase space:

$$\left(\varepsilon_{6\mathrm{D}}^{1\sigma}\right)^2 = \begin{vmatrix} \langle x \cdot x \rangle & \langle x \cdot x' \rangle & \langle x \cdot y \rangle & \langle x \cdot y' \rangle & \langle x \cdot l \rangle & \langle x \cdot \delta \rangle \\ \langle x' \cdot x \rangle & \langle x' \cdot x' \rangle & \langle x' \cdot y \rangle & \langle x' \cdot y' \rangle & \langle x' \cdot l \rangle & \langle x' \cdot \delta \rangle \\ \langle y \cdot x \rangle & \langle y \cdot x' \rangle & \langle y \cdot y \rangle & \langle y \cdot y' \rangle & \langle y \cdot l \rangle & \langle y \cdot \delta \rangle \\ \langle y' \cdot x \rangle & \langle y' \cdot x' \rangle & \langle y' \cdot y \rangle & \langle y' \cdot y' \rangle & \langle y' \cdot l \rangle & \langle y' \cdot \delta \rangle \\ \langle l \cdot x \rangle & \langle l \cdot x' \rangle & \langle l \cdot y \rangle & \langle l \cdot y' \rangle & \langle l \cdot l \rangle & \langle l \cdot \delta \rangle \\ \langle \delta \cdot x \rangle & \langle \delta \cdot x' \rangle & \langle \delta \cdot y \rangle & \langle \delta \cdot y' \rangle & \langle \delta \cdot l \rangle & \langle \delta \cdot \delta \rangle \end{vmatrix} \approx \left(\varepsilon_{xx'}^{1\sigma} \cdot \varepsilon_{yy'}^{1\sigma} \cdot \varepsilon_{l\delta}^{1\sigma}\right)^2 . \tag{3.23}$$

Thereby δ is the momentum deviation and l the longitudinal location deviation as defined in Section 3.1. The approximation in Equation 3.23 is valid if there are no correlations between the vertical, horizontal and longitudinal coordinates of the beam, which is in general the case [Hinterberger, 2008]. However, this does not mean that the momentum of the particles has no effect on the emittance. The interrelationships will be briefly explained in the following.

3.5.1. Emittance and particle momentum

In the following, the influence of the particles' momentum on the emittance in different phase spaces and subspaces is considered. To distinguish between the phase space described by (x, p_x, y, p_y, z, p_z) and $(x, x', y, y', l, \delta)$, the latter is often times referred to as trace space in literature. The trace space area $A_{xx'}$ is related to the projection of the phase space volume in the x-p_x-plane by [Reiser et al., 2008]:

$$A_{xx'} = \frac{1}{p_s} \iint dx\, dp_x = \frac{1}{\beta\gamma mc} \iint dx\, dp_x . \tag{3.24}$$

So if there is an energy transfer ($\beta\gamma \neq \mathrm{const}$), the trace space area $A_{xx'}$ and, in implication, the emittance $\varepsilon_{xx'}$ would change. To circumvent this effect, the normalized emittance $\varepsilon_{n,xx'}$ is used

$$\varepsilon_{xp_x}^{2\sigma} = \varepsilon_{n,xx'}^{2\sigma} = \bar{\beta}\bar{\gamma}\varepsilon_{xx'}^{2\sigma} = 4\bar{\beta}\bar{\gamma}\varepsilon_{xx'}^{1\sigma} \tag{3.25}$$

with the mean values of the relativistic quantities $\bar{\beta} = \bar{v}_{\text{total}}/c$ and $\bar{\gamma} = \bar{E}/(m_0 c^2) + 1$. It is therefore important, that the normalized emittances are referred to when two particle beams with different mean energies are compared.

A momentum distribution can also affect the transverse particle beam profile. This occurs when the beam is projected onto an x-y plane at a specific point along the nominal trajectory which, for example, is done when measured and simulated beam profiles are compared. In linear beam optics a simple drift with the length L_d will change the horizontal location deviation x and the longitudinal location deviation l (see Section 3.1) of a particle as follows:

$$x = x_0 + L_d x', \quad l = \frac{\delta}{\gamma^2} L_d . \tag{3.26}$$

A detector on the x-y-plane would however measure the horizontal location deviation

$$\hat{x} = x_0 + (L_d + l)x' = x_0 + (1 + \frac{\delta}{\gamma^2}) L_d x' . \tag{3.27}$$

For $\delta = 0$ the emittance $\varepsilon_{\hat{x}x'}$ would remain constant, and therefore it changes in case of $\delta \neq 0$ for an increasing drift length L_d. Since typically the momentum deviation is quite small ($\delta \ll 1$) this effect can

usually be neglected. However, it should be noted that in this work the ion beam is always projected onto the x-y plane at a particular point along the nominal trajectory.
The RMS emittance was thus found to be a suitable parameter for quantifying the beam quality. To investigate the extent to which the ion beam shaping at the LIGHT beamline changes the emittance, the trajectories of the particles are determined numerically in this thesis. This will now be discussed in the following section.

3.6. Particle beam tracking with the MATLAB ODE solver

In general, accelerator simulation codes can be classified into two types: matrix codes and numerical field models [Kalvas, 2014]. Matrix codes use the analytical transport matrices for each accelerator element up to a given order and combine them to create a comprehensive mathematical description of the accelerator through which the particles can then be tracked. This approach is particularly well suited for large accelerator structures with many elements of the same type. In numerical simulations, the three-dimensional electromagnetic field of each element is determined and the particle tracking through those fields is then achieved by finite element modelling. Since the LIGHT beamline consists of only five elements (two solenoids and three accelerating gaps) and it should also be possible to investigate the influence of different magnetic field distributions of the solenoids on the particle beam, the numerical approach was chosen for this work. The trajectories of the particles are only changing due to electromagnetic forces and can therefore be fully explained by the Lorentz equation [Demtröder, 2013]:

$$\mathbf{F} = \frac{d}{dt}\left(\gamma m_0 \dot{\mathbf{r}}\right) = \frac{d}{dt}\left(\frac{m_0 \dot{\mathbf{r}}}{\sqrt{1-\left(\frac{\dot{\mathbf{r}}}{c}\right)^2}}\right) = q\left(\mathbf{E} + \dot{\mathbf{r}} \times \mathbf{B}\right). \tag{3.28}$$

Thereby γ is the Lorentz factor, c the speed of light, **E** the electric field, **B** the magnetic field, m_0 the resting mass, $\dot{\mathbf{r}}$ the velocity and q the charge of the ion. The numerical solving of this differential equation is done with the MATLAB Ordinary Differential Equation (ODE) suite [Shampine and Reichelt, 1997]. The ODE suite is capable to solve first-order equations with various Runge–Kutta methods [Rannacher, 2017]. Therefore, the Lorentz equation has to be rewritten to a first-order equation. The substitutions

$$x_1 = x, x_2 = \dot{x}, y_1 = y, y_2 = \dot{y}, z_1 = z, z_2 = \dot{z}, \tag{3.29}$$

are leading to the following first-order equations:

$$\begin{aligned}
\dot{x_2} &= \frac{q}{\gamma m} \cdot \left(\left(y_2 \cdot B_z - z_2 \cdot B_y\right) + E_x\right), \\
\dot{y_2} &= \frac{q}{\gamma m} \cdot \left(\left(z_2 \cdot B_x - x_2 \cdot B_z\right) + E_y\right), \\
\dot{z_2} &= \frac{q}{\gamma m} \cdot \left(\left(x_2 \cdot B_y - y_2 \cdot B_x\right) + E_z\right).
\end{aligned} \tag{3.30}$$

In the presence of an electric field **E** it has to be considered that the Lorentz factor is time dependent $(\gamma = \gamma(t))$ which is taken into account by recalculating it for each step. For the simulations in this work, the Dormand–Prince method [Dormand and Prince, 1978, 1980] is used. It is an adaptive Runge–Kutta method that calculates the fourth- and fifth-order accurate solution for each step and if the deviation between these two solution is too large, the incremental step size is decreased. For the simulations shown in this thesis, a relative tolerance of 10^{-5} and an absolute tolerance of 10^{-8} m is used.

With the MATLAB ODE solver and the initial ion beam parameters (see Section 2.3), the trajectories of the particles can be determined for arbitrary electric and magnetic fields and thus also the influence of these fields on the beam quality. However, at its current state the simulation code does not take into account the self-generated electric and magnetic fields of the particles, which can influence the beam dynamics at very high particle fluxes. Therefore, in the final section of this chapter, the main effects of these self-generated fields are discussed.

3.7. Space charge effects

The forces on the particles of the beam due to their self-generated fields, referred to as space charge effects, cannot be neglected, especially for high particle fluxes. In the following, the most important information regarding the influence of space charge effects on the beam dynamics are provided. This section is based on [Reiser et al., 2008] where also more details on this topic can be found.

Space charge effects can be described by the sum of a "collision" force and a "smooth" force. The collision force is the interaction of the particles with their immediate neighbors, which causes statistical fluctuations in the particle distribution. In contrast, the smooth force raises from a collective potential of the beam and ultimately leads to a defocusing or an acceleration. To estimate the relative importance of these two effects, the particle beam can be considered as a non-neutral plasma, which exhibits a similar collective behavior as a neutral plasma. Thus, a local perturbation in the charge distribution of a beam with transverse temperature T and density n, confined by external focusing fields, will be screened off in a distance corresponding to the Debye length

$$\lambda_\mathrm{D} = \frac{\hat{v}_x}{\omega_\mathrm{p}} = \left(\frac{\epsilon_0 k_\mathrm{B} T}{q^2 n}\right)^{1/2} . \tag{3.31}$$

Thereby, $\hat{v}_x$ is the transverse RMS velocity and ω_p the plasma frequency. If the Debye length is large compared to the beam radius ($\lambda_\mathrm{D} \gg r_0$), the single particles are not screened and collisions will lead to statistical fluctuations of the particle distribution. However, for the beam parameters achieved in this thesis as well as for most beams of practical interest, the Debye length is small compared to the beam radius ($\lambda_\mathrm{D} \ll r_0$) and therefore collective effects will dominate [Reiser et al., 2008].

The collective effects are mainly leading to a defocusing force as well as an acceleration of the particles. By assuming a cylindrical beam cross-section with a homogeneous particle density ρ, the focusing strength caused by collective space charge effects is [Reiser et al., 2008]:

$$\kappa_\mathrm{sc} = \frac{K}{r_0^2} = \frac{qI}{2\pi\epsilon_0 m \beta^3 c^3 \gamma^3 r_0^2}(1-\gamma^2 f_\mathrm{e}). \tag{3.32}$$

Thereby $f_\mathrm{e} \in [0,1]$ is the space charge neutralization factor, I the beam current, r_0 the beam radius and K the generalized perveance. For a charge neutralized beam ($f_\mathrm{e} \approx 1$), e.g. an unaffected ion beam generated by the TNSA mechanism near its origin, the defocusing due to collective space charge effects vanishes for non-relativistic beams ($\gamma \approx 1$), whereas for a complete unneutralized beam it is $f_\mathrm{e} = 0$. In the derivative of the focusing strength κ_sc in [Reiser et al., 2008] it is assumed that the variation of the beam radius r_0 with axial distance is slow enough that axial electric field components E_z and radial magnetic field components B_r can be neglected. But for the ion bunch parameters that can be achieved with the LIGHT beamline this assumption is not valid. Therefore, in the following, the axial electric field E_z caused by space charge effects is estimated for a particle at the beam's edge. As it is done for the derivative of the focusing strength κ_sc in [Reiser et al., 2008], a cylindrical beam cross-section with a homogeneous particle density ρ is assumed.

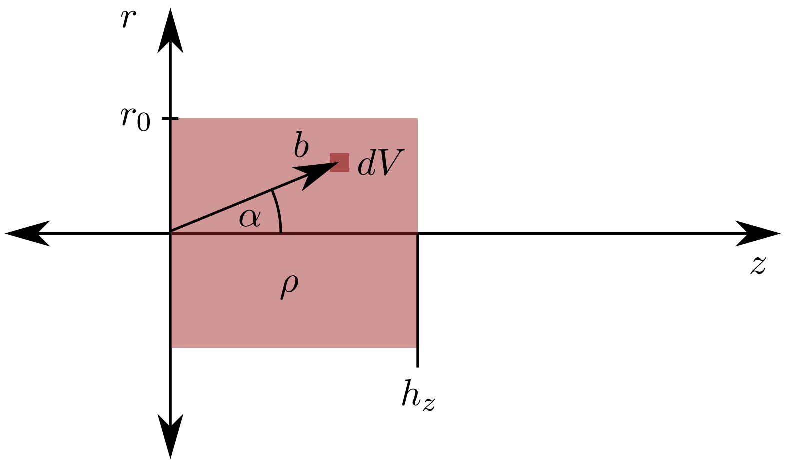

Fig. 3.4: Relation between the variables used to calculate the electric field of a particle located on the axis and at the edge of the beam for a cylindrical beam cross-section with a homogeneous particle density ρ.

The beam radius is r_0 and the axial expansion of the beam (cylinder height) is h_z (see Fig. 3.4). Then the electric field acting on a particle, that is located on the beam's axis $(r = 0)$ as well as on the beam's edge $(z = 0)$, can be determined by Coulomb's law [Demtröder, 2013]:

$$\mathbf{E} = \frac{1}{4\pi\epsilon_0} \int \frac{\hat{\mathbf{b}}}{|\mathbf{b}|^2} \rho(\mathbf{b})\, dV, \tag{3.33}$$

with $\hat{\mathbf{b}} = \mathbf{b}/|\mathbf{b}|$. Since $\mathbf{b}^2 = \mathbf{z}^2 + \mathbf{r}^2$, $\cos(\alpha) = z/b$ and $E_z = -|\mathbf{E}|\cos(\alpha)$ as shown in Fig. 3.4 as well as $\rho(\mathbf{b}) = \rho$ it follows:

$$E_z = -\frac{\rho}{4\pi\epsilon_0} \int_0^{h_z} \int_0^{r_0} \int_0^{2\pi} \cos(\alpha) \frac{r}{b^2}\, dz\, dr\, d\phi, \tag{3.34}$$

$$E_z = -\frac{\rho}{2\epsilon_0} \int_0^{h_z} \int_0^{r_0} \frac{zr}{(r^2 + z^2)^{3/2}}\, dz\, dr, \tag{3.35}$$

$$E_z = -\frac{\rho}{2\epsilon_0} \left(r_0 + h_z - \sqrt{h_z^2 + r_0^2} \right). \tag{3.36}$$

The Equations 3.32 and 3.36 are used in this thesis to estimate whether space charge effects can be neglected or if they could cause deviations between simulations and experimental data.

With the parameters and concepts that have been introduced in this chapter, the transport and the longitudinal ion beam shaping at the LIGHT beamline will now be investigated in the following chapters.

4. Beam transport with solenoid magnets

In this chapter, the transport of laser-accelerated ion beams with pulsed, high field solenoid magnets is investigated. Therefore, the focusing effect of the solenoid magnets is explained first by considering the motion of a charged particle in their magnetic field. After that, the focal spot size of an initially parallel ion beam that was focused by a solenoid magnet is estimated, taking into account the spherical and chromatic aberration of the solenoid. Subsequently, the technical design of the pulsed, high-field solenoid magnets used at the LIGHT beamline are presented, and their magnetic field distribution is determined for a simplified coil geometry. Finally, in the last section of this chapter, the capturing of the TNSA-generated proton beam at the LIGHT beamline is analyzed with numerical simulations.

4.1. Motion of charged particles in solenoid magnets

The equations and results used in this section can be found in [Kumar, 2009]. In the following, a particle with an initial direction deviation of zero is considered in the following axisymmetric magnetic field:

$$B_z(r,z) = B(z) - \frac{r^2}{4}B''(z) + \dots, \tag{4.1}$$

$$B_r(r,z) = -\frac{r}{2}B'(z) + \frac{r^3}{16}B'''(z) + \dots\ . \tag{4.2}$$

Thereby, z is the solenoid axis and r the radial distance to this axis. For simplification, only terms up to the first order of r are assumed, as well as $B(z) = B_0$ inside and $B(z) = 0$ outside the solenoid. Furthermore, the magnetic field $B(z)$ shall drop to zero abruptly at the edges of the solenoid. Then the Equations 4.1 and 4.2 can be written as

$$B_z(r,z) = B_0[u(z) - u(z - L_{\text{sol}})], \tag{4.3}$$

$$B_r(r,z) = -\frac{r}{2}B_0[\delta(z) - \delta(z - L_{\text{sol}})], \tag{4.4}$$

with the Dirac delta function $\delta(z)$, the length of the solenoid L_{sol} and the Heaviside step function $u(z)$. So, a charged particle that enters the solenoid ($z = 0$) experiences a kick due to the magnetic field $B_r(r,z) = -\frac{r_0}{2}B_0$. This results in an azimuthal velocity

$$\Delta v_\theta = \frac{r_0}{2}\frac{eB_0}{\gamma m} = r_0\omega_{\text{L}} = 2r_0\omega_{\text{c}}. \tag{4.5}$$

Thereby, r_0 is the initial distance of the particle to the solenoid axis, ω_{L} the Larmour frequency and ω_{c} the cyclotron frequency. Afterwards the particle is effected by the magnetic field $B_z(r,z) = B_0$, which causes it to move on a helical trajectory (see Fig. 4.1) with the radius

$$R_{\text{c}} = \frac{\gamma m v_\theta}{eB_0} = \frac{r_0}{2}. \tag{4.6}$$

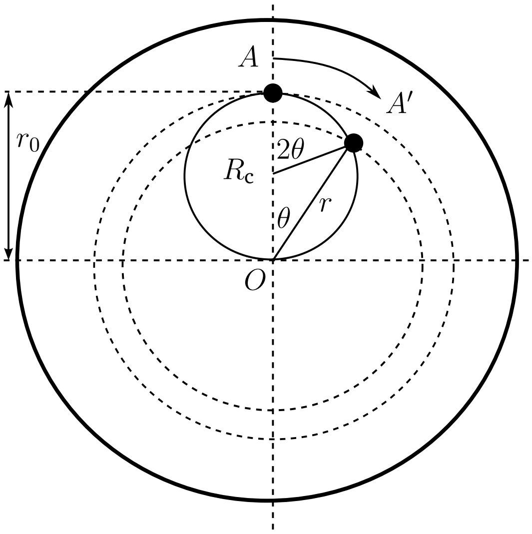

Fig. 4.1: Motion of a charged particle within a solenoid magnet.

The radial and azimuthal velocities of the particle on this trajectory are

$$\begin{aligned} v_r &= -r\omega_\mathrm{L} \tan\left(\frac{\omega_\mathrm{L} z}{v_z}\right), \\ v_\theta &= r\omega_\mathrm{L}. \end{aligned} \tag{4.7}$$

When the particle exits the solenoid it experiences a kick again, but this time the radial magnetic field is directed away from the solenoid axis $B_r(r,z) = \frac{r}{2}B_0$ and therefore cancels out the azimuthal velocity v_θ. The radial velocity on the other hand is not effected by the radial magnetic field, thus the particle moves towards the z axis after the solenoid. If for the length of the solenoid $L_\mathrm{sol} \ll v_z/\omega_\mathrm{L}$ applies (thin lens approximation), the small angle approximation can be used and the focal length of the solenoid can be written as

$$\frac{1}{f} = \left(\frac{qB_0}{2\gamma m v_z}\right)^2 \cdot L_\mathrm{sol} = \left(\frac{\omega_\mathrm{L}}{\beta c}\right)^2 \cdot L_\mathrm{sol}. \tag{4.8}$$

By further assuming that the radial coordinate r_0 does not change significantly in the solenoid, the stepwise usage of Equation 4.8 leads to the more general equation [Kumar, 2009]:

$$\frac{1}{f} = \left(\frac{q}{2\gamma m v_z}\right)^2 \int_{z1}^{z2} B_z^2 dz. \tag{4.9}$$

Due to the dependency of the focal length from the square of the particles' momentum $p_z = mv_z$ a solenoid can be used as an energy selector, which is one of the tasks of the solenoid magnets in this thesis. But it also causes the chromatic aberration of the solenoid. In addition, the second term in Equation 4.1 can not be neglected in a more realistic magnetic field distribution of the solenoid magnet. Therefore, particles with a larger distance to the solenoid axis experience a stronger magnetic field B_z, which causes a spherical aberration. This will be explained in more detail in the next section by an estimation of the influence of these effects on the focal spot size of an ion beam that is focused by a solenoid magnet.

4.2. Ion beam focusing with solenoid magnets

In this section, the focal spot size of an initially parallel ion beam that is focused by a solenoid magnet is estimated. This section is inspired by [Chen, 2003], in which similar results are found.
Let $z = 0$ be just behind a focusing solenoid, $r(z = 0) = r_0$ the initial beam radius and ε the emittance of the beam in front of the solenoid. So for $z \geq 0$ the beam propagates freely (no magnetic or electric field is present). In this case, the beam radius can be described by the Lee-Cooper's envelope equation [Lee and Coopert, 1976; Reiser et al., 2008]:

$$r''(z) = \frac{\varepsilon^2}{r(z)^3}. \tag{4.10}$$

Multiplying both sides by r' and integrating from $z_1 = 0$ to $z_2 = z$ results in

$$(r_0')^2 - (r')^2 = \frac{\varepsilon^2}{r^2} - \frac{\varepsilon^2}{r_0^2}, \tag{4.11}$$

since

$$\int r'r''dz = \frac{1}{2}(r')^2, \quad \int \frac{r'}{r^3}\,dz = -\frac{1}{2r^2}. \tag{4.12}$$

By defining the constant $C^2 = (r_0')^2 + \varepsilon^2/r_0^2$, Equation 4.11 can be rearranged as follows:

$$\frac{r'r}{\sqrt{r^2 - \varepsilon^2/C^2}} = -C. \tag{4.13}$$

Again, integrating from $z_1 = 0$ to $z_2 = z$ leads to

$$\sqrt{r_0^2 - \varepsilon^2/C^2} - \sqrt{r^2 - \varepsilon^2/C^2} = Cz, \tag{4.14}$$

since

$$\int \frac{r'r}{\sqrt{r^2 - \varepsilon^2/C^2}}\,dz = \sqrt{r^2 - \varepsilon^2/C^2}. \tag{4.15}$$

Now the following two assumptions are made from this point on:

1. The beam was parallel before it entered the solenoid, so behind the solenoid the direction deviation is $|r'(z = 0)| = |r_0'| = r_0/f_0$, with f_0 being the focal length of the solenoid as derived in the previous subsection (see Equation 4.8).
2. The focal spot size will be much smaller than the initial beam ($r_0|r_0'| \gg \varepsilon$).

From the second assumption it follows:

$$\frac{\varepsilon^2}{C^2} = \frac{\varepsilon^2}{(r_0')^2 + \varepsilon^2/r_0^2} \approx \frac{\varepsilon^2}{(r_0')^2} \tag{4.16}$$

and

$$\sqrt{r_0^2 - \varepsilon^2/(r_0')^2} \approx r_0. \tag{4.17}$$

This can be substituted in Equation 4.14, which leads to

$$r_0 - \sqrt{r^2 - \varepsilon^2/(r_0')^2} = zr_0'. \tag{4.18}$$

Rearranging for $r(z)$ yields

$$r^2(z) = \frac{\varepsilon^2}{(r_0')^2} + (r_0 - z r_0')^2. \tag{4.19}$$

Therefore, the minimum focal spot size is at the position $z = f_0 = r_0/\left|r_0'\right|$:

$$r^2(f_0) = r_{f_0}^2 = \left(\frac{\varepsilon f_0}{r_0}\right)^2. \tag{4.20}$$

Now the effect of the chromatic and the spherical aberration on this focal spot size is investigated. Both aberrations cause a slight deviation of the focal length Δf. Let $f = f_0 + \Delta f$, so that $f = r_0/\left|\tilde{r}_0'\right|$ as shown in Fig. 4.2.

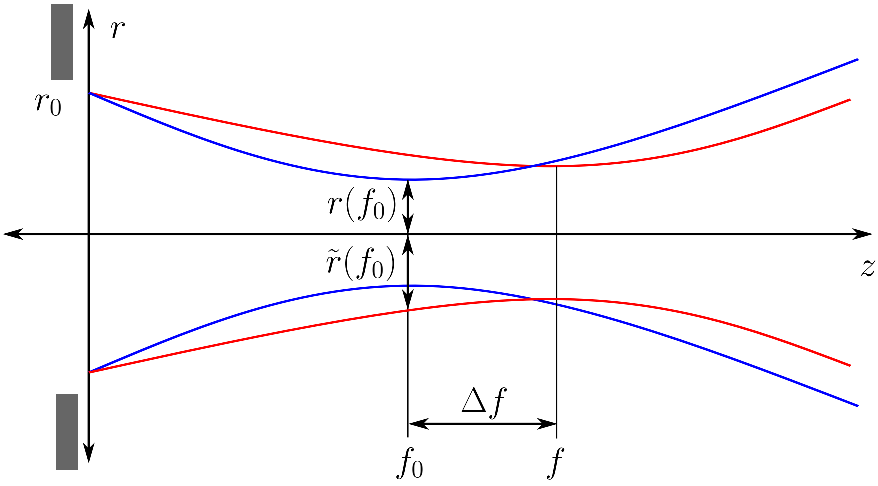

Fig. 4.2: Relationship of the variables in Equation 4.24.

With these definitions, Equation 4.19 can be rewritten as follows:

$$\begin{aligned}
\tilde{r}^2(f_0) &= \frac{\varepsilon^2}{(\tilde{r}_0')^2} + (r_0 - f_0 \tilde{r}_0')^2 && (4.21)\\
&= \left(\frac{\varepsilon f}{r_0}\right)^2 + r_0^2 \left(1 - \frac{f_0}{f}\right)^2 && (4.22)\\
&= \left(\frac{\varepsilon f_0}{r_0}\right)^2 + \left(\frac{\varepsilon \Delta f}{r_0}\right)^2 + 2 f_0 \Delta f \left(\frac{\varepsilon^2}{r_0^2}\right) + r_0^2 \left(\frac{\Delta f}{f}\right)^2 && (4.23)\\
&\approx \left(\frac{\varepsilon f_0}{r_0}\right)^2 + r_0^2 \left(\frac{\Delta f}{f}\right)^2. && (4.24)
\end{aligned}$$

In the last step, the assumption $r_0 \gg \Delta f$ is made. By substituting $\Delta f = \Delta f_{C_s} + \Delta f_\delta$, with the focal length deviations due to chromatic aberration $\Delta f_\delta / f$ and the focal length deviations due to spherical aberration $\Delta f_{C_s}/f$ into Equation 4.24, one obtains

$$\tilde{r}^2(f_0) \approx \left(\frac{\varepsilon f_0}{r_0}\right)^2 + \left(\frac{r_0 \Delta f_\delta}{f}\right)^2 + \left(\frac{r_0 \Delta f_{C_s}}{f}\right)^2 + \left(\frac{2 r_0^2 \Delta f_\delta \Delta f_{C_s}}{f^2}\right). \tag{4.25}$$

Now the focal length deviations $\Delta f_\delta / f$ and $\Delta f_{C_s}/f$ are determined for a solenoid and substituted in Equation 4.25. The focal length deviation $\Delta f_\delta / f$ can be directly determined by the partial derivative of the focal length of the solenoid (see Equation 4.8). For a non-relativistic particle it is

$$\frac{\partial f}{\partial \gamma} \ll \frac{\partial f}{\partial p} \tag{4.26}$$

and therefore

$$\frac{\partial f}{\partial p} = \frac{2f}{p} \approx \frac{\Delta f_\delta}{\Delta p} \rightarrow \frac{\Delta f_\delta}{f} \approx 2\delta. \tag{4.27}$$

The spherical aberration is a direct consequence of the variation of the magnetic field $B_z(r,z)$ on the radial distance, so the higher order terms in Equation 4.1. Including the second order term of $B_z(r,z)$ in Equation 4.9 leads to

$$\frac{1}{f_{C_\mathrm{s}}} = \left(\frac{q}{2\gamma m v_z}\right)^2 \left(\int B_z^2 dz - \frac{r^2}{2}\int B_z B_z'' dz + \frac{r^4}{16}\int (B_z'')^2 dz\right). \tag{4.28}$$

By assuming $\int (B_z'')^2 dz \approx 0$ and defining the spherical aberration coefficient as

$$C_\mathrm{s} = \frac{1}{2}\frac{\int B_z B_z'' dz}{\int B_z^2 dz}, \tag{4.29}$$

the focal length deviation caused by the spherical aberration is approximately

$$\frac{f}{f_{C_\mathrm{s}}} \approx 1 - C_\mathrm{s} r_0^2 \rightarrow \frac{\Delta f_{C_\mathrm{s}}}{f_{C_\mathrm{s}}} \approx -C_\mathrm{s} r_0^2 \approx \frac{\Delta f_{C_\mathrm{s}}}{f}. \tag{4.30}$$

According to [Scherzer, 1936], the spherical aberration coefficient C_s is always positive. Therefore, $\Delta f_{C_\mathrm{s}}/f$ is always negative and cannot be compensated in terms of linear ion optics. Substitution of Equation 4.30 and 4.27 in Equation 4.25 then results in the following estimation for the focal spot size:

$$(\tilde{r}_{f_0})^2 \approx \left(\frac{\varepsilon f_0}{r_0}\right)^2 + (2r_0\delta)^2 + \left(C_\mathrm{s} r_0^3\right)^2 - \left(4r_0^4 \delta C_\mathrm{s}\right). \tag{4.31}$$

The last term in Equation 4.31 ensures, that the focal length deviation of the chromatic and the spherical aberration compensate each other in the case of $C_\mathrm{s} r_0^2 = 2\delta \leftrightarrow -\Delta f_{C_\mathrm{s}}/f = \Delta f_\delta / f$. But if the mean focal spot size of many particles with an axisymmetric energy distribution, and without any correlation between $r_{0,i}$ and δ_i is determined, the term vanishes since

$$\frac{1}{N}\sum_{i=1}^{N} r_{0,i}^4 \delta_i \approx 0. \tag{4.32}$$

Since the minimum focal spot size is directly related to the emittance, Equation 4.31 can also be used as a scaling law for the emittance growth that is caused by the aberrations. This will be verified with simulations in the last section of this chapter. In the next two sections, the technical design of the pulsed high-field solenoid magnets used at the LIGHT beamline and the determination of their magnetic field distribution will be explained first.

4.3. Technical design of the pulsed, high-field solenoid magnets

The pulsed high-field solenoid magnets used in this work were designed and constructed by the High-Field Laboratory (HLD) at HZDR. The coil itself has a length of 150 meters with 112 evenly distributed windings in four layers. The wire has a cross-section of $(4.3 \times 2.8)\,\mathrm{mm}^2$ and is wrapped around a cylindrical, Fiber Reinforced Plastic (FRP) coil body with an inner diameter of 46 mm and an outer diameter of 54 mm. Each layer is isolated by at least 1.5 mm Zylon-epoxy composite. The coil can in principle be operated in a vacuum, but to prevent outgassing of the Zylon-epoxy and to reduce the breakdown voltage in accordance to Paschen's law, the coil is usually located in a stainless steel housing and connected to the outside air volume. This housing reduces the open aperture of the solenoid to 40 mm. In Fig. 4.3 a technical drawing of the design is illustrated.

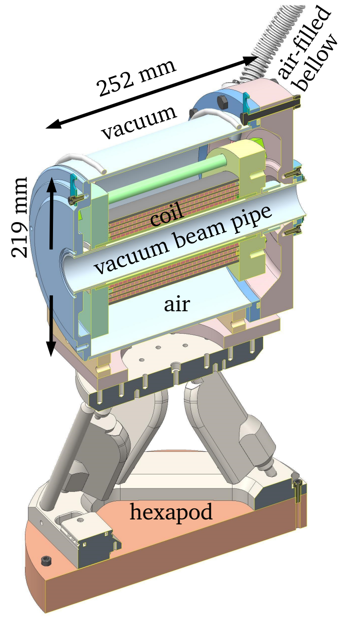

Fig. 4.3: Cutaway view of the pulsed, high-field solenoid magnet with stainless steel housing, which is mounted on a hexapod [Kroll, 2018].

The coil can be operated with a peak current of up to 23.4 kA, which corresponds to a magnetic field of 19.7 T in the center of the solenoid. Such high currents are provided by a specially designed, capacitor-based pulse generator with a capacity of 180 µF. The following equation is a good estimation for the maximum magnetic field strength of the solenoid [Busold, 2014; Kroll, 2018]:

$$B_0 = B_{z,\mathrm{max}} \approx 0.84 \times I \approx 0.55 \times U. \tag{4.33}$$

Thereby, I is the current of the generated pulse and U is the voltage of the pulse generator. When the solenoid magnet is pulsed, its temperature increases. Therefore, the repetition rate of the setup is limited by the energy of the pulse that is provided to the solenoid. For full energy pulses, one shot per minute for several minutes is tolerable [Kroll, 2018].

4.3.1. Magnetic field distribution of the solenoid magnets

For the determination of a magnetic field distribution of the solenoid magnets for the simulation studies of this work, the coil geometry is reconstructed with many straight line wires and the magnetic field of those are then calculated with the Biot-Savart law [Demtröder, 2013]:

$$\mathbf{B}(\mathbf{r}) = \frac{\mu_0}{4\pi} \int_C \frac{I\, d\boldsymbol{l} \times \mathbf{r}'}{|\mathbf{r}'|}. \tag{4.34}$$

Thereby, $d\boldsymbol{l}$ is a vector along the path C, $\mathbf{r}' = \mathbf{r} - \boldsymbol{l}$ and I the current. The sum of all the individual magnetic fields then results in the magnetic field of the solenoid magnet. The reconstructed coil is shown in Fig. 4.4. It contains of 100 (4 × 25) ring wires and has a length of 150 mm. Then, a current of 1 A is used to determine a 41 × 41 × 481 mm³ field map with a grid size of 1 mm for each magnetic field direction. In Fig. 4.5 the y-z-plane $(x = 0)$ of these field maps are shown. The coordinate systems in Fig. 4.4 and Fig. 4.5 are identical, so the front side of the coil has a distance of 80 mm to the origin of the coordinate system. It can be seen, that at the entrance $(z = 80\,\mathrm{mm})$ and the exit $(z = 230\,\mathrm{mm})$ of the coil the magnetic field is mainly directed towards the radial direction which corresponds to the y-direction in the y-z-plane, whereas inside the coil, the magnetic field is directed towards the z-direction.

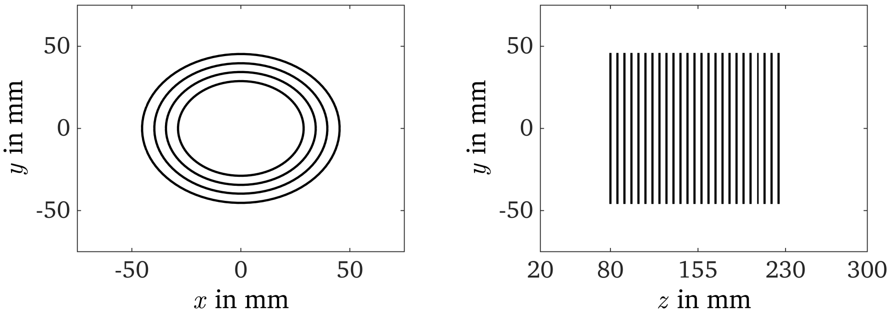

Fig. 4.4: Simplified coil geometry of the solenoid magnet used at the LIGHT beamline. This geometry consists of many straight line wires and was used in this section to determine field maps for the simulation studies of this work.

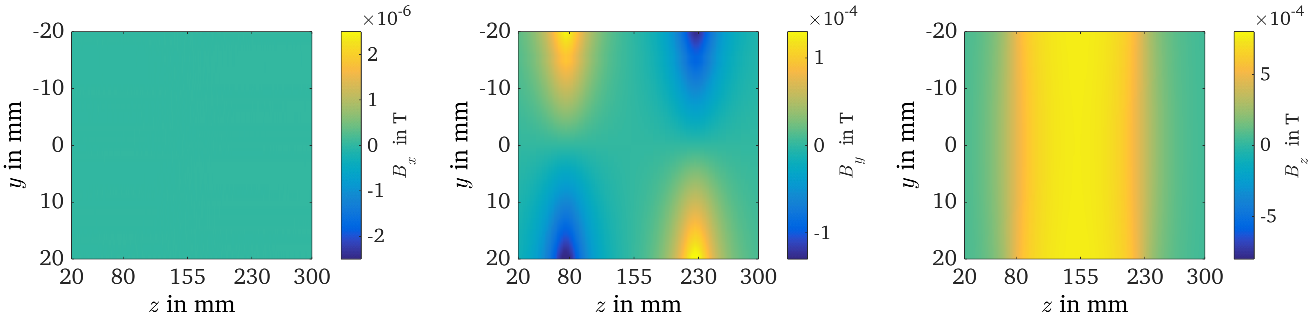

Fig. 4.5: The y-z-plane $(x = 0)$ of the field maps that have been determined with the Biot-Savart law (see Equation 4.34) and the coil geometry shown in Fig. 4.4.

The presented or similar field maps will now be used to simulate the capturing of laser-accelerated proton beams at the LIGHT beamline.

4.4. Simulation studies on capturing laser-accelerated proton beams

This section is divided into three subsections. In Subsection 4.4.1 the required magnetic field strength for collimating TNSA-generated protons with a specific energy is determined as well as the maximum initial divergence angle that the LIGHT beamline can capture. Then the emittance growth that results from the capturing process is analyzed in Subsection 4.4.2 and finally, in Subsection 4.4.3, the influence of different magnetic field distributions on the properties of the transported ion beam is investigated.

4.4.1. Energy selection and capture efficiency

In most of the experimental campaigns with the LIGHT beamline, protons with an energy of about 8 MeV were transported since the RF cavity is designed for ions with an energy per mass of 8 MeV u^{-1}. The typical setup of the LIGHT beamline in the experiments in which protons with 8 MeV are targeted is shown in Fig. 4.6. This setup will be used for the following simulations.

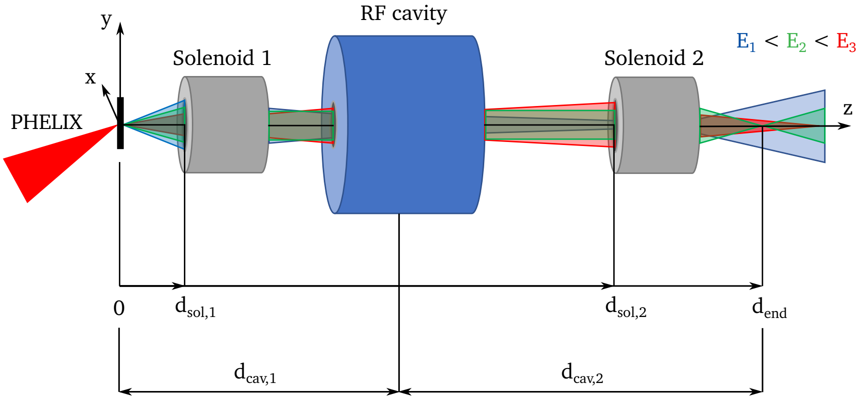

Distance	Length
$d_{\text{sol},1}$	40 mm
$d_{\text{sol},2}$	5400 mm
d_{end}	5700 mm
$d_{\text{cav},1}$	2275 mm
$d_{\text{cav},2}$	3425 mm

Fig. 4.6: Setup of the LIGHT beamline which is typically used for handling protons with 8 MeV.

For the numerical simulations, the initial proton beam is generated first as described in Section 2.3. Therefore, the parameters shown in Table 4.1 are used, which have been determined by fits to RIS data in [Busold, 2014].

Table 4.1: Parameters that were used to generate the initial proton beam in the simulations of this section. The values have been determined by fits to RIS data in [Busold, 2014].

N	$k_B T$	E_{min}	E_{max}	E_{cut}	a_2	a_1	a_0	m	q
5×10^6	6 MeV	2 MeV	22 MeV	28 MeV	-0.04 °/MeV^2	0.41 °/MeV	26.47 °	1 u	1 e

The resulting energy spectrum as well as the correlations between the location deviation x, the direction deviation x', the divergence angle θ and the energy E of the generated particles are shown in Fig. 4.7. It can be seen, that the number of protons is decreasing exponentially to higher energies, whereas the corresponding source size and divergence increases.
The trajectories of these protons are then determined with the procedure that has been described in Section 3.6. In the simulations that will be presented in this subsection, the field maps determined in the previous section are used for the first solenoid while the RF cavity and the second solenoid are only

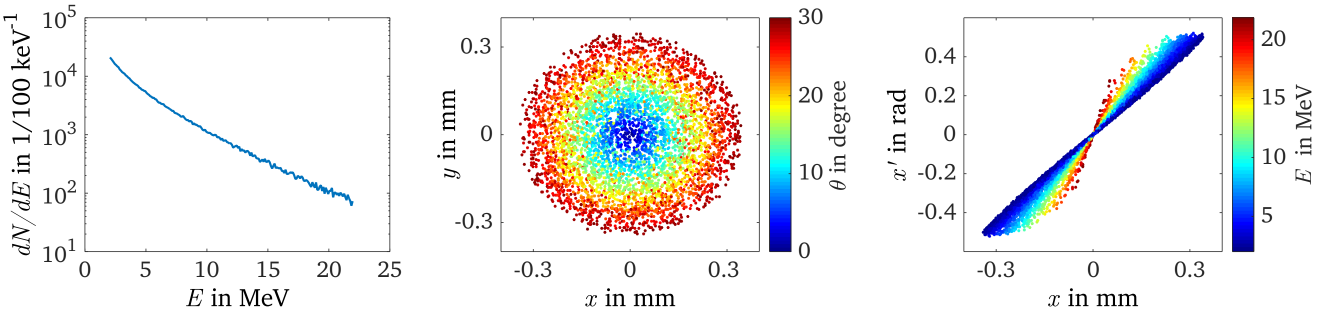

Fig. 4.7: Energy spectrum as well as the correlations between the location deviation x, the direction deviation x', the divergence angle θ and the energy E of a reconstructed TNSA-generated proton beam at its origin.

implemented as drift tubes. Since the field maps have been determined for a current of 1 A, the field strength is simply adjusted by multiplying the entire field map by the desired current. It should also be noted at this point, that the magnetic field is linearly interpolated for the positions of the protons during the calculation process in all simulations of this work.

In Fig. 4.8 the resulting energy distributions of the proton bunches at a distance of 5.7 m to their origin are shown for different currents supplied to the first solenoid. Due to the dependence of the focal length of the solenoid on the particle momentum (see Eq. 4.7), and the limited apertures of the solenoids (40 mm) and the RF cavity (35 mm), only a certain energy range of the proton beam reaches the end of the beamline.

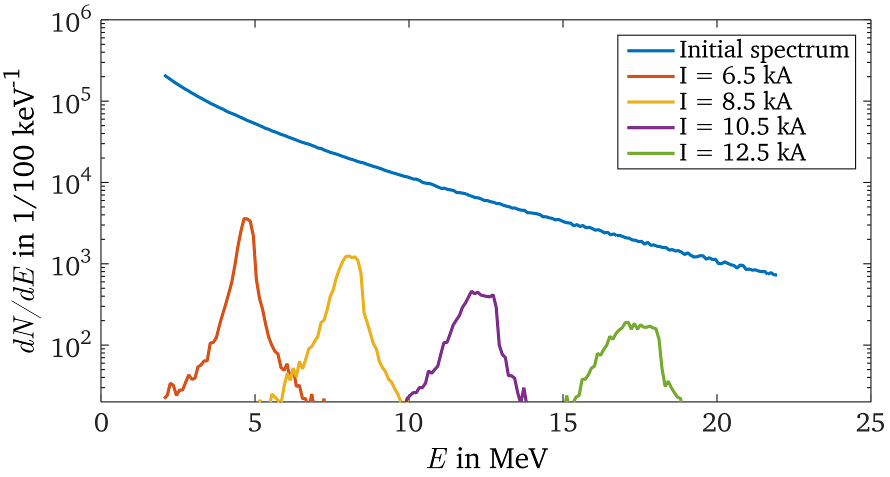

Fig. 4.8: Energy distributions of the proton bunches at the LIGHT beamline 5.7 m behind their origin. The color of the lines corresponds to the current supplied to the first solenoid. The energy spectrum of the protons at their origin is also shown in blue.

Since $f^{-1} \propto (qB_0/p)^2 \propto (qI/p)^2$ (see Equation 4.33 and Equation 4.8), it is expected, that the relation between I and E for non-relativistic protons ($\gamma = 1, p = \sqrt{2mE}, q_1 = q_2$ and $m_1 = m_2$) is

$$I_2 = \sqrt{\frac{E_2}{E_1}} \cdot I_1 \tag{4.35}$$

under the assumption that the focal length f is identical for the collimation of any particle ($f_1 = f_2$), which can be confirmed. The relative energy spread of the transported proton bunch is approximately $\Delta E/E_{\text{peak}} \approx 10\,\%$ (FWHM) for all currents shown. Due to the smaller initial direction deviation of protons with higher energies, the transport efficiency in the corresponding energy interval ($\Delta E/E_{\text{peak}} = 10\,\%$) increases from 8.43 % ($E_{\text{peak}} = 4.75\,\text{MeV}$) to 13.40 % ($E_{\text{peak}} = 17.5\,\text{MeV}$).

According to the simulation, for a current of 8.5 kA most of the protons that are reaching the end of the beamline have an energy of 8.3 MeV. Therefore, the current that is necessary to transport 8 MeV protons is 8.34 kA in the simulation. But since the solenoid in the experiment has 112 windings and the coil which was used to generate the field map for these simulations has only 100 windings, the required current in the experiment is expected to be 7.45 kA.

Lastly, these simulations are also used to determine the opening angle that the solenoid is able to capture. For this purpose, the distributions of the initial direction deviations of the transported beams are illustrated in Fig. 4.9. The maximum initial direction deviation of all the shown distributions is 130 mrad (≈ 7.5°), which is a clear indication that this is the maximum opening angle that the solenoid magnet is able to capture for the used setup.

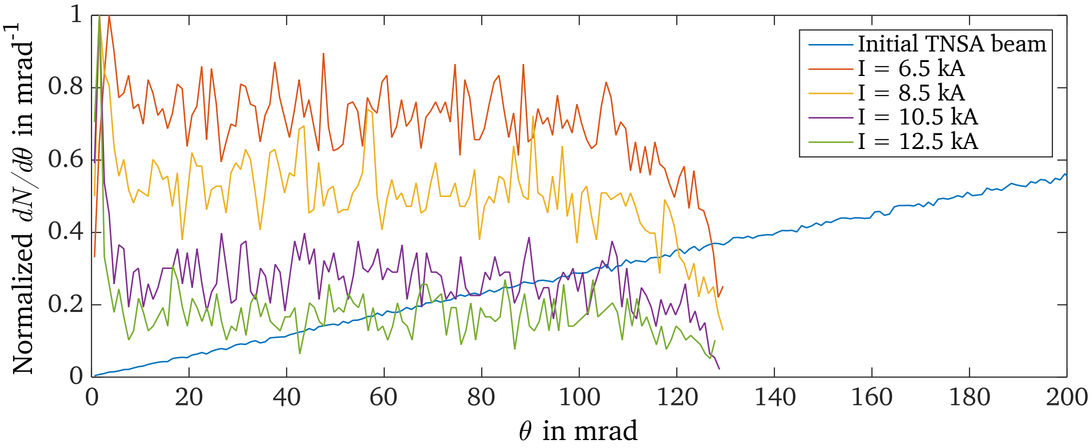

Fig. 4.9: Normalized distributions of the initial divergence angle θ of the proton bunches that reach the end of the LIGHT beamline in the simulation in case of the setup shown in Fig. 4.6. The normalized distribution of the initial ion beam is shown in blue. The colors of the other lines correspond to the respective currents supplied to the first solenoid, which in turn corresponds to the energy distributions of the transported proton bunches, as shown in Fig. 4.8.

For an energy spread of $\Delta E/E_{\text{peak}} \approx 10\,\%$ (FWHM) and a maximum initial divergence of 130 mrad (≈ 7.5°) it can be expected, that the beam quality was degraded due to the chromatic and the spherical aberration of the solenoid which will now be investigated in the next subsection.

4.4.2. Quantification of the spherical and chromatic aberrations

Since the effect of the spherical and the chromatic aberration are both depending on the distance of the particle to the solenoid axis (see Equation 4.31), they cannot really be considered independently of each other. Nevertheless, in order to characterize both aberrations as well as possible, a monochromatic proton beam with 8.3 MeV and a proton beam with an energy range of (7 - 9) MeV will be transported by the first solenoid and the emittances of the resulting bunches are then compared with each other. Moreover, this is done for different maximum initial divergence angles in each case, so a_1 and a_2 are set to zero and $a_0 = \theta_{\text{max}}$ (see Section 2.3). Therefore, in the following θ_0 is also a direct measure for the distance of the particle to the nominal axis r_0 in and shortly after the first solenoid. The resulting effective, normalized emittances $\varepsilon^{2\sigma}_{n,xx'}$ of the proton beams just behind the RF cavity (2.5 m behind the origin) are shown in Table 4.2. Thereby, the same beamline setup as in the previous subsection is used (see Fig. 4.6) and the RF cavity is only implemented as a drift tube with an aperture of 35 mm.

Table 4.2: Emittances $\varepsilon^{2\sigma}_{n,xx'}$ of proton beams with different energies E and different maximum initial divergence angles a_0 that were collimated by the first solenoid of the LIGHT beamline. All other initial beam parameters are identical ($N = 3 \times 10^5$, $k_\mathrm{B}T = 6$ MeV, $E_\mathrm{cut} = 28$ MeV and $a_2 = a_1 = 0$). The emittances are determined just behind the RF cavity 2.5 m from the origin of the beamline.

a_0	$\varepsilon^{2\sigma}_{n,xx'}$
2°	0.11 mm mrad
4°	0.51 mm mrad
6°	1.73 mm mrad
8°	3.95 mm mrad

(a) E = 8.3 MeV

a_0	$\varepsilon^{2\sigma}_{n,xx'}$
2°	1.66 mm mrad
4°	6.45 mm mrad
6°	10.73 mm mrad
8°	12.84 mm mrad

(b) E = (7 - 9) MeV

The emittance of the monoenergetic proton beam is thus fifteen times ($a_0 = 2°$) or three times ($a_0 = 8°$) smaller than the emittance of the proton beam with an energy spread. Moreover, the emittance growth for the proton beams with energy spread scales approximately linearly with a_0, while for the monochromatic beams it scales approximately with a_0^3. Since the initial divergence of the particle is directly related to its distance to the nominal axis in and just behind the solenoid, the emittance growth in these simulations scales similar as the focal spot size in Equation 4.31.
The effect of the aberrations shall now also be discussed on the basis of Fig. 4.10.

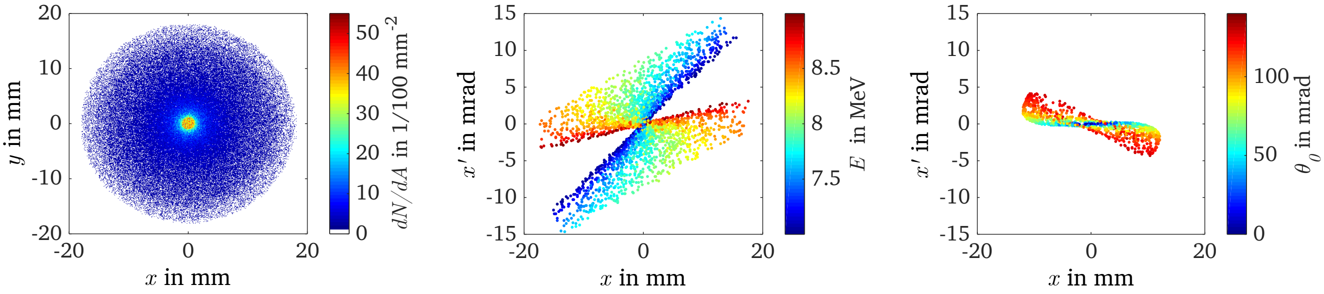

(a) $E = (7\text{-}9)$ MeV (b) $E = (7\text{-}9)$ MeV (c) $E = 8.3$ MeV

Fig. 4.10: Transported proton beams with different energies at the center of the LIGHT beamline. The current supplied to the capturing solenoid was 8.5 kA in these simulations.

The beam profile of the transported proton beam with an energy of $E = (7\text{-}9)\,\mathrm{MeV}$ (see Fig. 4.10a) is radially symmetric as the initial proton beam and the magnetic field distribution. In Fig. 4.10b the same proton beam is shown in the x-x' phase space. Thereby, the color of the particles corresponds to their energy. In this figure, the dependency of the focal length on the energy of the protons can be observed by the different orientation of the various energies in the x-x' phase space. For an energy of approximately 8.3 MeV

the beam is collimated best, whereas for lower and higher energies, the divergence of the beam increases. The energy for which most protons are collimated thus corresponds to the peak energy ($E_{\text{peak}} \approx 8.3\,\text{MeV}$) of the beam (see Fig 4.8).
In Fig. 4.10c the particles with an energy of 8.3 MeV are shown in the x-x' phase space. Thereby, the color of the particles correspond to their initial divergence angle θ_0 to better illustrate the spherical aberration. It can be seen that the particles with a larger initial divergence are rotated more clockwise in phase space and therefore had experienced a stronger focusing force by the solenoid. This is consistent with the findings in Section 4.2.

The results obtained so far should be taken with caution due to the highly simplified coil geometry that was used to generate the magnetic field distribution of the solenoid (see Section 4.3.1). A strong indication that the magnetic field is not perfectly radially symmetric in the experiments, is the filamentation of the beam profile in the x-y plane, which is typically observed in pulsed, high-field solenoid beamlines (see cover of this thesis or [Busold, 2014; Kroll, 2018; Brack et al., 2020]). Therefore, the influence of magnetic field imperfections on the beam profile and the beam quality are investigated in the following.

4.4.3. Cause of the beam filamentation in pulsed, high-field solenoid beamlines

The filamentation of the ion beam profile in pulsed, high field solenoid beamlines (see cover of this thesis or [Busold, 2014; Kroll, 2018; Brack et al., 2020]) has long been debated. In the following, the cause of the filamentation is investigated with simulations. These results have also been published in [Metternich et al., 2022].
From RIS data, it is known that the initial TNSA-generated ion beam is radially symmetric to a good approximation (see Section 2.2). Therefore, the beam filamentation has to be caused by an asymmetry in the magnetic field distribution of the solenoid, which in turn can only be caused by the connection cables or the slight inclination of the windings. To investigate this further, the magnetic field distribution of solenoid magnets with different coil geometries are calculated and for each of them the beam profile of the proton beam is simulated in the middle of the LIGHT beamline. The following coil geometries are used:

- Straight ring wires (Fig. 4.11a)
- Connected helix wires (Fig. 4.11b)
- Ring wires with connection cables (Fig. 4.11c)
- Realistic coil geometry (Fig. 4.12)

All four coils have 100 windings (4 x 25) and a total length of 150 mm. As described in Section 4.3.1, the corresponding field maps of the straight ring wires have been determined by reconstructing the coil geometry with many line wires and the Biot-Savart law. The corresponding field maps of the connected helix wires and the ring wires with connection cables are calculated in the same way. The realistic coil geometry was constructed in a Computer-Aided Design (CAD) software and the field maps were determined with the COMSOL Multiphysics® software.

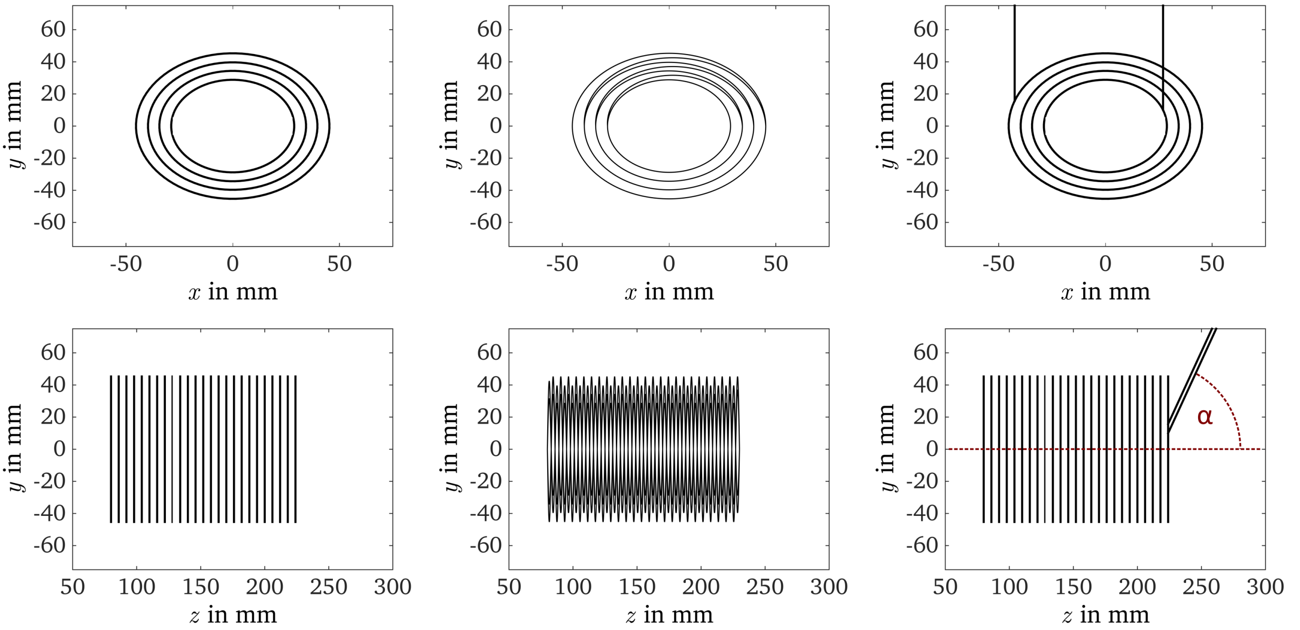

(a) Straight ring wires (b) Connected helix wires (c) Ring wires with connection cables

Fig. 4.11: Different coil geometries that have been used in this work to determine field maps of the magnetic field distribution with the Biot-Savart law.

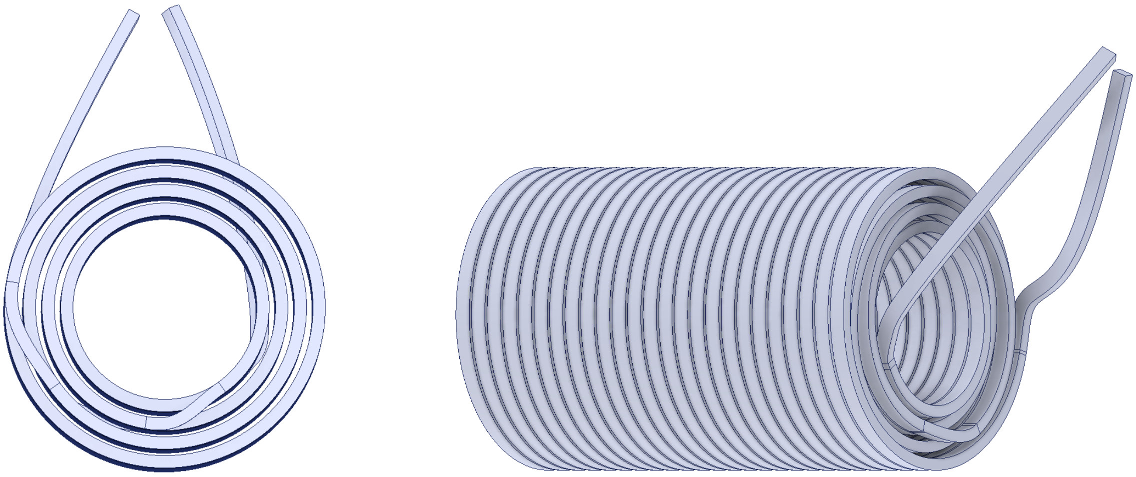

Fig. 4.12: Coil geometry of a solenoid magnet, which was constructed in a Computer-Aided Design (CAD) software.

The beam profiles of the captured protons are shown in Fig. 4.13. For these simulations the parameters shown in Table 4.1 have been used for the generation of the initial proton beam and the current supplied to the solenoid was 8.5 kA as in the previous subsection.

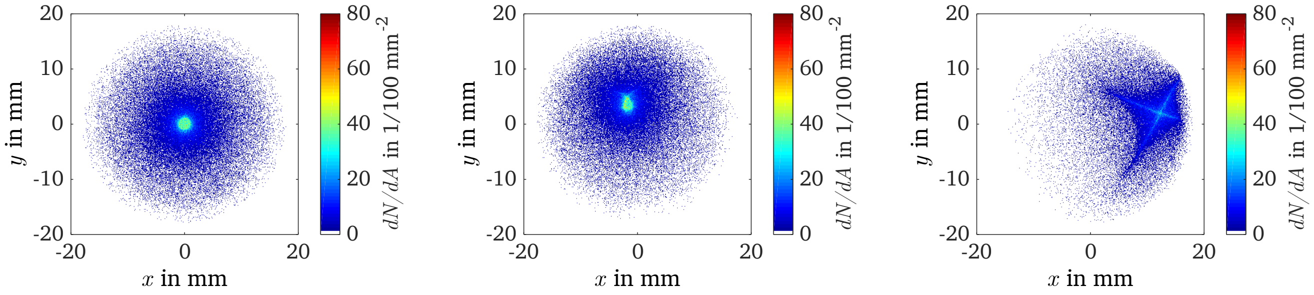

(a) Straight ring wires

(b) Connected helix wires

(c) Realistic coil

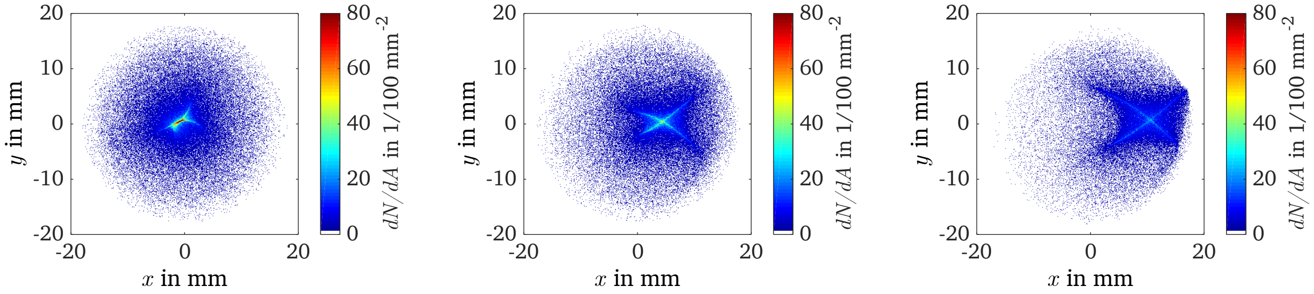

(d) Straight ring wires with connection cables (α = 90°)

(e) Straight ring wires with connection cables (α = 75°)

(f) Straight ring wires with connection cables (α = 60°)

Fig. 4.13: Beam profiles of the transported protons at the middle of the LIGHT beamline (2.5 m from their origin). Thereby, different field maps have been used for the capturing solenoid magnet in the simulation. These field maps were determined with the coil geometries shown in Fig.4.11 and 4.12.

The beam profile shown in Fig. 4.13a is radially symmetric to the z-axis which has to be the case since the initial beam as well as the wire geometry have this symmetry. In case of the connected helix wires this symmetry remains for the most part and therefore the corresponding magnetic field only causes a slight deflection of the beam. But by adding the magnetic field generated by the connection cables, this symmetry is harmed. In the case that the cables are directed as in Fig. 4.11c (towards the z- and y-direction) the generated magnetic field is also mainly directed towards this direction and its strength decreases with increasing distance to the cables. This has two effects:

- An astigmatism arises which causes the filamentation of the proton bunch.
- The proton bunch is directed towards the x-direction (in the case the connection cables are directed as in Fig. 4.11c).

Whether the magnetic field generated by the connecting cables is directed more towards the z- or y-direction depends on how the cables are routed away from the coil. It is mainly directed in the y-direction when the cables are parallel, and mainly directed in the z-direction when they are perpendicular to the coil (see Fig. 4.14). Since in particular the magnetic field in the y-direction adds an asymmetry to the magnetic field distribution, the influence of the connecting cables increases for smaller angles α (see Fig. 4.13).

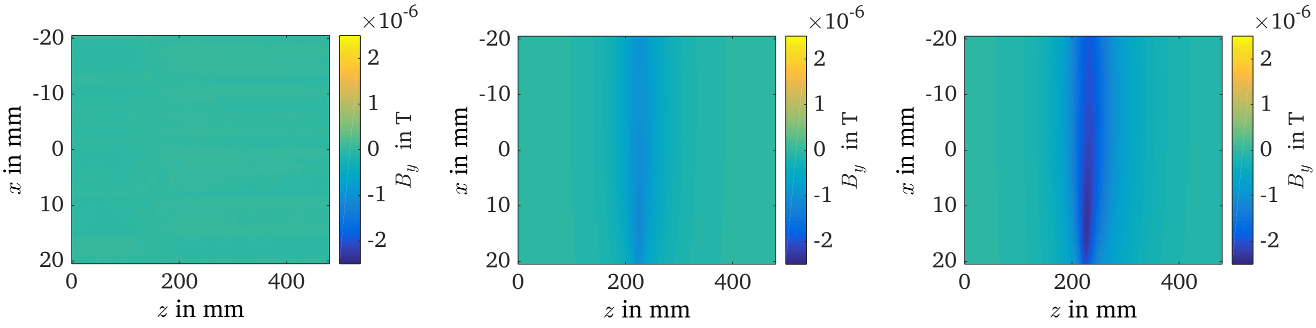

Ring wires w/o CC

Ring wires w/ CC ($\alpha = 75°$)

Ring wires w/ CC ($\alpha = 60°$)

Fig. 4.14: B_y field maps in the x-z-plane $(y = 0)$, which were determined with different coil geometries. The CC in the captions of the subfigures stands for connection cables and α indicates the angle between the connection cables and the x-z-plane (see in Fig. 4.11c).

In a future design of the solenoid magnet the following approaches could therefore be pursued to minimize the influence of the connecting cables:

- The connecting cables could be guided vertically away from the coil to minimize the y-component of their magnetic field.
- The connection cables could be guided close to each other, possibly even twisted together. Thereby, the magnetic fields of the two connecting cables would cancel each other out.
- The number of windings could be increased to decrease the relative magnetic field strength of the connecting cables in relation to the coil.
- The distance of the connecting cables to the drift tube of the solenoid could be increased by adding additional layers with windings or by increasing the radii of the layers.

In the next step, the influence of astigmatism on beam quality is now also determined. In Table 4.3 the effective, normalized emittances $\varepsilon^{2\sigma}_{n,xx'}$ of different beams, captured by the different field maps, are listed. Thereby in each case, the appropriate magnetic field strength is used to collimate protons with 8.3 MeV and the deflection of the beams by the magnetic field of the connection cables is compensated by a transverse displacement of the solenoid, so that the center of the cross-shaped beam profile is on the nominal trajectory as in Fig. 4.15d. As can be seen, for high initial divergence angles $(a_0 = 8°)$ the relative emittance growth that is caused by the connection cables and the inclination of the windings is less than 10 %. This indicates that mainly the particles that are close to the solenoid axis (particles with small initial divergence angles θ_0) are affected by the asymmetry of the magnetic field distribution of the realistic coil. This can also be seen in Fig. 4.15, where the transported beams obtained with the simplified and the realistic magnetic field distribution are compared.

Even though the imperfections in the magnetic field distributions only contribute slightly to the emittance growth, the energy distribution in the resulting filaments deviate from the energy distribution of the entire beam. The experimental campaign and the simulations in which this was revealed will be presented together in Chapter 7.

In the following chapter, the longitudinal beam shaping with the RF cavity will be explained first, since this will be essential for all the following investigations of this thesis.

Table 4.3: Emittances $\varepsilon^{2\sigma}_{n,xx'}$ of captured proton beams with different energies E and different maximum initial divergence angles a_0 just behind the RF cavity 2.5 m from their origin. Thereby, different field maps have been used for the first solenoid in the simulations. All other initial beam parameters are identical ($N = 3 \times 10^5$, $k_B T = 6$ MeV, $E_{\text{cut}} = 28$ MeV and $a_2 = a_1 = 0$) and CC is an abbreviation for ring wires with connection cables.

Fieldmap	$\varepsilon^{2\sigma}_{n,xx'}$
Ring wires	0.11 mm mrad
Helix wires	0.14 mm mrad
CC ($\alpha = 60°$)	0.61 mm mrad
Realistic coil	0.35 mm mrad

E = 8.3 MeV, a_0 = 2°

Fieldmap	$\varepsilon^{2\sigma}_{n,xx'}$
Ring wires	12.84 mm mrad
Helix wires	13.14 mm mrad
CC ($\alpha = 60°$)	13.90 mm mrad
Realistic coil	13.30 mm mrad

E = (7 - 9) MeV, a_0 = 8°

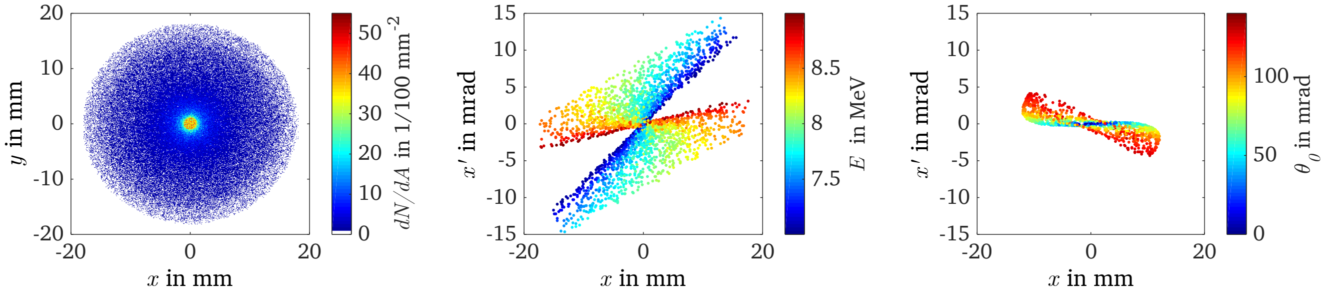

Ring wires, $E = (7\text{-}9)$ MeV Ring wires, $E = (7\text{-}9)$ MeV Ring wires, $E = 8.3$ MeV

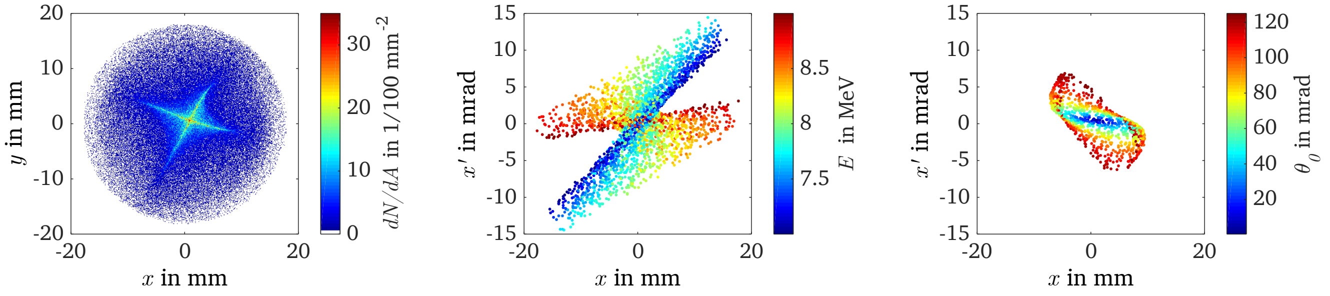

Realistic coil, $E = (7\text{-}9)$ MeV Realistic coil, $E = (7\text{-}9)$ MeV Realistic coil, $E = 8.3$ MeV

Fig. 4.15: Comparison of transported proton beams that have been captured by solenoid magnets with different magnetic field distributions in the simulation. The proton beams are shown in the middle of the LIGHT beamline (2.5 m from their origin) and the magnetic field distributions have been determined with the coil geometries shown in Fig. 4.11 and 4.12.

5. Longitudinal beam shaping with an RF cavity

In this chapter, the longitudinal beam shaping with an RF cavity is considered. Therefore, the main tasks of the RF cavity at the LIGHT beamline are presented first. Then the technical design of the RF cavity used in this thesis and the velocity dependent energy transfer that results from this design is discussed. Thereby, equations are derived that can be used to determine the required RF cavity voltage for different applications and different setups of the LIGHT beamline. Finally, the implementation of the RF cavity in the numerical simulations is explained, which is then used in the following chapters to make predictions about the beam parameters that can be achieved with the LIGHT beamline.

5.1. Longitudinal beam shaping fundamentals

In a beamline with only beam guiding magnets, a beam with a momentum deviation expands longitudinally. For a free propagation over the distance L_d the following applies for a single particle with a momentum deviation δ and an initial longitudinal deviation of $l_0 = 0$:

$$\delta = \text{const.}, \quad l = \frac{\delta}{\gamma^2} L_d. \tag{5.1}$$

As already stated in Section 3.1 in the context of this work the kinetic energy E and the time of flight t of the particles are specified most of the time which are related to δ and l as follows:

$$E = \text{const.}, \quad \Delta t = t - t_0 = \frac{l}{v_0}. \tag{5.2}$$

By inserting Equation 5.1 in Equation 5.2 and using the relation $\delta = \Delta p/p = \beta^{-2}\Delta\tilde{E}/\tilde{E}$ [Wille, 1996] one obtains

$$\Delta t = \frac{\Delta\tilde{E}}{\tilde{E}} \frac{L_d}{\gamma^2\beta^3 c}. \tag{5.3}$$

Thereby $\tilde{E}$ is the total energy of the particle $\tilde{E} = E + m_0c^2$. This equation can also be used to determine the change in temporal width Δt of an ion bunch, provided that the mean energy $\tilde{E}$, the energy spread $\Delta\tilde{E}/\tilde{E}$ and the distance L_d are known. However, it should be noted that this relation has been derived in the context of linear beam dynamics and therefore deviations may occur if $\Delta\tilde{E} \ll \tilde{E}$ does not apply.

In accelerators, as in this thesis, high-frequency (RF) electric fields generated in cavities are used to accelerate particles and thus influence the longitudinal beam dynamics. Let ω be the frequency of the electric field in the RF cavity and U_0 the maximum voltage. Then in case of a short interaction between the electric field of the cavity and the particle $(v/L_{\text{cav}} \ll 2\pi/\omega)$, the energy transfer to the particle is given by

$$\Delta E = q \cdot U_0 \cdot \cos(\omega \cdot \Delta t + \phi). \tag{5.4}$$

Thus, the nominal particle $(\Delta t = 0)$ experiences a maximum acceleration for $\phi = 2\pi \cdot n$, a maximum deceleration for $\phi = \pi(2n \pm 1)$ and is unaffected by the cavity for $\phi = \pi(2n \pm 0.5)$. In the context of this

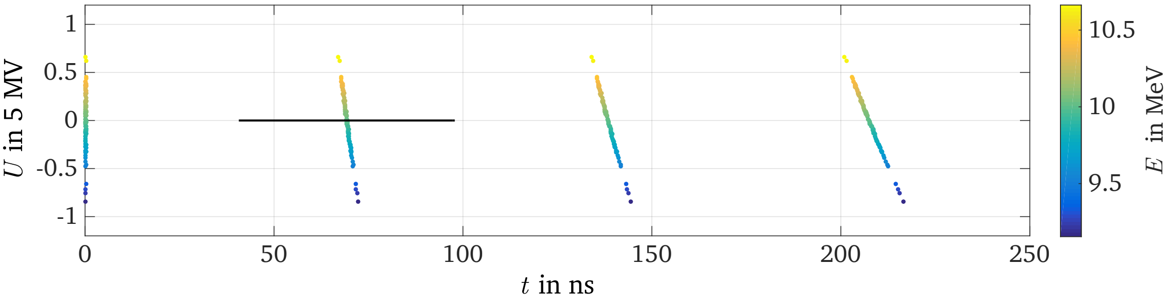

(a) Free beam propagation

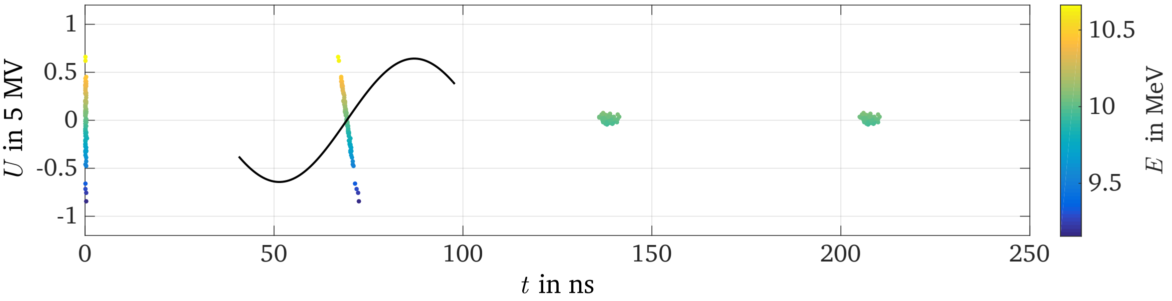

(b) Energetic compression

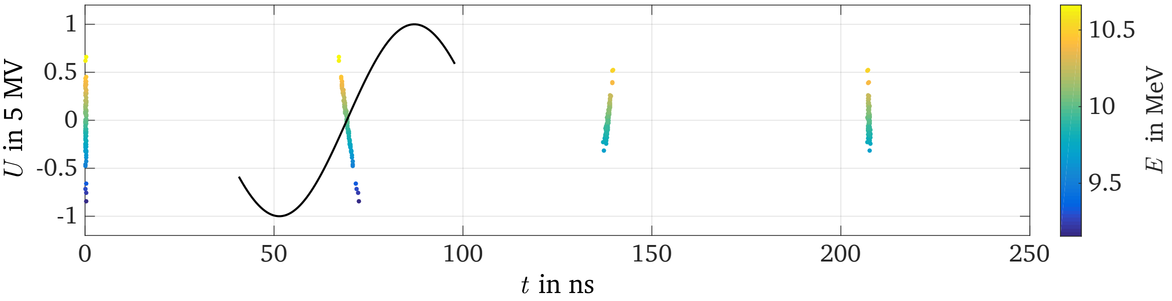

(c) Temporal compression

Fig. 5.1: Temporal evolution of an ion beam in case of a free propagation (Fig. 5.1a), an energetic compression (Fig. 5.1b) and a temporal compression (Fig. 5.1a). The energy transfer to the beam is indicated by the black line and the color of the ions corresponds to their energy.

thesis, the case $\phi = \pi(2n - 0.5)$ is particularly interesting, since thereby an energetic compression or even a temporal compression of the ion bunch can be achieved. This is now described with the help of Fig. 5.1. The black line in these images represents the electric field of an RF cavity and the colored dots are the particles of a beam in the E-t-phase space for different times. Thereby, the color of the particles correspond to their energy. Without any electric field, the temporal width of the beam increases due to the energy spread of the beam (Fig. 5.1a). As can be seen, during the free propagation the linear correlation between the energy and the time of flight of the particles remains (according to Equation 5.4). If the temporal width of the bunch in the RF cavity is small so that $\cos(\omega \cdot \Delta t + \phi) \approx \omega \cdot \Delta t + \phi$ is a valid assumption, the energy transfer of the RF cavity to the particles is also proportional to their time of flight for $\phi = \pi(2n - 0.5)$ (see Equation 5.4). Therefore, the energy spread of the bunch can be minimized for the proper electric field strength of the RF cavity (see Fig. 5.1a). This method is called energetic compression in the following and the corresponding electric field strength will be U_{Ecomp}. For an RF cavity voltage higher than U_{Ecomp} the resulting energy distribution causes the bunch to contract in time during the subsequent drift until it reaches a minimum temporal width (see Fig. 5.1c). This temporal compression of the bunch is the main operation mode of the RF cavity in the experimental campaigns of this thesis, since it leads to high particle fluxes.

In the following equations shall be derived that can be used to determine the required RF cavity voltage for the energetic and the temporal compression at the LIGHT beamline. Thereby, the RF cavity used in this work is characterized precisely.

5.2. Design and effective voltage of the three-gap spiral resonator

At the LIGHT beamline a three-gap spiral resonator, which was formerly used at the UNILAC of GSI [Häuser, 1989], is implemented. A schematic overview of this RF cavity is shown in Fig. 5.2a and the corresponding values of the distances that are drawn in as well as the most important electric properties are given in Table 5.1.

Table 5.1: Most important geometrical and electric data of the three gap spiral resonator used in this thesis.

Geometrical data

Aperture a	35 mm
Outer gap length $L_{\mathrm{gap,o}}$	20 mm
Inner gap length $L_{\mathrm{gap,i}}$	40 mm
Drift tube length $L_{\mathrm{drift,o}}$	85 mm
Drift tube length $L_{\mathrm{drift,i}}$	150 mm
Gap to gap length L_{gg}	180 mm

Electric data

Resonance frequency f_{RF}	108.4 MHz
Optimal particle velocity v_{opt}	$8\,\mathrm{MeV\,u^{-1}}$
Shunt impedance R_s	$21.8\,\mathrm{M\Omega\,m^{-1}}$
Maximum RF power P_{RF}	> 100 kW
Maximum RF cavity voltage U_{max}	~ 1 MV
Quality factor Q	> 6000

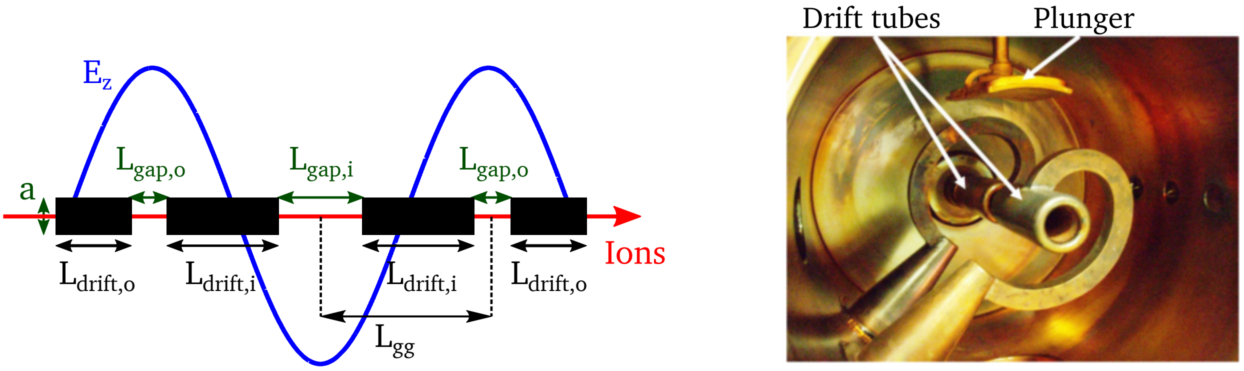

(a) Schematic overview of the three gap spiral resonator

(b) Photograph of the inside of the three gap spiral resonator

Fig. 5.2: Schematic overview and photograph of the inside of the three gap spiral resonator used in this thesis [Busold, 2014; Ding, 2018].

The three-gap geometry causes an energy transfer which depends on the ion velocity v. Moreover, for ions with low velocities the electric field cannot be assumed to be constant during the time in which they pass the gap, so the assumption $v/\mathrm{L}_{\mathrm{gap,i}} \gg \omega = 2\pi f_{\mathrm{RF}}$ is not given. Since in this work also particles with relatively low velocities are temporally compressed, the dependency between the energy transfer of the RF cavity and the ion velocity is derived now. The considerations in this section are mainly taken from [Ding, 2018].

For the following considerations it is always assumed, that the energy transfer of the cavity is much smaller than the initial energy of the particle $\Delta E_{\mathrm{RF}} \ll E_{\mathrm{particle}}$ as well as that the electric field in the gap is spatially constant and only directed towards the z-direction: $\mathbf{E}(r,t) = (0,0,E_z(t))$. Let's first also assume that $v/\mathrm{L}_{\mathrm{gap,i}} \gg \omega$ is given. Between the inner and the outer gaps there is a phase shift of π. Therefore, a particle with an energy per mass of $8\,\mathrm{MeV\,u^{-1}}$ experiences the same electric field strength in all three gaps, since the time required for this particle to travel from an outer to an inner gap corresponds to half the period duration

$$\frac{T}{2} = \frac{\mathrm{L}_{\mathrm{gg}}}{v_{\mathrm{opt,0}}}. \tag{5.5}$$

So $v_{\mathrm{opt,0}}$ corresponds to the velocity of a particle with an energy per mass of $8\,\mathrm{MeV\,u^{-1}}$ and L_{gg} is the distance from the inner to an outer gap (see Fig. 5.2a). According to this consideration, also particles with a velocity of

$$v_{\mathrm{opt},n} = \frac{v_{\mathrm{opt,0}}}{2n+1}, \tag{5.6}$$

with $n \in \mathbb{N}$, experiences the same electric field strength in all three gaps, whereas for the velocities

$$v_{\mathrm{unsuitable},n} = \frac{v_{\mathrm{opt,0}}}{2n} \tag{5.7}$$

the energy transfer of the outer gaps and the inner gap cancel each other out and therefore no energy transfer is possible. If the assumption $v/\mathrm{L}_{\mathrm{gap,i}} \gg \omega = 2\pi f_{\mathrm{RF}}$ is not valid, the energy transfer of a single gap to a particle is

$$\begin{aligned}
\Delta E_{\mathrm{RF}} &= q \int_{-\mathrm{L}_{\mathrm{gap}}/2}^{\mathrm{L}_{\mathrm{gap}}/2} E_z(t)\, dz. && (5.8)\\
&\approx q v E_{z,0} \int_{-t_{\mathrm{gap}}/2}^{t_{\mathrm{gap}}/2} \cos(\omega t + \phi)\, dt. && (5.9)\\
&= q v E_{z,0} \int_{-t_{\mathrm{gap}}/2}^{t_{\mathrm{gap}}/2} \left(\cos(\omega t)\cos(\phi) + \sin(\omega t)\sin(\phi)\right)\, dt && (5.10)\\
&= q v E_{z,0} \cos(\phi) \int_{-t_{\mathrm{gap}}/2}^{t_{\mathrm{gap}}/2} \cos(\omega t)\, dt && (5.11)\\
&= q v E_{z,0} \cos(\phi)\, \frac{2\sin\left(\omega t_{\mathrm{gap}}/2\right)}{\omega}. && (5.12)
\end{aligned}$$

Thereby $t_{\mathrm{gap}} = L_{\mathrm{gap}}/v$ since $\Delta E_{\mathrm{RF}} \ll E_{\mathrm{particle}}$ as mentioned in the beginning. Also, $U_0 = E_{z,0} L_{\mathrm{gap}}$ and therefore, it follows:

$$\begin{aligned}
\Delta E_{\mathrm{RF}} &= q U_0 \cos(\phi)\, \frac{2v}{\omega \mathrm{L}_{\mathrm{gap}}} \sin\left(\frac{\omega \mathrm{L}_{\mathrm{gap}}}{2v}\right) && (5.13)\\
&= q U_0 \cos(\phi_0)\, TT, && (5.14)
\end{aligned}$$

with the transit time factor TT of a gap. Now the effective voltage of the three gap spiral resonator used in this work is determined for the maximal acceleration of the nominal particle (ϕ = 0°):

$$U_{\text{eff}}^{\text{TT}} = \underbrace{U_0 TT_1 \cos(\pi - \omega \mathrm{L_{gg}}/v)}_{\text{gap,1}} + \underbrace{2U_0 TT_2 \cos(0)}_{\text{gap,2}} + \underbrace{U_0 TT_3 \cos(\pi + \omega \mathrm{L_{gg}}/v)}_{\text{gap,3}}, \tag{5.15}$$

with $U_{\text{cav}} = 4U_0 \to U_1 = U_0, U_2 = 2U_0, U_3 = U_0$ and the transit time factor of the nth gap TT_n. Since $TT_1 = TT_3$ and $\cos(-x+\pi) = \cos(x+\pi)$ Equation 5.15 can be simplified to

$$U_{\text{eff}}^{\text{TT}} = 2U_0 \left(TT_2 + TT_1 \cos(\pi + \omega \mathrm{L_{gg}}/v)\right). \tag{5.16}$$

This equation can only further be simplified for $v/\mathrm{L_{gap,i}} \gg \omega$. In this case $TT_n \approx 1$, which corresponds to the assumption made in the beginning of this section and thus

$$U_{\text{eff}} \approx 2U_0 \left(1 + \cos(\pi + \omega \mathrm{L_{gg}}/v)\right). \tag{5.17}$$

For a cavity voltage of $U_{\text{cav}} = 4U_0$ = 8 kV and the geometrical data shown in Table 5.1, the effective voltage is illustrated in Fig 5.3 for ions with different energies per mass.

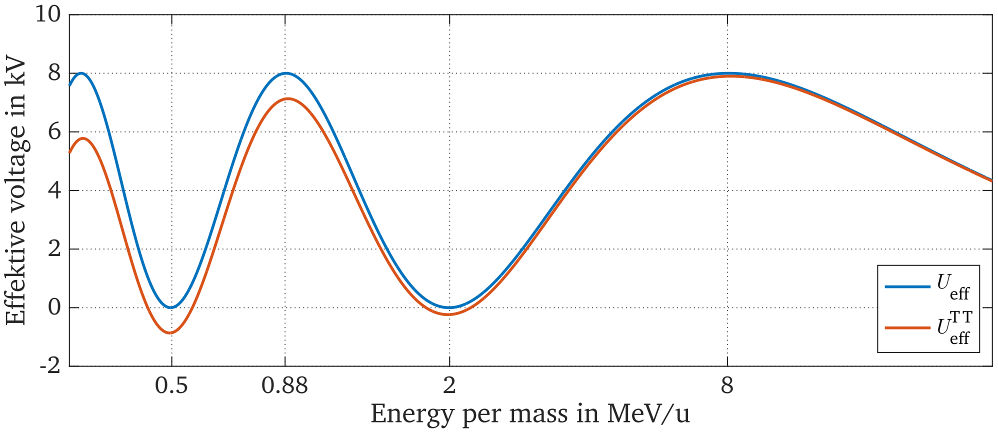

Fig. 5.3: Effective voltage of the three-gap spiral resonator used at the LIGHT beamline for ions with different energies per mass at a maximum outer gap voltage of 2 kV and a maximum inner gap voltage of 4 kV [Ding, 2018]. The blue line is calculated by Equation 5.17, so the transit time factor is $TT = 1$. For the determination of the red line Equation 5.16 is used, so the transit time factor TT is determined for each energy per mass and gap length.

With the effective RF cavity voltage, the required RF cavity voltage for the energetic and the temporal compression can be determined, which is explained in the next section.

5.3. Required RF cavity voltage for the energetic and the temporal compression

Let U_{Ecomp} be the required RF cavity voltage for the energetic compression, E the mean energy of the bunch, $\Delta E/E$ the energy spread of the bunch and $d_{\text{cav,1}}$ the distance of the RF cavity to the origin of the beam for the following considerations. Also, the temporal width of the bunch at its origin is assumed to be zero. In Section 5.1 the following relation for the temporal width of the beam is derived in terms of linear beam optics:

$$\Delta t = \frac{\Delta \tilde{E}}{\tilde{E}} \frac{d_{\mathrm{cav,1}}}{\gamma^2 \beta^3 c}, \tag{5.18}$$

with the total energy $\tilde{E} = E + m_0 c^2$. Therefore, the relation between the time and the energy deviation is linear in first approximation and the energetic compression is only possible in the range, in which the temporal change of the electric field is also approximately linear. This time is assumed to be $T_{\mathrm{linear}} \mathrel{\widehat{=}} T/6$ in the following to ensure that the deviation of $\omega \cdot T_{\mathrm{linear}}$ and $2\sin(\omega \cdot T_{\mathrm{linear}}/2)$ is less than 10 %. The relations of those variables is shown in Fig. 5.4.

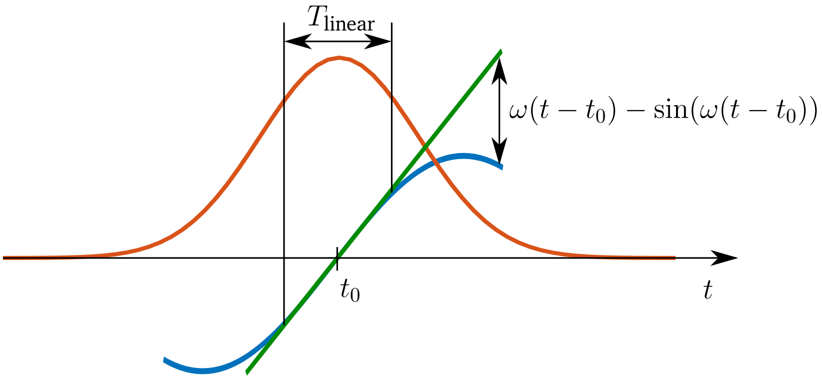

Fig. 5.4: Schematic Illustration of the parameter T_{linear}. Thereby, the red line corresponds to the temporal profile of the ion bunch in the RF cavity, the blue line corresponds to the energy transfer of the RF cavity and the green line corresponds to the energy transfer that is required for an energetic compression of the ion bunch. As can be seen, only in the time T_{linear} the deviation between $\omega(t-t_0)$ and $\sin(\omega(t-t_0))$ is very small and therefore only this part of the ion beam can be energetically compressed by the RF cavity.

At the LIGHT beamline the temporal width of the bunch within the cavity is usually longer than T_{linear} which is therefore always assumed in the following. The energy deviation $\Delta E_{\mathrm{linear}}$ of the bunch that can be energetically compressed is

$$\Delta E_{\mathrm{linear}} \approx \frac{\gamma^2 \beta^3 c T_{\mathrm{linear}}}{d_{\mathrm{cav,1}}} \tilde{E}. \tag{5.19}$$

For this reason, the distance of the RF cavity to the origin of the beamline $d_{\mathrm{cav,1}}$ should be as short as possible, since then the fraction of the beam that is energetically compressed becomes larger. On the other hand the required cavity voltage U_{Ecomp} increases for a lower distance $d_{\mathrm{cav,1}}$ since for an energetic compression the following condition must apply

$$\Delta E_{\mathrm{RF,\ Ecomp}} = q U_{eff}^{TT} = \frac{\Delta E_{\mathrm{linear}}}{2\sin(\omega T_{\mathrm{linear}}/2)} \approx \frac{\Delta E_{\mathrm{linear}}}{\omega T_{\mathrm{linear}}}, \tag{5.20}$$

with (see previous section):

$$U_{\mathrm{eff}}^{\mathrm{TT}} = \frac{U_{\mathrm{cav}}}{2} \left(TT_2 + TT_1 \cos(\pi + \omega \mathrm{L_{gg}}/v) \right). \tag{5.21}$$

Therefore, the required RF cavity voltage for the energetic compression is

$$U_{\mathrm{Ecomp}} = \frac{2 \Delta E_{\mathrm{linear}}}{q \omega T_{\mathrm{linear}} C_{\mathrm{TT}}(v)} \tag{5.22}$$

with

$$C_{\mathrm{TT}}(v) = TT_2(v) + TT_1(v)\cos(\pi + \omega \mathrm{L_{gg}}/v). \tag{5.23}$$

Substituting Equation 5.19 in Equation 5.22 results in the following relation between the voltage U_{Ecomp}, the distance $d_{\mathrm{cav,1}}$ and the mean energy E of the bunch:

$$d_{\mathrm{cav,1}} \cdot U_{\mathrm{Ecomp}} = \frac{2\gamma^2\beta^2 c(E + m_0c^2)}{q\omega C_{\mathrm{TT}}(v)}. \tag{5.24}$$

This equation is now used to determine the voltage U_{Ecomp} and the distance $d_{\mathrm{cav,1}}$ for different mean proton bunch energies E. The maximum voltage U_{max} of the RF cavity at the LIGHT beamline is 1 MV and the distance $d_{\mathrm{cav,1}}$ can be adjusted between (1225 - 2275) mm. In the left image of Fig. 5.5 the required distance $d_{\mathrm{cav,1}}$ for an energetic compression of a bunch with a mean energy E is shown for the maximum RF cavity voltage U_{max} and in the right image of Fig. 5.5 the required RF cavity voltage U_{Ecomp} is illustrated for the upper and lower limit of $d_{\mathrm{cav,1}}$. For some energies $d_{\mathrm{cav,1}}$ and U_{Ecomp} approaches infinity since the parameter $C_{\mathrm{TT}}(v)$ approaches zero for these energies (zero crossings of the red line in Fig. 5.3).

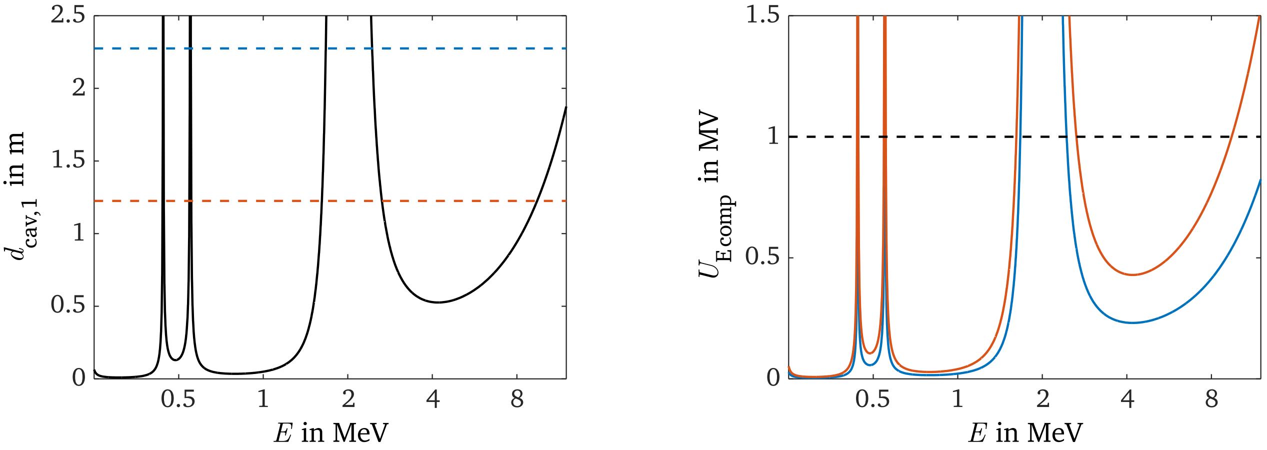

Fig. 5.5: In the left picture, the required distance $d_{\mathrm{cav,1}}$ (black line) for an energetic compression is shown for different mean energies E of the bunch and the maximum RF cavity voltage of $U_{\mathrm{max}} = 1\,\mathrm{MV}$. The upper (blue dashed line) and the lower (red dashed line) limit of $d_{\mathrm{cav,1}}$ at the LIGHT beamline are also drawn in. In the right picture, the required RF cavity voltage for the energetic compression is plotted for the upper (blue line) and the lower (red line) limit of $d_{\mathrm{cav,1}}$. For these illustrations, Equation 5.24 is used and the x axes are scaled logarithmically.

As can be seen, Equation 5.24 can be used to determine the required voltage U_{Ecomp} at the LIGHT beamline for each ion type and energy. Since the principle of the temporal compression is very similar to the principle of the energetic compression, the required voltage for the temporal compression U_{tcomp} can also be determined by Equation 5.24 which is explained in the following.

To obtain a temporal compression instead of an energetic compression, the RF cavity voltage has to be increased. The resulting energy distribution then causes the bunch to contract in time behind the RF cavity. Since the change of the temporal bunch width is proportional to the energy spread and the distance (see Equation 5.18), the required RF cavity voltage for the temporal compression U_{tcomp} depends on the distance $d_{\mathrm{cav,2}}$ from the RF cavity to the position, at which the bunch should have its minimum temporal length. As in the case of the energetic compression, only the fraction of the beam, that has a temporal width of approximately $T/6$ within the RF cavity can be temporally compressed. Therefore,

$$U_{\text{tcomp}} = (1 + d_{\text{cav,1}}/d_{\text{cav,2}}) \cdot U_{\text{Ecomp}} \tag{5.25}$$

and in this case the energy spread of the temporally compressed beam is given by

$$\frac{\Delta E_{\text{tcomp}}}{E} = \frac{\Delta E_{\text{linear}}}{E} \cdot \frac{d_{\text{cav,1}}}{d_{\text{cav,2}}}. \tag{5.26}$$

The most important concepts of this work with respect to the longitudinal ion beam shaping have thus been covered. Since the TNSA-generated proton beam at Z6 can be characterized very precisely and the RF cavity is best suited for an energy per mass of 8 MeV u^{-1}, in the first experiments with the LIGHT beamline proton beams with approximately 8 MeV were exclusively targeted. These were, also in the context of this work (see Chapter 7), successfully transported, energetically compressed, temporally compressed and focused [Busold et al., 2013, 2014b, 2015; Jahn et al., 2019; Metternich et al., 2022]. In order to make predictions on the beam parameters that can be achieved for other ion species and energies, the RF cavity has been implemented in the numerical simulations, which is now explained in the last section of this chapter.

5.4. Implementation of the RF cavity in the numerical simulations

In the simulation, the RF cavity only consists of the three gaps whose length and spacing are as shown in Fig 5.2a. For the electric field **E**, the following assumptions are made:

- The electric field is only directed towards the z-direction: $\mathbf{E} = (0, 0, E_z)$.
- The electric field is spatially constant in the gap.
- Outside the gaps, the electric field immediately drops to zero.

That these assumptions are justified is shown in Appendix A.2. In the gaps, the electric field acting on a particle is therefore

$$\begin{aligned} E_{z,\text{gap1}} &= E_{z,0} \cdot \cos(\omega \cdot t + \phi) \\ E_{z,\text{gap2}} &= E_{z,0} \cdot \cos(\omega \cdot t + \phi + \pi) \\ E_{z,\text{gap3}} &= E_{z,0} \cdot \cos(\omega \cdot t + \phi) \end{aligned} \tag{5.27}$$

with the time of flight of the particle t, the electric field strength $E_{z,0}$ and the phase ϕ. The latter two can be adjusted as desired in the simulation. Instead of the electric field strength $E_{z,0}$, the cavity voltage U_{cav} is usually given in the following, which is in accordance to the considerations in the previous sections of this chapter defined as follows:

$$U_{\text{cav}} = E_{z,0} \cdot (2L_{\text{gap,o}} + L_{\text{gap,i}}). \tag{5.28}$$

As a validation, the energy transfer to a collimated proton beam with an energy range of $E = (0.1 \text{ - } 10)\,\mathrm{MeV}$ for a cavity voltage of $U_{\text{cav}} = 8\,\mathrm{kV}$, a distance of the cavity to the beams' origin of $d_{\text{cav,1}} = 2275\,\mathrm{mm}$ and different phases ϕ is shown in Fig. 5.6, which is consistent with the determined energy transfer of the RF cavity shown in Fig. 5.3.

With the implementation of the RF cavity, it is now possible to simulate the ion beam shaping with the LIGHT beamline for specific applications. This will now be done in the next part of this thesis to make predictions about the achievable beam parameters and compare them with experimental results.

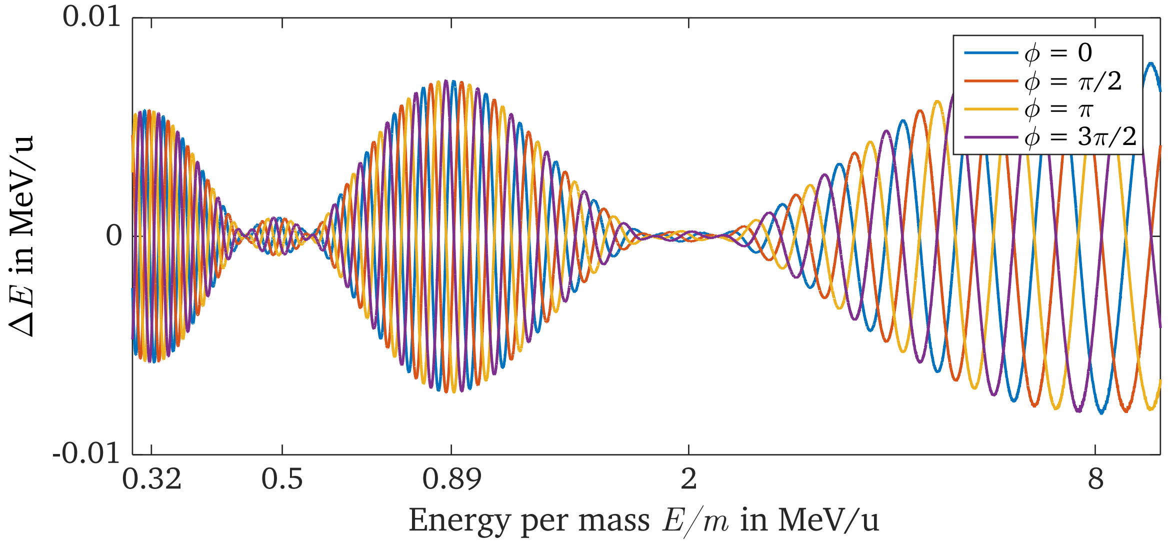

Fig. 5.6: Simulated energy transfer to a collimated proton beam with an energy E of (0.1 - 10) MeV for a cavity voltage of U_{cav} of 8 kV, a distance of the cavity to the beams' origin $d_{\mathrm{cav},1}$ of 2275 mm and different phases ϕ. The x-axis is logarithmic in this figure.

Part II.

Investigations on specific applications

6. SIS18 injection with the LIGHT beamline

The first application that will be investigated is the generation of an ion beam with the LIGHT beamline that can be injected into the heavy ion synchrotron SIS18 of GSI. Therefore, in the beginning of this chapter an introduction to this project is given and the beam parameter requirements are defined. After that, the setup for the LIGHT beamline is considered for two different mean proton beam energies. The resulting setups are then used in simulations to determine the resulting beam parameters and estimate the amount of particles that can be injected into the SIS18.

6.1. Required beam parameters for the SIS18 injection

Injecting a laser-generated ion beam into a synchrotron would be a major milestone for the laser plasma accelerator community. In this section, a closer look at how close the implementation of a first proof of principle experiment at GSI is and which preparations still have to be made. In Fig. 6.1, a schematic overview of the accelerator facility at GSI is illustrated.

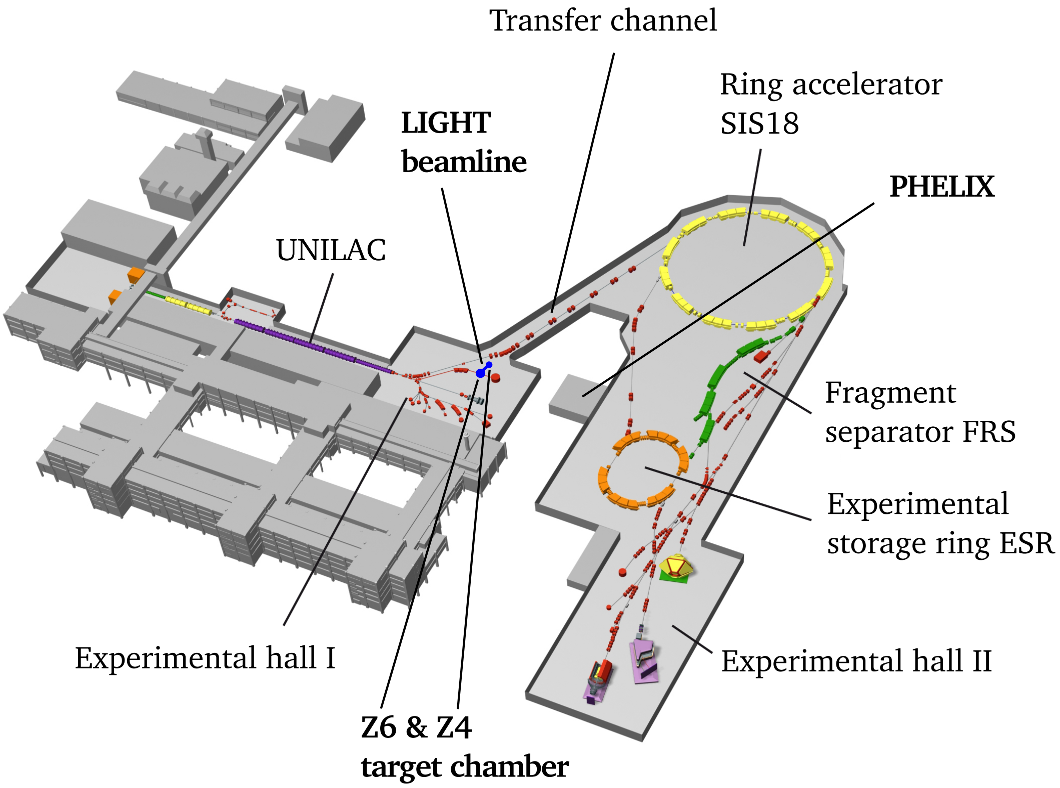

Fig. 6.1: Schematic drawing of the accelerator facility at GSI.

The UNILAC can accelerate almost all ion species to 11.4 MeV u^{-1}. These can then either be used at the experimental areas of the experimental hall I, or they are injected into the heavy ion synchrotron SIS18 via the transfer channel for post acceleration. As can be seen in Fig. 6.1, the LIGHT beamline is right next to the transfer channel and protons with 11.4 MeV u^{-1} are also well within the capabilities of the LIGHT beamline. The initial conditions for a first proof-of-principle experiment are therefore very promising.
However, it remains to be determined whether the LIGHT beamline can generate a proton beam which is within the acceptance range of the SIS18 and whether it contains a sufficient number of protons to be detected by the respective beam diagnostic. The following values are specified for the acceptance of the SIS18 [GSI, 2022]:

- Normalized horizontal emittance $\varepsilon^{2\sigma}_{n,xx'} = 3.12\,\mathrm{mm\,mrad}$
- Normalized vertical emittance $\varepsilon^{2\sigma}_{n,xx'} = 9.96\,\mathrm{mm\,mrad}$
- Energy spread $\Delta E/E = \pm 0.2\,\%$ (full width)

It is also known that the maximum number of protons reached in SIS18 is about 3×10^{10} and the time the UNILAC needs to fill the SIS18 is approximately 130 µs [GSI, 2022].
The extent to which the required beam parameters for the SIS18 injection can be accomplished with the LIGHT beamline will be determined with simulations in the following. Therefore, the setup of the LIGHT beamline is considered first.

6.2. Setup of the LIGHT beamline for the SIS18 injection

For a first proof of principle experiment, protons will be used since they are accelerated most efficiently by the TNSA mechanism and therefore most particles are expected for this ion species. Since the RF cavity at the LIGHT beamline is best suited for a proton energy of 8 MeV and the proton beam energy that the UNILAC usually provides to the SIS18 is 11.4 MeV, these two energies are used for the following considerations.
In Chapter 4 it was shown that the energy spread of the transported ion beam at the LIGHT beamline is $\Delta E/E = 10\,\%$ (FWHM) as well as that the emittance of a transported proton beam with a mean energy of 8.3 MeV and a maximal initial divergence angle of 8° is $\varepsilon^{2\sigma}_{n,yy'} \approx \varepsilon^{2\sigma}_{n,xx'} = 13.3\,\mathrm{mm\,mrad}$. Thus, the transverse emittance of the transported beam is expected to be approximately in the order of the acceptance range of the SIS18, while its energy spread will be much larger than required. The extent to which the injection is possible therefore depends mainly on the amount of particles that can be energetically compressed by the RF cavity. Therefore, as a first step, the energy spread of the transported proton beam that can be energetically compressed $\Delta E_{\mathrm{linear}}/E$ and the RF cavity voltage U_{Ecomp} required for that are determined with Equation 5.24. The results are shown in the Tables 6.1a and 6.1b for different distances $d_{\mathrm{cav},1}$ that are geometrically accessible at the LIGHT beamline.
The maximum RF cavity voltage is $U_{\max} \approx 1\,\mathrm{MV}$, which means that the energetic compression for protons with 8 MeV and a distance $d_{\mathrm{cav},1}$ of 1225 mm is within the capabilities of the RF cavity, whereas for protons with 11.4 MeV it is just about possible for a distance $d_{\mathrm{cav},1}$ of 1750 mm. The simulations of these two scenarios are now presented. Thereby, in both cases the second solenoid is not implemented since the resulting beam is already considered after the RF cavity and for the first solenoid the field maps determined with the realistic coil are used (see Section 4.4.3).

Table 6.1: The energy spread $\Delta E_{\text{linear}}/E$ of the transported beam that can be energetically compressed by the RF cavity of the LIGHT beamline as well as the required voltage U_{Ecomp} for different distances $d_{\text{cav,1}}$. The values are determined with Equation 5.19 and 5.22 for protons with a desired energy of 8 MeV (Table 6.1a) and 11.4 MeV (Table 6.1b).

$d_{\text{cav,1}}$	$\Delta E_{\text{linear}}/E$	U_{Ecomp}
1225 mm	9.84 %	0.77 MV
1750 mm	6.89 %	0.54 MV
2275 mm	5.30 %	0.41 MV

(a) E = 8 MeV

$d_{\text{cav,1}}$	$\Delta E_{\text{linear}}/E$	U_{Ecomp}
1225 mm	11.74 %	1.39 MV
1750 mm	8.22 %	0.97 MV
2275 mm	6.32 %	0.75 MV

(b) E = 11.4 MeV

6.3. Simulations on the energetic compression of protons with 8 MeV

The simulations of the energetic compression of protons with 8 MeV will be presented first. Therefore, the capturing solenoid is supplied with 8.3 kA so that protons with 8 MeV are collimated. The distance $d_{\text{cav,1}}$ is set to the smallest distance possible (1225 mm) since according to Table 6.1a this leads to the largest value of $\Delta E_{\text{linear}}/E$ and U_{Ecomp} is still well within the capabilities of the RF cavity. For the initial proton beam parameters shown in Table 6.2 the smallest energy spread of the beam behind the RF cavity was achieved for an RF cavity voltage of 0.78 MV in the numerical simulations, which is thus consistent with the analytically determined values in Table 6.1a.

Table 6.2: Parameters that were used to generate the beam for the simulation of the energetic compression in case of protons with 8 MeV.

N	$k_B T$	E_{min}	E_{max}	E_{cut}	a_2	a_1	a_0	m	q
1×10^7	6 MeV	6 MeV	10 MeV	28 MeV	-0.04 °/MeV^2	0.41 °/MeV	26.47 °	1 u	1 e

The spectra of the initial, the transported, and the energetically compressed proton beam obtained in this way are shown in the left image of Fig. 6.2. The most important parameters of the particles that pass the RF cavity are as follows:

- Energy spread $\Delta E/E = 0.32\,\%$ (FWHM)
- Horizontal emittance $\varepsilon^{2\sigma}_{n,xx'} = 17.4$ mm mrad (entire beam)
- Vertical emittance $\varepsilon^{2\sigma}_{n,yy'} = 17.3$ mm mrad (entire beam)
- Number of protons $N_{\text{sim}} = 3.7 \times 10^5$ (entire beam)

The energy spread of the transported proton beam is 10 % (FWHM) which is reduced to 0.32 % (FWHM) by the RF cavity in this simulation. The main reason for the remaining energy spread is the longer path that particles with higher initial divergence angles have to travel. Therefore, particles with the same energy

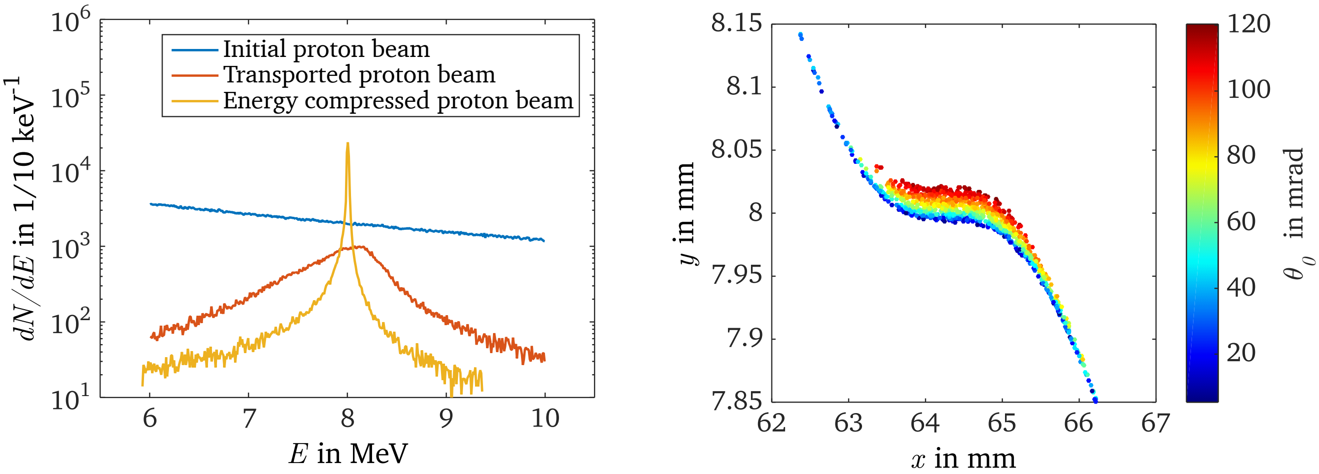

Fig. 6.2: The left image shows the simulated spectra of the initial, the transported, and the energetically compressed proton beam at the LIGHT beamline for a targeted energy of 8 MeV and in the right image the particles of the energetically compressed beam in the E-t phase space are illustrated. The main reason for the remaining energy spread of the energetically compressed fraction of the proton beam are the different initial divergence angles θ_0 as shown in the right image.

reach the RF cavity at slightly different times and do not experience the same electric field strength. This can be seen in the right image of Fig. 6.2, since the size of the compressed beam in the E-t phase space is caused by the different initial divergence angles θ_0 of the particles.

The reason for the relatively large transverse emittances of the beam is that they refer to all protons that pass the RF cavity and not only to those that are collimated and energetically compressed. Only considering the protons of the beam that are within the energy spread of ±0.2 % (acceptance range of the SIS18) leads to the following beam parameters:

- Energy spread $\Delta E/E = 0.4\,\%$ (full width)
- Horizontal emittance $\varepsilon^{2\sigma}_{n,xx'} = 8.54\,\mathrm{mm\,mrad}$ (within $\Delta E/E$)
- Vertical emittance $\varepsilon^{2\sigma}_{n,yy'} = 7.82\,\mathrm{mm\,mrad}$ (within $\Delta E/E$)
- Number of protons $N_{\mathrm{sim}} = 10^5$ (within $\Delta E/E$)

For this fraction of the beam the horizontal emittance $\varepsilon^{2\sigma}_{n,xx'}$ is still not within the acceptance range of the SIS18 ($\varepsilon^{2\sigma}_{n,xx'} = 3.12\,\mathrm{mm\,mrad}$). Since the solenoid is set up to collimate most of the beam's particles, the horizontal emittance of the beam can be reduced by removing particles with a large horizontal direction deviation. By removing all protons with $x' > 4\,\mathrm{mm\,mrad}$ the horizontal emittance of the beam corresponds exactly to the required emittance of $\varepsilon^{2\sigma}_{n,xx'} = 3.12\,\mathrm{mm\,mrad}$. The proton beam obtained in this way contains 6×10^4 protons in the simulation which are 46 % of the protons that would pass the second solenoid of the LIGHT beamline. The initial beam has 10^7 particles with an energy of (6 - 10) MeV (see Table 6.2) and the TNSA source at the experimental area Z6 typically contains 8.8×10^{10} particles in this energy range. Therefore, it can be expected that the LIGHT beamline can inject a proton beam with the following parameters into the SIS18:

- Energy spread $\Delta E/E = 0.4\,\%$ (full width)
- Horizontal emittance $\varepsilon^{2\sigma}_{n,xx'} = 3.12\,\mathrm{mm\,mrad}$
- Vertical emittance $\varepsilon^{2\sigma}_{n,yy'} = 6.04\,\mathrm{mm\,mrad}$
- Number of protons $N_{exp} = 5.3 \times 10^8$ (within $\Delta E/E$, $\varepsilon^{2\sigma}_{n,xx'}$ and $\varepsilon^{2\sigma}_{n,yy'}$)

The same simulation has also been performed for a targeted proton beam energy of 11.4 MeV and will be presented in the next section.

6.4. Simulations on the energetic compression of protons with 11.4 MeV

For protons with an energy of 11.4 MeV the first solenoid is supplied with 9.9 kA, the distance $d_{\text{cav},1}$ is set to 1750 mm, the RF cavity voltage is set to 1 MV and the parameters shown in Table 6.3 are used to generate the initial proton beam.

Table 6.3: Initial proton beam parameters for the simulations in this subsection.

N	$k_\text{B}T$	E_min	E_max	E_cut	a_2	a_1	a_0	m	q
1×10^7	6 MeV	9 MeV	14 MeV	28 MeV	-0.04 °/MeV^2	0.41 °/MeV	26.47 °	1 u	1 e

This results in a proton beam with the following parameters behind the RF cavity:

- Energy spread $\Delta E/E = 0.21\,\%$ (FWHM)
- Horizontal emittance $\varepsilon^{2\sigma}_{n,xx'} = 9.66\,\mathrm{mm\,mrad}$ (within $\Delta E/E = \pm 0.2\,\%$)
- Vertical emittance $\varepsilon^{2\sigma}_{n,yy'} = 8.37\,\mathrm{mm\,mrad}$ (within $\Delta E/E = \pm 0.2\,\%$)
- Number of protons $N_\text{sim} = 1.2 \times 10^5$ (within $\Delta E/E = \pm 0.2\,\%$)

Therefore, also in this case protons with a high horizontal direction deviation behind the solenoid are removed to reduce the horizontal emittance of the beam to $\varepsilon^{2\sigma}_{n,xx'} = 3.12\,\mathrm{mm\,mrad}$. In this simulation, the threshold had to be set to $x'_\text{max} = 1.4\,\mathrm{mm\,mrad}$. The proton beam obtained in this way contains 6.8×10^4 protons in the simulation which are 39 % of the protons that would pass the second solenoid of the LIGHT beamline. The initial beam has 10^7 particles with an energy of (9 - 14) MeV (see Table 6.3) and the TNSA source at the experimental area Z6 typically contains 4.7×10^{10} particles in this energy range. Therefore, the LIGHT beamline can inject 3.2×10^8 protons with an energy of 11.4 MeV into the SIS18 in a single shot. The results of the simulations of this chapter are summarized in the Tables 6.4a and 6.4b.

Table 6.4: The beam parameters that can be achieved with current setup of the LIGHT beamline for the injection in the SIS18.

Beam parameter	Value
Energy spread $\Delta E/E$	0.4 % (full width)
Hor. emittance $\varepsilon^{2\sigma}_{n,xx'}$	3.12 mm mrad
Vert. emittance $\varepsilon^{2\sigma}_{n,yy'}$	6.04 mm mrad
Number of protons within $\Delta E/E$ and $(\varepsilon^{2\sigma}_{n,xx'}, \varepsilon^{2\sigma}_{n,yy'})$	5.3×10^8

(a) E = 8 MeV

Beam parameter	Value
Energy spread $\Delta E/E$	0.4 % (full width)
Hor. emittance $\varepsilon^{2\sigma}_{n,xx'}$	3.12 mm mrad
Vert. emittance $\varepsilon^{2\sigma}_{n,yy'}$	6.5 mm mrad
Number of protons within $\Delta E/E$ and $(\varepsilon^{2\sigma}_{n,xx'}, \varepsilon^{2\sigma}_{n,yy'})$	3.2×10^8

(b) E = 11.4 MeV

The estimated number of particles that can be injected refer to the current setup of the LIGHT beamline. In the following, some measures are mentioned with which the number of injectable particles can be increased:

- An increase in the available PHELIX laser energy at Z6, which would increase the number of particles in the initial TNSA spectrum significantly.
- A reduction of the initial divergence for the particles in the relevant energy interval of the TNSA source, which would increase the transport efficiency and reduce the emittance growth by chromatic and spherical aberrations of the solenoid (see Section 4.4.2). This could be achieved by a TNSA target optimization or by increasing the beam size of the PHELIX laser on the target.
- An improvement of the ion capturing element to obtain more particles in the required transverse emittance range.
- A reduction of the distance $d_{\text{cav},1}$ between the TNSA source and the RF cavity, which would require an RF cavity with more power and geometric adjustments in and around the Z6 target chamber.

For some applications, such as the planned stopping power measurements, a high beam flux and a short temporal length of the bunch is more valuable than a small energy spread. At the LIGHT beamline the highest particle flux (for the transported beam) is achieved by a temporal compression with the RF cavity in combination with the focusing of a second solenoid. Within the scope of this thesis, this was investigated for laser-accelerated protons and carbon ions using simulations and experiments. The results of this are presented in the following two chapters.

7. Generation of high proton fluxes

In this chapter, the results of a beamtime that was conducted in January 2020 are presented. Prior to this beamtime the transport, the focusing and the temporal compression of 8 MeV protons had already been successfully performed separately at the LIGHT beamline [Busold et al., 2013, 2014b, 2015; Jahn et al., 2019]. From these results, it was expected, that the focusing of the temporally compressed bunch would lead to a very high particle flux [Jahn et al., 2019]. The generation of such high particle fluxes was therefore the main goal of this experimental campaign.

In the following, the transport, focusing and temporal compression of the proton beam is considered with simulations first. After that, the measurements of the experimental campaign are described in detail and the corresponding results of their evaluation are presented. A discussion of the discrepancies between the experimental data and the simulations is then given in the last section of this chapter.

7.1. Simulation studies for the generation of high proton fluxes

The following simulations will be compared to the experimental data to identify possible systematic measuring errors and explain unexpected observations in the measurements. The energy of the resulting proton bunch in the experiment was 7.7 MeV. Therefore, in the following simulations, the particle flux of a proton beam with 7.7 MeV is optimized for the corresponding beamline setup of the experiment. The setup of the LIGHT beamline in the experimental campaign and the simulations corresponds to the setup that was already shown in Fig. 4.6. In Table 7.1 the parameters that are used to generate the initial proton beam are given.

Table 7.1: Parameters that were used to generate the initial proton beam in the simulations of this subsection.

N	$k_B T$	E_{min}	E_{max}	E_{cut}	a_2	a_1	a_0	m	q
1×10^7	6 MeV	5 MeV	10 MeV	28 MeV	-0.04 $^\circ/\mathrm{MeV}^2$	0.41 $^\circ$/MeV	26.47 $^\circ$	1 u	1 e

7.1.1. Transport and focusing of the proton beam

To transport protons with a mean energy of 7.7 MeV in the simulation, the first solenoid has to be supplied with 8.23 kA (see Section 4.4). Simultaneously supplying the second solenoid with a current of 7.75 kA leads to a focal spot of the transported beam behind the second solenoid. In Fig. 7.1 the beam sizes in the x-y-plane are shown for different distances to the TNSA target d (behind the second solenoid) as well as for different magnetic field distributions used for the solenoids (see Section 4.4.3) and different beam size definitions.

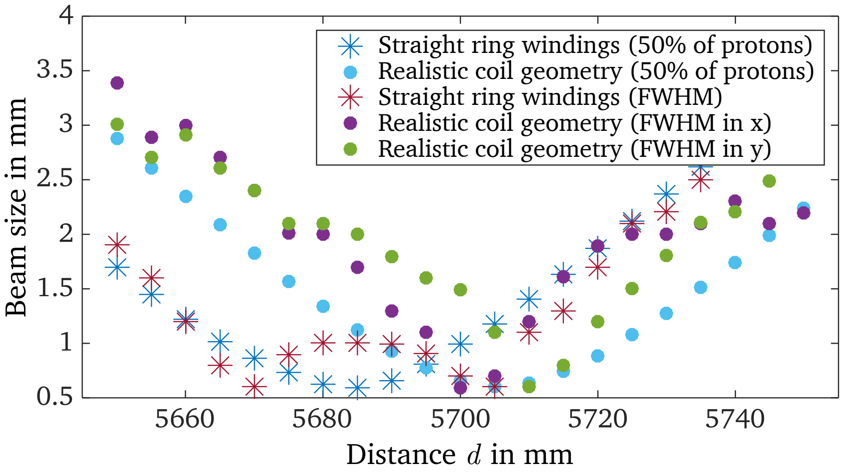

Fig. 7.1: Beam sizes for different distances d, different beam size definitions and different magnetic field distributions used for the solenoid magnets.

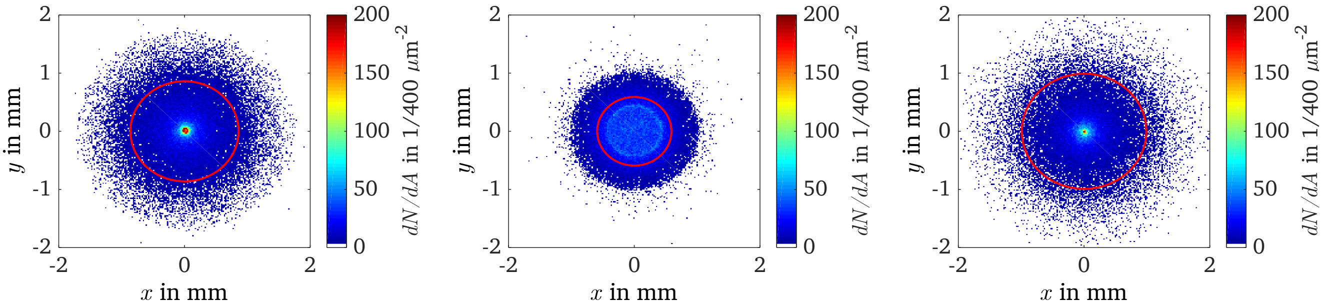

(a) Straight ring windings
$d = 5670$ mm

(b) Straight ring windings
$d = 5685$ mm

(c) Straight ring windings
$d = 5705$ mm

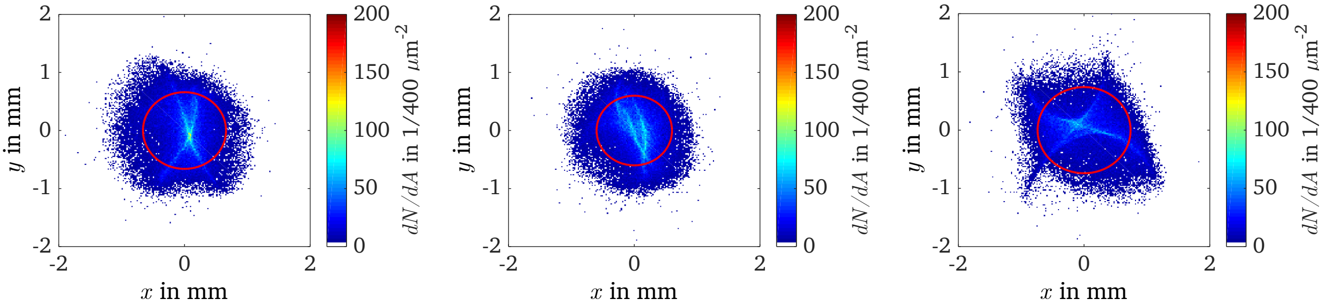

(d) Realistic coil geometry
$d = 5700$ mm

(e) Realistic coil geometry
$d = 5705$ mm

(f) Realistic coil geometry
$d = 5715$ mm

Fig. 7.2: Transported proton beams for different distances d to their origin and different magnetic field distributions of the solenoid magnets. The red circles are enclosing 50 % of the total proton number.

Also, for some distances, the beam profiles are illustrated in Fig. 7.2. In case of the beam size definition that is called "50 % of protons" in the legend of Fig. 7.1, the radius of a circle is given that encloses 50 % of the transported protons. This circle is also shown in red in the images of Fig. 7.2. For every focal spot size definition and for both magnetic field distributions that are used, the minimum size is close to 0.5 mm, albeit at different distances. The plateau of the FWHM for the straight ring windings at approximately 5685 mm in Fig. 7.1 is striking, which can be explained by the uniform particle distribution of the beam profile around this distance (see Fig. 7.2b). These simulations therefore illustrate that only the particle distribution in the focal spot is changed by the imperfections in the magnetic field distribution and not its size. This was also expected due to the similar emittances of the beam after the first solenoid for the different magnetic field distributions (see Section 4.4.3).

In the next subsection, the particle distribution in the beam profile shown in Fig. 7.2f is described in more detail.

7.1.2. Analyzing the beam filamentation in the focal spot

In Fig. 7.3 the individual particles of the beam profile shown in Fig. 7.2f are illustrated. Thereby, in the left picture, the color of the particles corresponds to their energy E, while in the right picture it corresponds to their initial divergence angle θ_0.

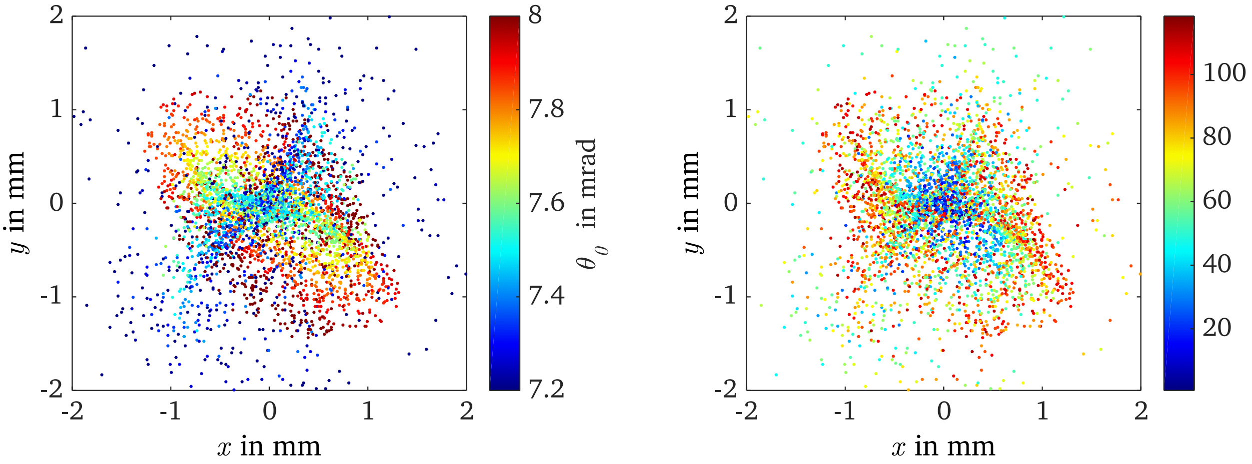

Fig. 7.3: Particles of the proton bunch at a distance of 5715 mm to their origin. In the left image, the color of the particles corresponds to their energy E, while in the right image it corresponds to their divergence angle θ_0 at the origin of the beamline.

In these two pictures the effect of the chromatic aberration, the spherical aberration and the astigmatism of the solenoid magnets can be seen, which are now considered one after the other. The chromatic aberration was found to be the most dominant aberration at the LIGHT beamline in Section 4.4.2. This aberration is caused by the dependency of the focal length of the solenoid on the particles' momentum. Therefore, the particles of each energy are reaching the nominal axis at different positions. In the left picture of Fig. 7.3 it can be seen, that at the illustrated position particles with an energy of (7.5 - 7.8) MeV are closest to the nominal axis $(x = y = 0)$. The particles with an energy of (7.8 - 8) MeV will therefore reach the nominal axis behind the considered position while the particles with an energy of (7.2 - 7.5) MeV have already passed the nominal axis. The elliptical or S-shaped distribution of the particles of each energy is caused by the astigmatism which in turn is caused by the connection cables of the solenoid as shown in Subsection 4.4.3. In the right picture of Fig. 7.3 it can be seen that the particles with a smaller initial divergence angle are closer to the nominal axis at the illustrated position. Since the first solenoid collimates the beam, particles with a large initial divergence angle have the largest distance to the nominal axis in the second solenoid and, as discussed in Section 4.2, therefore experience a stronger focusing force (spherical aberration). Therefore, many particles with a large initial divergence angle have already passed the nominal axis at the illustrated position.

Due to the elliptical or S-shaped distribution of the particles of each energy, multi-peak structures in the temporal beam profile can occur if just a fraction of the beam is considered. This is indicated in Fig. 7.4. Thereby, the diameter of the blue and the red circle in the left image of Fig. 7.4 corresponds to the detection area (0.5 mm diameter) of the time of flight diamond membrane detector that is typically used in the experimental campaigns with the LIGHT beamline [Jahn et al., 2018]. In the experiments, this ultimately leads to an unclear correlation between the shape of the measured temporal beam profile and the phase or the electric field strength of the RF cavity, which makes a systematic adjustment of the RF cavity with a filamented beam unfeasible. Therefore, during the adjustment of the RF cavity the beam filamentation has to be suppressed with a scattering foil in the experiments.

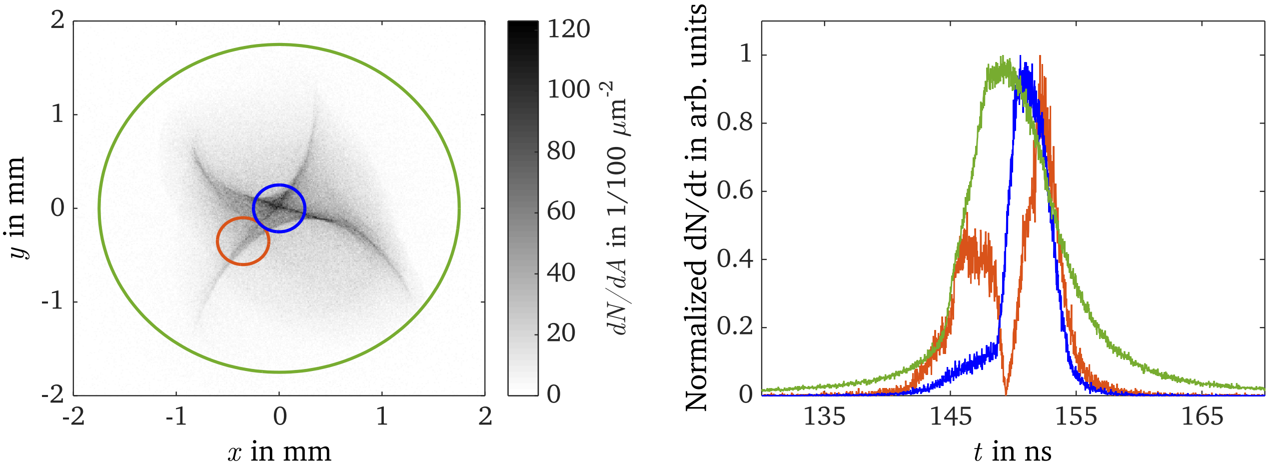

Fig. 7.4: In the left image the number of particles per area of the proton bunch at a distance of 5715 mm to their origin is shown and the temporal profiles of the beam fractions enclosed by the green, blue and red rings are illustrated in the right image.

Due to the energy spread of the transported bunch, its temporal width increases over the entire length of the LIGHT beamline. Therefore, the temporal width of the bunch is 7 ns (FWHM) in the focal spot of the second solenoid as can be seen by the green line in the right image of Fig. 7.4. In the next section, the RF cavity is now used to temporally compress the bunch and thus increase the particle flux at this position.

7.1.3. Temporal compression of laser-accelerated proton beams

As a first step, the required RF cavity voltage for the temporal compression shall be determined with Equation 5.25. For the used setup the ratio $d_{\text{cav,1}}/d_{\text{cav,2}}$ is 0.66 and according to Table 6.1a U_{Ecomp} is 0.41 MV which results in a U_{tcomp} of 0.68 MV. In the simulations, the voltage was then systematically optimized and the smallest temporal bunch width was found for an RF cavity voltage of 0.67 MV.

In the left image of Fig. 7.5 the energy spectra of the initial, the transported and the temporally compressed proton beam are compared at a distance of 5.7 m from the TNSA source. The spectrum of the temporally compressed beam has an U-shape with an energy spread of 4.54 %. According to Equation 5.26 the energy spread of the resulting beam is 5.2 %, which is therefore consistent with the simulations.

In the right image of Fig. 7.5 the beam is shown in the E-t phase space and the color of the particles corresponds to their initial divergence angle θ_0. The temporal width of the beam at this position is 60 ps

(FWHM). As in the case of the energetic compression in Chapter 6, the temporal width of the beam is only limited by the different path lengths of the particles with different initial divergence angles θ_0 in the simulation.

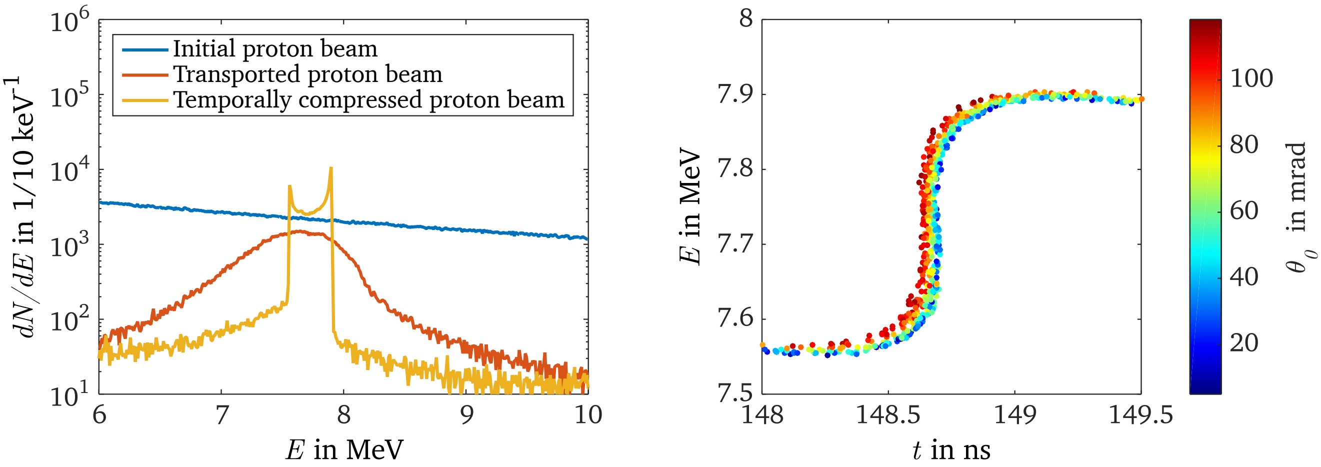

Fig. 7.5: The left image shows the simulated energy spectra of the initial, the transported, as well as the temporally compressed proton beam at the LIGHT beamline for a targeted energy of 7.7 MeV. The right image shows the particles of the temporally compressed beam with their initial divergence angle θ_0 in E-t phase space.

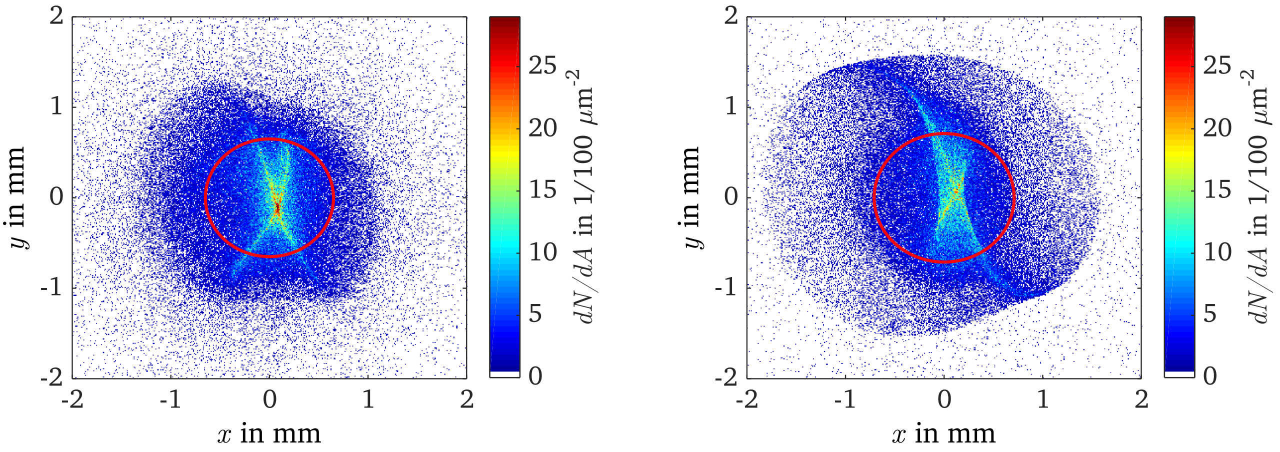

Fig. 7.6: Comparison of the focal spots at the LIGHT beamline for a transported proton beam (left image) and a transported proton beam that is temporally compressed by the RF cavity (right image).

In the experimental campaign, the spatial beam profile of the temporal compressed beam was measured in the focal spot. Therefore, the extent to which the temporal compression changes the beam profile in the focal spot of the second solenoid is also investigated with simulations. The beam profiles of the transported and the temporally compressed proton beam after the second solenoid are shown in Fig. 7.6. As can be seen, the temporal compression changes the beam profile only slightly and the beam size increases only from 1 mm to 1.3 mm.

This concludes the simulation studies of this chapter. The most important parameters of the temporal compressed and focused proton bunch are summarized in Table 7.2. In the next section, the measured beam parameters in the experiment are presented.

Table 7.2: Parameters of the temporal compressed and focused proton beam that have been determined with the simulations shown in this section.

Parameter	Value
Mean energy	7.7 MeV
Energy spread (full width)	4.54 %
Temporal bunch width	60 ps
Focal spot size	1.3 mm

7.2. Generation and measurement of high proton fluxes

In the following, the setup of the beamline, the alignment of the solenoids and the adjustment of the RF cavity during the experimental campaign are explained, and the most important results obtained in this process are presented and evaluated.
Fig. 7.7 shows the setup of the LIGHT beamline during the experimental campaign along with the used diagnostics.

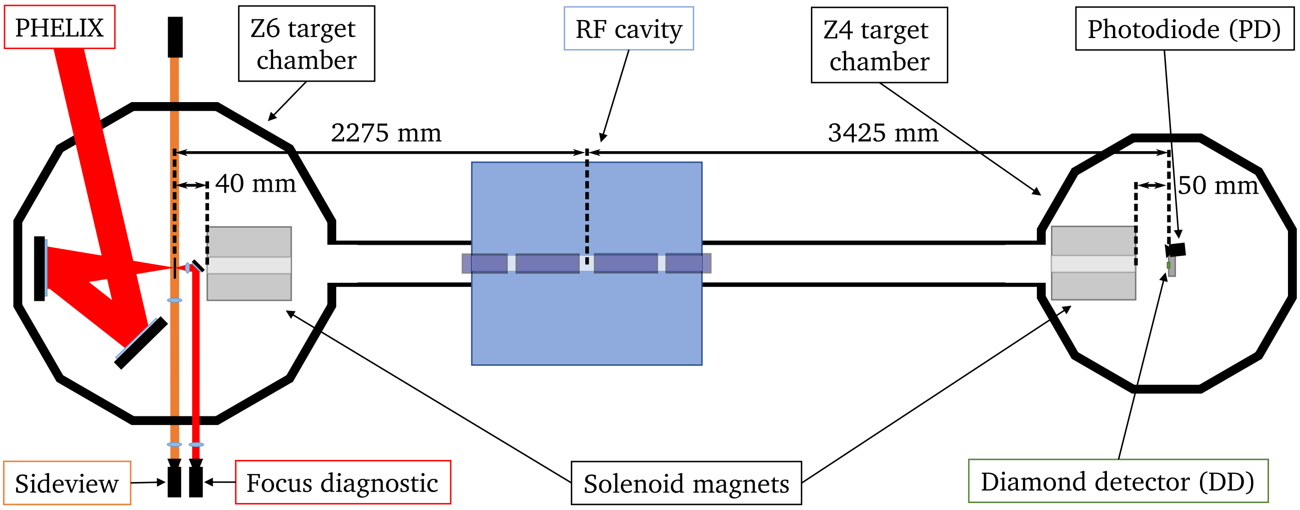

Fig. 7.7: Schematic setup of the LIGHT beamline during the experimental campaign in January 2020.

After the PHELIX beam enters the Z6 target chamber, a mirror reflects the beam on the off-axis parabola which then focuses it on the TNSA target. The focus of the PHELIX beam and the TNSA target are aligned with the sideview and the focus diagnostic. The sideview images the TNSA target on a camera. Thereby, a laser pointer is used as a backlight. The focus diagnostic images the PHELIX beam at the position of the target on a camera. The first optics of the focus diagnostic are mounted on a motorized linear stage so that they can be moved away from the beamline axis.

For the alignment of the capturing solenoid, the transported proton beam is diagnosed with RCF stacks in front of the RF cavity and at the entrance of the second solenoid. Thereby the RCF stacks are configured, so that the protons with an energy of 5.8 MeV, 8 MeV and 9.8 MeV are stopped in the active layers. The size of the beam in the active layers is then used for the adjustment of the magnetic field strength and its position for the solenoid alignment. Since even a slight displacement ($\sim \mathrm{mm}$) of the solenoid results in a deflection of the beam, the alignment is very crucial for the capture efficiency and can be very time-consuming due to the limited shot rate of the PHELIX laser. Therefore, the solenoid is mounted on a hexapod (HXP100-MECA V6), whose adjustment platform can perform motions and rotations in the range of µm or mdeg. This hexapod was installed in the Z6 target chamber in 2019 as one of the first projects of this work. In Fig. 7.8 the hexapod is shown in the Z6 target chamber with and without the mounted solenoid.

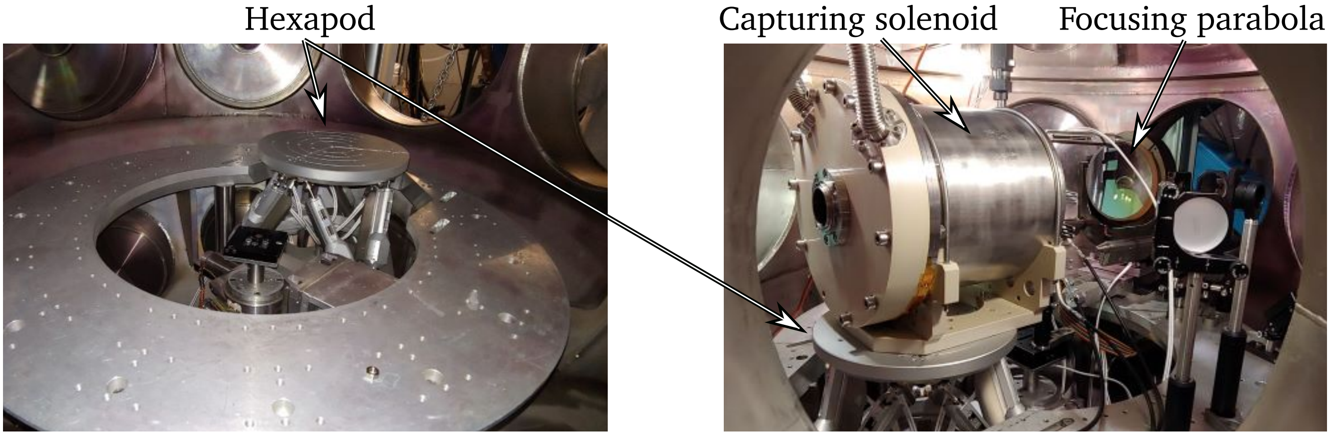

Fig. 7.8: Images of the hexapod in the Z6 target chamber before and during an experimental campaign with the LIGHT beamline.

The second solenoid is adjusted in the same way, but due to the short distance between the second solenoid and the middle of the Z4 target chamber, the alignment is far less demanding. After the minimization of the focal spot size in the Z4 target chamber, the temporal profile and the energy of the transported proton beam can be measured with the Diamond Detector (DD) and the photodiode. In this experimental campaign, the diamond membrane detector [Jahn et al., 2018] is placed in the focal spot of the proton beam which had a distance of $d_{\mathrm{DD}} = (5.70 \pm 0.05)\,\mathrm{m}$ to the TNSA target. The photodiode was placed right next to the diamond detector and measured the electromagnetic radiation that is generated by the interaction between the PHELIX laser and the TNSA target. Diamond detector and photodiode were connected to an oscilloscope with cables of the same type and length. Therefore, the time of flight of the bunch from the TNSA target to the diamond detector t_{bunch} can be determined by the time difference between the rising edge of the photodiode signal and the diamond detector signal Δt_{oszi}, since the electromagnetic radiation of the plasma travels with the speed of light c, so

$$t_{\mathrm{bunch}} = \Delta t_{\mathrm{oszi}} + d_{\mathrm{DD}}/c. \tag{7.1}$$

The time of flight can then be used to determine the energy of the bunch

$$E_{\mathrm{bunch}} = \gamma_{\mathrm{bunch}} \cdot m_0 c^2 = \frac{m_0 c^2}{\sqrt{1-\beta_{\mathrm{bunch}}^2}} \tag{7.2}$$

with

$$\beta_{\text{bunch}} = \frac{d_{\text{DD}}}{c \cdot t_{\text{bunch}}}. \tag{7.3}$$

It should be noted, that this is only valid if the energy of the bunch is constant over the entire distance, so only if the mean energy of the bunch is not changed by the RF cavity. The result of one of the first measurements with this setup is shown in Fig. 7.9 as an example.

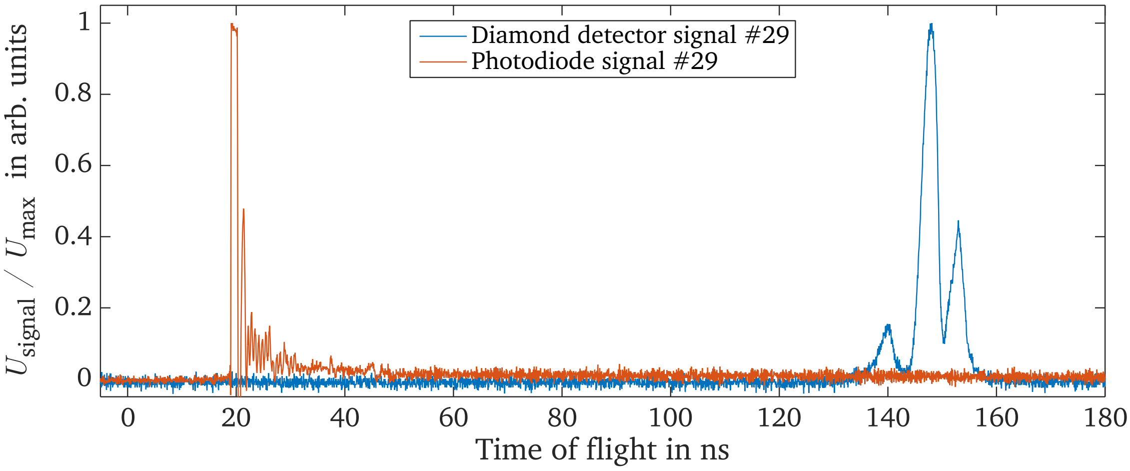

Fig. 7.9: Normalized signals of the photodiode and the diamond detector, which were recorded by an oscilloscope. The signal of the photodiode is caused by the electromagnetic radiation of the plasma, whereas the signal of the diamond detector is caused by the transported protons.

Thereby, 30 % of the rising edge of the photodiode signal corresponds to the time of flight of the electromagnetic radiation from their origin to the diamond detector ($d_{\text{DD}}/c = 19$ ns) and therefore the diamond detector signal corresponds to the time of flight of the transported protons. The triple peak structure of the diamond detector signal is due to the beam filamentation and the small detection area of the diamond detector as shown in the simulations of Section 7.2. To get the temporal profile of the entire proton bunch, its filamentation was eliminated by a scattering foil. The middle peak corresponds to a proton energy of 7.7 MeV. According to the Stopping and Range of Ions in Matter (SRIM) code, the scattering of an RCF of type *Gafchromic* HD-V2 (about 100 µm thick) at the second solenoid causes a mean scattering angle of 13 mrad, which corresponds to a transverse position deviation of 3.86 mm at the position of the diamond detector if the scattering foil is placed in front of the second solenoid (the size of the whole beam at the position of the diamond detector was approximately 2.5 mm). This scattering was sufficient to eliminate the beam filamentation, which can be seen by the Gaussian-like diamond detector signal of shot 68 shown in Fig. 7.10. The temporal width of this signal is (7.50 ± 0.04) ns (FWHM). According to Equation 5.3 this corresponds to an energy spread of $\Delta E/E \approx 10\,\%$, which agrees well with the predictions of the simulations in Section 7.2.

The elimination of the beam filamentation allows the systematical adjustment of the RF cavity for the temporal compression, which is illustrated in Fig. 7.11. As can be seen, changing the RF cavity phase ϕ (delay between the RF cavity and the PHELIX laser) leads to a different energy transfer of the RF cavity to the nominal particle (particle with the mean energy of the bunch) whereas an increase in the RF cavity voltage changes the energy spread of the bunch and therefore the temporal width of the bunch at the position of the diamond detector. The absolute values of the used RF cavity voltages are estimated, since the applied voltages were only measured relative to each other.

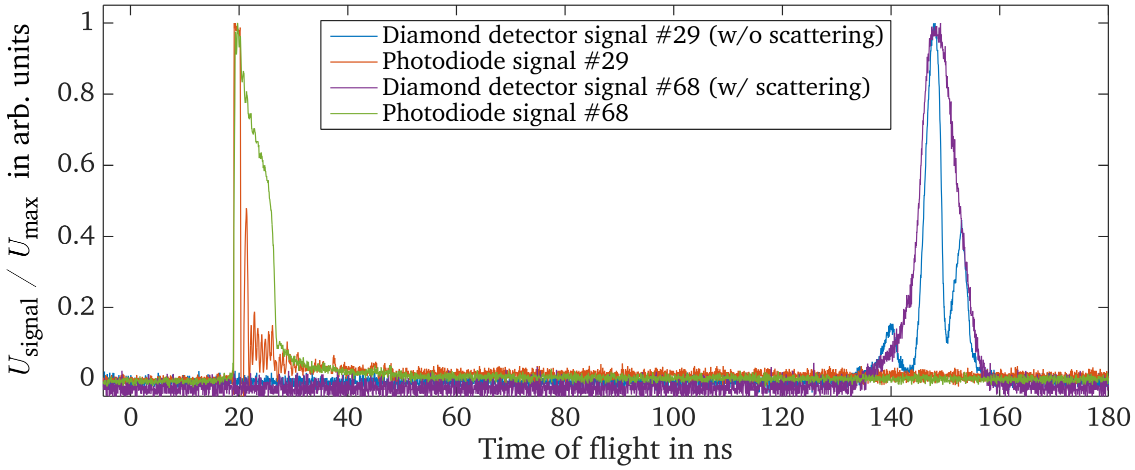

Fig. 7.10: Normalized signals of the photodiode and the diamond detector which were recorded by the oscilloscope for shot 29 and 68. The triple peak structure of the diamond detector signal of shot 29 is caused by the filamentation of the proton beam. For shot 68 the filamentation is eliminated by a scattering foil.

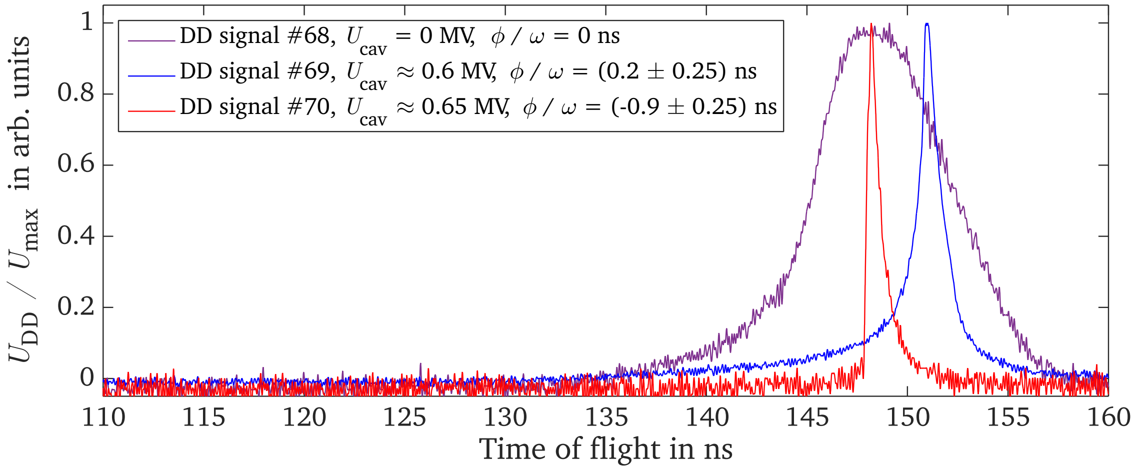

Fig. 7.11: Temporal profile of the transported proton bunch at the LIGHT beamline for different RF cavity voltages U_{cav} and phases ϕ.

With a **temporal width of (742 ± 40) ps (FWHM)**, the signal of shot 70 has the smallest temporal width measured in this experiment. Therefore, the RF cavity parameters of this shot were used to measure the transverse beam profile of the temporally compressed bunch with the RIS. For this measurement, the scattering foil was removed to obtain the smallest possible focal spot. The used RCF stack configuration and the deposited energy in the first four active layers of the RCF stack are shown in Fig 7.12.

The red circle in the second active layer has a **diameter of 1.38 mm**. Since the total deposited energy is highest in the second active layer and then decreases significantly in the third active layer, it can be concluded that most of the protons had an energy between 7.7 MeV and 8 MeV, which is consistent with the results of the ToF measurements.

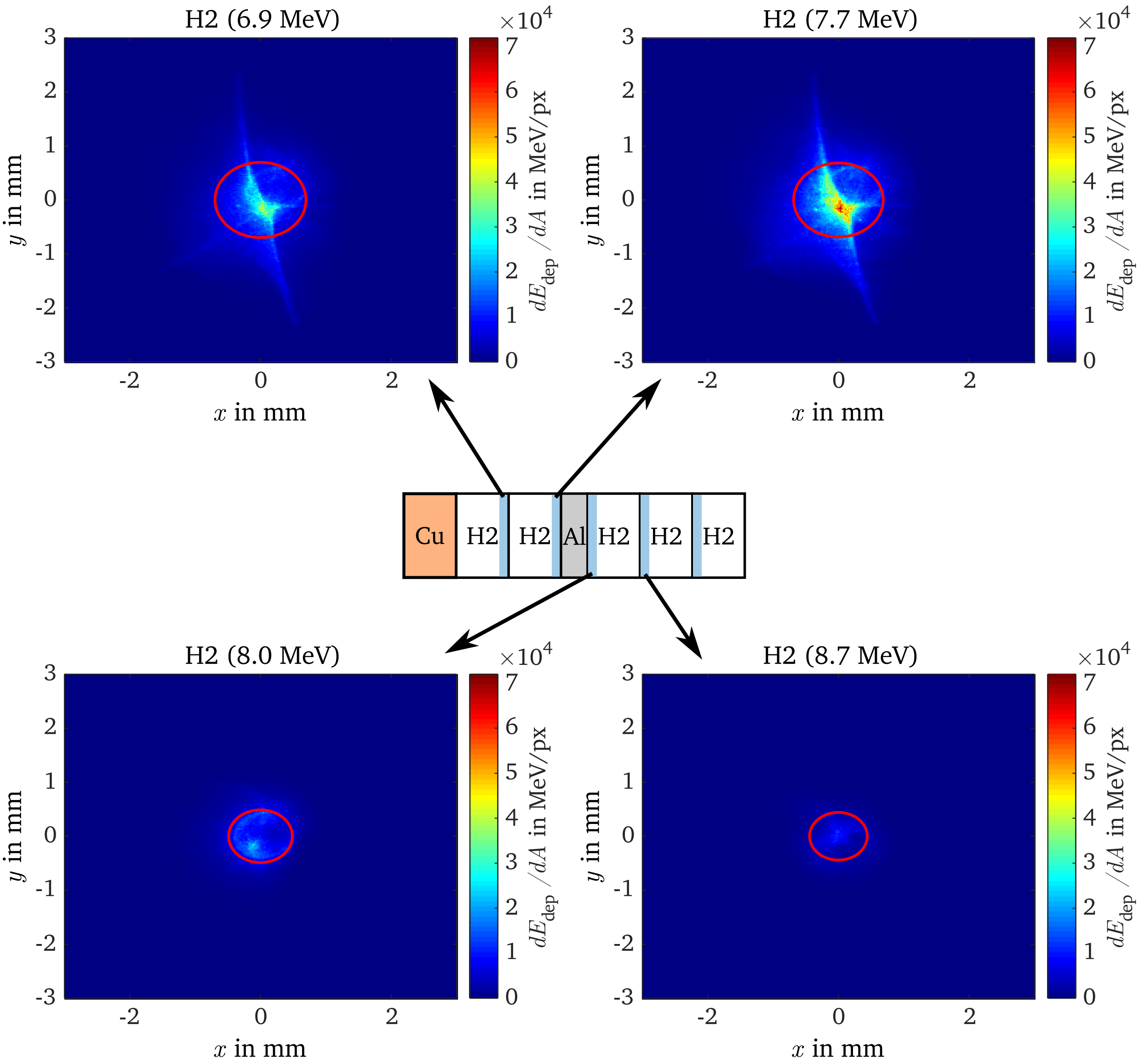

Fig. 7.12: RCF configuration and the deposited energy of the temporal compressed bunch in the first four active layers of the stack. The copper (Cu) layer had a thickness of 100 µm and the aluminum (Al) layer a thickness of 25 µm. The specified energies in the header of the images correspond to the energy of the protons that are, according to SRIM, stopped in the active layer and the red circles are enclosing 50 % of the total deposited energy.

In the next step, the particle flux of the proton bunch is determined, which requires the number of protons in the bunch. Therefore, a particle distribution must be found that deposits the same amount of energy in the active layers of the RCF stack as was measured in the experiment. This is done with two different methods in the following. The first method is based on a stepwise adjustment of the number of particles that are stopped in the active layers. Thereby, the number of particles in the passive layers are set by a linear interpolation. The idea of this method was first published in [Schollmeier et al., 2014] and was implemented in an RCF evaluation routine as part of this work, which has also been published [Schmitz et al., 2022]. The main advantage of this method is that no particle distribution has to be assumed.

In the second method, a given particle distribution is optimized so that its deposited energy matches the measured deposited energy, as is done in Section 2.2 for the TNSA source at Z6 and an exponentially decaying energy spectrum. Thereby, the following particle distribution are used:

- Gaussian distribution: $\frac{dN}{dE} = N_0 \exp\left(-\frac{1}{2}\left(\frac{E-E_\mu}{\sigma}\right)^2\right) + N_{\text{bg}}$
- Gaussian distribution (fixed σ): $\frac{dN}{dE} = N_0 \exp\left(-\frac{1}{2}\left(\frac{E-E_\mu}{\tilde{\sigma}}\right)^2\right) + N_{\text{bg}},\ \tilde{\sigma} = 0.32$
- Parabolic distribution: $\frac{dN}{dE} = N_0\,(E-E_\mu)^2 + N_{\text{bg,u}},\ \frac{dN}{dE}(E > E_\mu + \Delta E_1, E < E_\mu - \Delta E_2) = N_{\text{bg}}$

So in all three distributions E_μ is the mean energy, N_{bg} is a constant background of particles, and the parameter N_0 only influences the number of particles that the distribution contains. The background N_{bg} is required to properly reproduce the deposited energy at higher ion energies which is caused by particles with very small initial divergence angles. The fixed standard deviation of the second Gaussian distribution $\tilde{\sigma}$ corresponds to an energy spread of $\Delta E/E \approx 10\,\%$ (FWHM), as it would be expected for a transported, uncompressed beam. According to the simulation studies in Section 7.2 the energy spectrum of the temporal compressed beam has an U-shape which can be reproduced with the parabolic distribution. The resulting particle distributions are shown in Fig. 7.13 and their most important parameters are listed in Table 7.3.

Table 7.3: Number of particles N_{ges}, mean energy E_μ and energy spread $\Delta E/E$ of the particle distributions that were adjusted or optimized to match the measured deposited energies shown in Fig 7.12. The square root of the mean squared deviation (MSD) of the deposited energies divided by the maximum measured deposited energy $\bar{E}_{\text{dep}}^{\text{max}}$ are also given.

Distribution	N_{ges}	E_μ	$\Delta E/E_\mu$	$\sqrt{\text{MSD}}/\bar{E}_{\text{dep}}^{\text{max}}$
Gradually adjustment	(7.29 ± 0.64) × 10^8	7.70 MeV	5.92 % (2σ)	0
Gaussian	(7.21 ± 0.72) × 10^8	7.82 MeV	6.60 % (2σ)	1.53 %
Gaussian (fixed σ)	(7.81 ± 0.79) × 10^8	7.80 MeV	16.03 % (2σ)	12.24 %
Parabolic	(7.30 ± 0.81) × 10^8	7.81 MeV	4.91 % (full width)	1.47 %

To determine the uncertainty of the particle number N_{ges}, the corresponding method was applied to the minimum and maximum measured deposited energies. As can be seen in Fig 7.13 and by the mean squared deviation (MSD) in Table 7.4, all obtained particle distributions except the normal distribution with the fixed standard deviation can reproduce the RIS measurement. In addition, the particle number, energy and energy deviation of the distributions, that reflect the measurement well, differ only slightly from each other. It can therefore be concluded that these values apply to the measured spectrum. For a definite assignment of a specific distribution function, the pure RIS measurement does not provide enough data points. However, according to the ToF measurements and the simulation studies in Section 7.2, it is very likely that the measured beam had an energy spectrum similar to the one shown in Fig 7.13d.

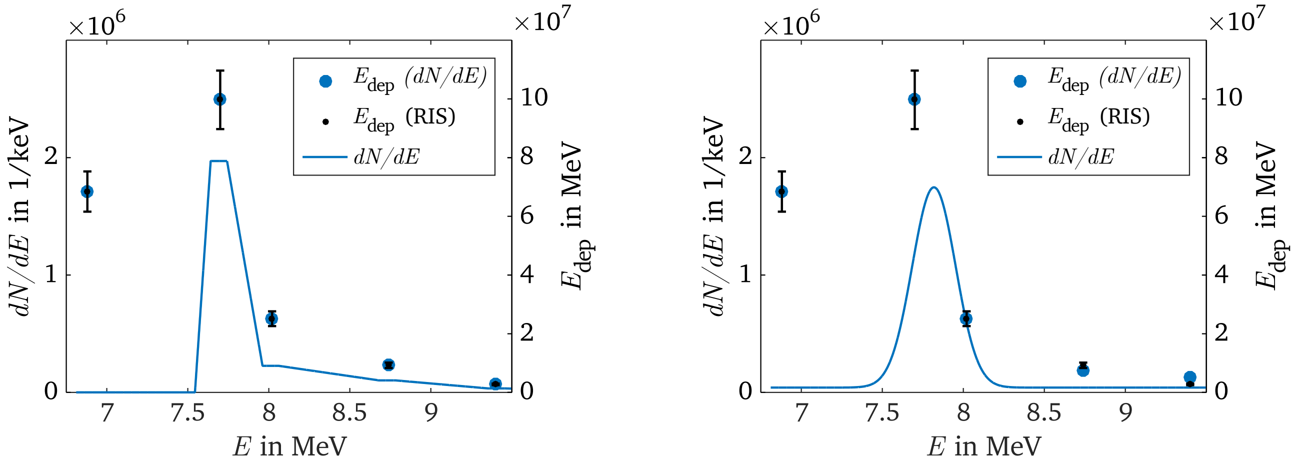

(a) Gradually adjustment with linear interpolation

(b) Optimization of a normal distribution

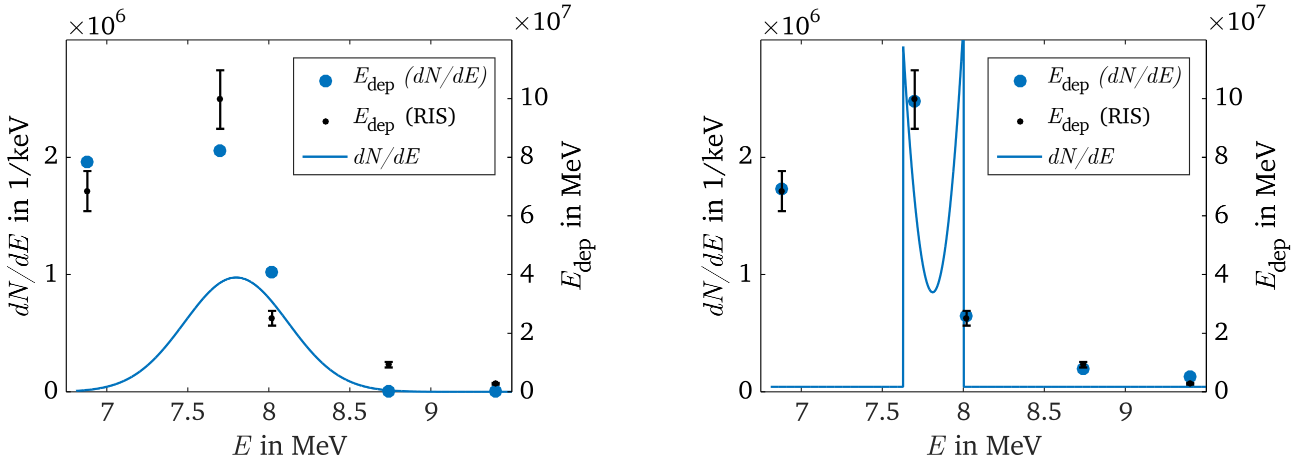

(c) Optimization of a normal distribution with $\tilde{\sigma} = 0.32$

(d) Optimization of a parabolic distribution

Fig. 7.13: Particle distributions whose deposited energies are adjusted or optimized to match the RIS measurement shown in Fig 7.12. In addition, the deposited energies of the spectra are compared to the measured deposited energies in each case.

With the number of particle thus obtained, the proton beam is well-characterized for most applications. The most important beam properties are summarized in Table 7.4. Thereby, the number of protons that corresponds to the gradually adjusted particle distribution are used, so the values given are identical to those published in [Metternich et al., 2022].
In the next section, the measurements are compared with the simulations of the Section 7.2 to evaluate the accuracy of the simulations and to identify possible systematic errors in the measurements.

Table 7.4: Parameters of the proton beam obtained during an experiment performed as part of this work.

Parameter	Value	Determined by
Number of protons	$(7.29 \pm 0.64) \times 10^8$	RIS measurement
Mean energy	(7.72 ± 0.14) MeV	ToF measurement
Energy spread	(4.91 ± 0.82) %	RIS measurement
Temporal bunch width	(742 ± 40) ps	ToF measurement
Focal spot size (50 % of protons)	(1.38 ± 0.02) mm	RIS measurement
Particle fluence in the focal spot	$(2.44 \pm 0.21) \times 10^8\,\mathrm{mm}^{-2}$	Parameters above
Particle flux in the focal spot	$(3.28 \pm 0.24) \times 10^8\,\mathrm{ns}^{-1}\,\mathrm{mm}^{-2}$	Parameters above
Beam current	(157 ± 16) mA	Parameters above

7.3. Comparison of the measurements and the simulations

In Table 7.5 the measured and the simulated parameters of the focused and temporal compressed proton beam are listed side by side.

Table 7.5: Parameters of the proton beam that were achieved during a beamtime in January 2020 and in the simulation studies of Section 7.2. Since the coils of the solenoid magnets in the experiment have N_{exp} = 112 windings and the coil that is used to determine the magnetic field distributions in the simulation only have N_{sim} = 100 windings, the specified current for the solenoids in the simulation are multiplied by the ratio $N_{\text{sim}}/N_{\text{exp}}$ (for a solenoid $B_0 \propto NI/L$ applies with L = 150 mm being the length of the coil [Demtröder, 2013]).

Parameter	Experiment	Simulation	Deviation
Capture efficiency	(9.10 ± 3.21) %	9.58 %	5.01 %
Mean energy	(7.72 ± 0.14) MeV	7.7 MeV	0.26 %
Energy spread	(4.91 ± 0.82) %	4.54 %	8.15 %
Temporal bunch width	(742 ± 40) ps	60 ps	> 10
Focal spot size that contains 50 % of protons	(1.38 ± 0.02) mm	1.3 mm	6.15 %
Current supplied to the first solenoid	$\sim$ 7.94 kA	7.32 kA	8.47 %
Current supplied to the second solenoid	$\sim$ 7.24 kA	6.75 kA	7.26 %
RF cavity voltage	$\sim$ 0.65 MV	0.68 MV	4.41 %

So except of the temporal bunch width, the relative deviation of all parameters is less than 10 %. The deviation of temporal bunch widths can be caused by anything that was not taken into account in the simulation or in the evaluation of the experimental data. The most likely causes are

- The scattering foil in the ToF measurements
- Incorrect settings or alignments of the beamline components
- Saturation effects of the used diagnostics
- Space charge effects
- A non-negligible initial emittance of the TNSA-generated ion beam
- A radially dependent energy transfer of the RF cavity

The influence of these effects on the beam parameters are estimated one by one in the following.

The scattering foil in the ToF measurements

According to SRIM, a monochromatic proton beam with 7.7 MeV has a Gaussian distributed energy spectrum after the scattering foil with a FWHM of 75 keV. This energy spread results in a temporal width of 30 ps (FWHM) over the distance between the scattering foil and the diamond detector (300 mm). Therefore, the scattering foil cannot explain the deviation between the measured and simulated temporal bunch width.

Incorrect settings or alignments of the beamline components and possible saturation effects

For the considerations of these points, some more details about the alignment procedure, the setting accuracies and the shot-to-shot variations in the experiment are given. The main amplifier of the PHELIX laser consists of five individual amplifier heads. If all of them are used simultaneously, the shot rate of the laser system is limited to about one shot per 90 minutes to get a sufficient cooling time for the Nd:glass of the amplifiers. During the alignment phase of the LIGHT beamline only two to three amplifier heads are used simultaneously which therefore allows a shot rate of 1 shot per (30 - 45) minutes at the expense of laser energy. Nevertheless, the alignment process remains the most time-consuming step in experimental campaigns and slight deviations from the optimal settings cannot be ruled out.

As a next step, the shot-to-shot variations and the setting accuracies shall be discussed. In this context, the solenoid magnets are considered first. In the case that the maximum energy of the TNSA spectrum is higher than the energy that shall be transported, the mean energy of the transported bunch is only depending on the current that is supplied to the first solenoid. The mean relative deviation of this current is less than 1 % in the experiments, which leads to a very stable transported proton beam energy.

The same applies for the shot-to-shot variations of the RF cavity voltage ($\sim$ 1 %) as well as for the delay between the RF cavity and the PHELIX laser ($\sim$ 0.5 ns). Therefore, only slight deviations of the temporal width and the height of the diamond detector signal are observed in the experiment. In fact, the relative influence of the RF cavity voltage on the diamond detector signal is smaller than it would be expected from the simulations, which is shown in Fig 7.14.

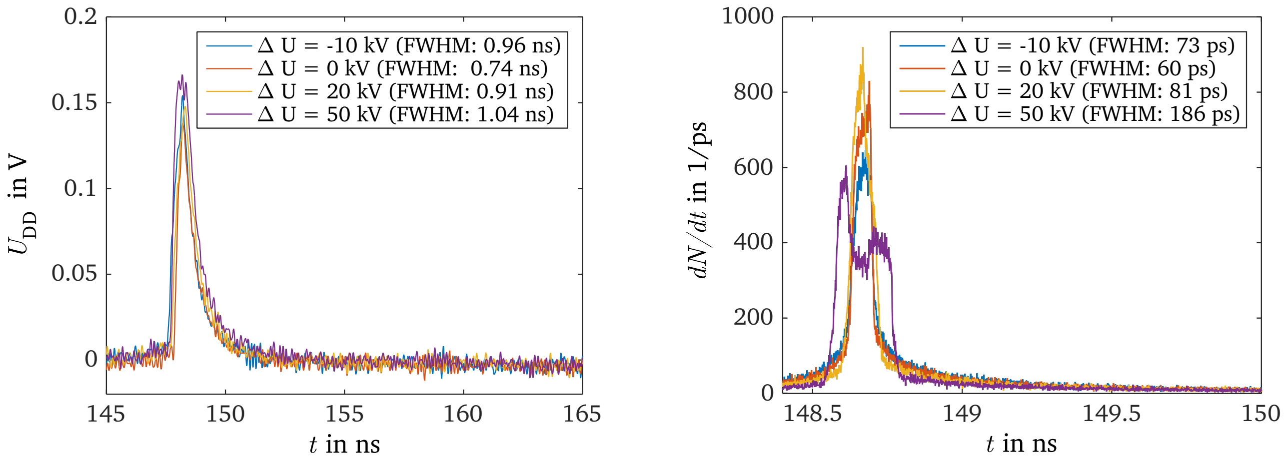

(a) Experiment

(b) Simulation

Fig. 7.14: Comparison of the temporal widths (FWHM) in the simulation and the experiment for different deviations ΔU from the optimal RF cavity voltage for the temporal compression.

This observation strongly suggests saturation effects in the diamond detector. However, the other effects mentioned above are also possible causes for this.

Space charge effects

In Fig. 7.15 the electric field in longitudinal direction $E_{z,\mathrm{sc}}$ (on axis and at the edge of the beam) and the defocusing strength κ_{sc} caused by space charge effects are shown for different beam radii r_0 and different temporal bunch widths τ. The equations derived in Section 3.7 are used to generate these images. Thus, a cylindrical beam with 7.29×10^8 homogeneously distributed protons is assumed. In addition, the solenoid magnets are assumed to act as magnetic mirrors for the TNSA-generated electrons that would otherwise move along with the transported beam, so the space charge neutralization factor f_e in Equation 3.32 is set to zero. In the following, the influence of the space charge effects on the longitudinal beam dynamics are considered first.

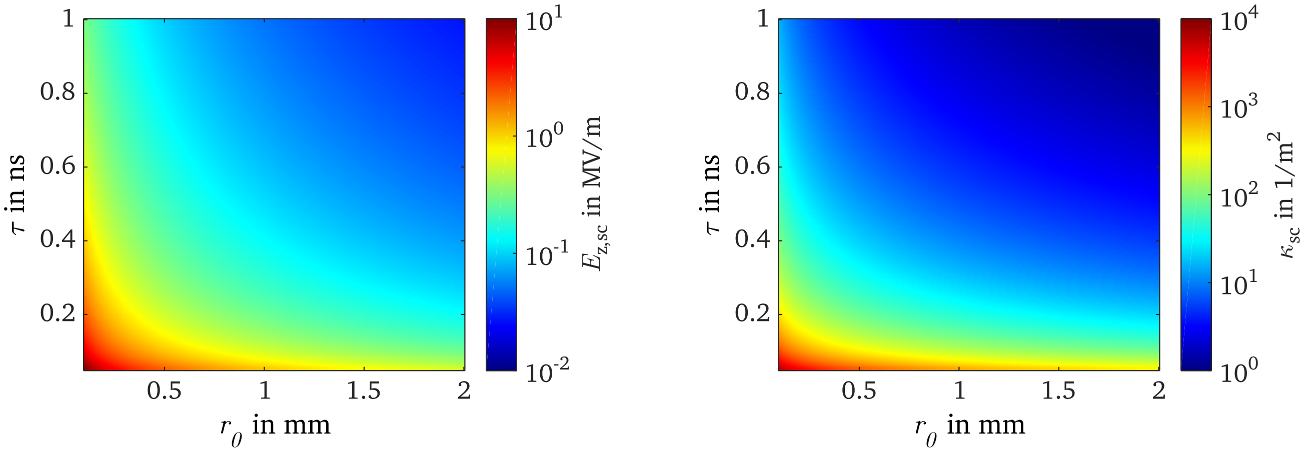

Fig. 7.15: Electric field $E_{z,\mathrm{sc}}$ and defocusing strength κ_{sc} caused by space charge effects for different beam radii r_0 and bunch lengths τ.

For the proton beam parameters achieved in the simulation $(r_0 = 0.65\,\mathrm{mm},\ \tau = 60\,\mathrm{ps})$ the electric field strength for the particles that are on axis and at the edge of the beam is 1.9 MV m^{-1}. However, at a distance of 30 mm to the focal spot the beam radius is already 1.5 mm (see Fig. 7.1) and therefore the electric field at this position is only 48 kV m^{-1} (assuming a constant temporal bunch width over this distance). The electric field $E_{z,\mathrm{sc}}$ can therefore only explain a change in the energy of the particles in the immediate vicinity of the focal point, but a change in their flight time from the origin to the focal point due to space charge effects can be excluded. In the following, it will also be investigated whether transverse space charge effects could have had an influence on the beam dynamics.

Since the value of the focusing strength has not been used in this work so far, the focusing strength of the second solenoid magnet in the experiment shall be given here as a comparison. By using the Equations 4.8 and 4.33 as well as $\kappa_{\mathrm{sol}} = \frac{1}{fL_{\mathrm{sol}}}$ [Hinterberger, 2008], one obtains $\kappa_{\mathrm{sol}}(6.75\,\mathrm{kA}) = 144\,\mathrm{m}^{-2}$ for protons with an energy of 7.7 MeV which would thus correspond to the green color in the right image of Fig. 7.15. For the proton beam parameters achieved in the simulation $(r_0 = 0.65\,\mathrm{mm},\ \tau = 60\,\mathrm{ps})$ the defocusing strength κ_{sc} is 283 m^{-2}, and it seems therefore unrealistic that a focal spot size of 0.65 mm is achievable for 7.29×10^8 protons with 7.7 MeV and a temporal width of 60 ps. On the other hand, for the measured proton beam parameters $(r_0 = 0.69\,\mathrm{mm},\ \tau = 742\,\mathrm{ps})$ the defocusing strength κ_{sc} is only 10 m^{-2}. So only if the actual temporal bunch widths were shorter than the diamond detector signals it is possible that space charge effects had a significant influence on the transverse beam dynamics in the experiment and thus led to an enlargement of the focal spot. This implies that for the uncompressed proton beam, a smaller focal spot size should be possible. The focal spot of the transported, uncompressed bunch during the beamline adjustment was actually smaller, which can be seen in Fig 7.16. However, the simulations also showed that the temporal compression slightly increases the focal spot size (see Fig. 7.6). Also, a direct comparison of Fig. 7.16 and Fig. 7.12 should be taken with caution since during the beamline alignment the energy of the PHELIX laser is reduced to increase the shooting rate. For this reason, the maximum energy of the TNSA spectrum is lower and therefore the initial maximum divergence angle of protons with 7.7 MeV is smaller. According to Table 4.2 this results in a smaller emittance of the beam which could also be the reason for the smaller focal spot.

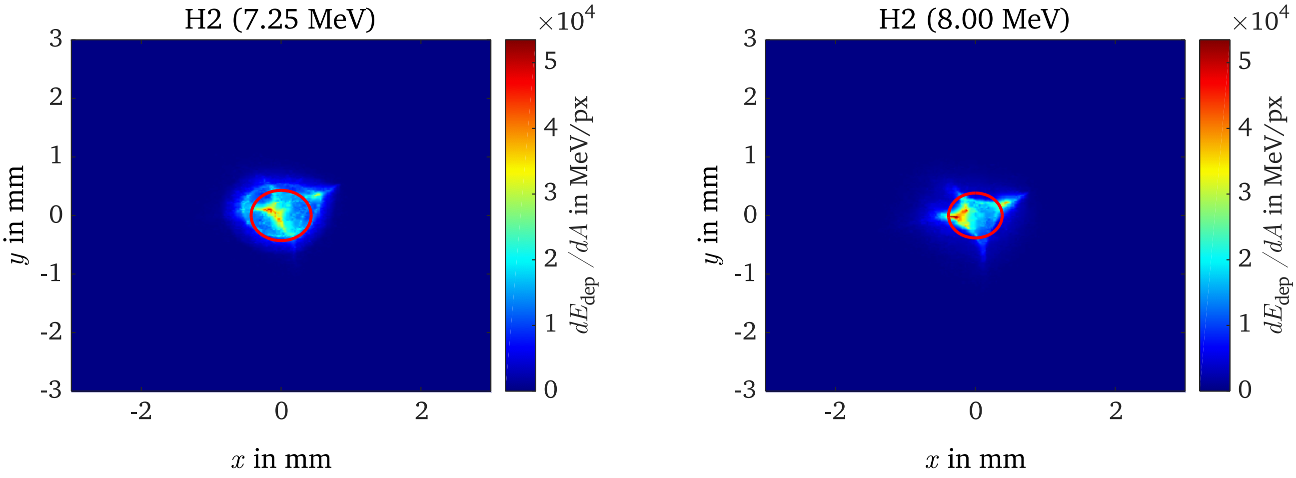

Fig. 7.16: Deposited energy of the uncompressed proton beam during the adjustment of the second solenoid. The red circles enclose 50 % of the total deposited energy. In the left image the circle has a diameter of 0.86 mm and in the right image the diameter is 0.76 mm.

From this discussion it can be concluded that the space charge effects had little, if any, influence on the beam dynamics.

Initial emittance of the TNSA-generated ion beam

As discussed in Section 2.3 and in Appendix A.1, according to [Cowan et al., 2004] the transverse and the longitudinal emittance of the TNSA-generated ion beam are very low and should therefore not affect the resulting beam parameters at the LIGHT beamline. However, measuring the longitudinal emittance with the LIGHT beamline would definitely be an option for a future experimental campaign if saturation effects of the diamond detector cannot explain the discrepancies between the temporal bunch width in the simulations and the measurements.

Radial dependence of the energy transfer of the RF cavity

A dependency of the energy transfer of the RF cavity on the radial distance of the particles would limit the temporal bunch width that can be achieved by the temporal compression. In Appendix A.2 the spatial distribution of the electric field in an acceleration gap is determined for a very simplified, stationary charge distribution. The radial dependency of the energy transfer that resulted from this electric field distribution does not change the resulting temporal bunch width in the simulation. However, the determination of a realistic electric field distribution was not carried out within the scope of this work and a more detailed investigation of this point is therefore still pending.

Conclusion

In this section, the measured and the simulated parameters of the focused and temporally compressed proton bunch at the LIGHT beamline were compared. Thereby, a good agreement of all beam parameters was found except for the temporal bunch width. The scattering foil, space charge effects, incorrect settings of the RF cavity, the initial emittance of the proton beam and a radial dependence of the energy transfer of the RF cavity could be excluded as the cause of this deviation. Therefore, saturation effects in the diamond detector used in the measurements are the most plausible explanation of this deviation for the time being. However, in order to prove this with certainty, further investigations are required.

This concludes the investigations of this thesis with respect to proton beam shaping. In the next chapter, the implementation and results of an experimental campaign are presented in which carbon ions have been shaped for future stopping power experiments at GSI.

8. Generating suitable ion bunches for stopping power experiments

The last application that will be investigated in this thesis is the generation of a suitable ion bunch for stopping power experiments. Therefore, in the beginning of this chapter an introduction to this application is given, the beam parameter requirements are defined and a suitable setup for the LIGHT beamline is determined. After that, the results of a preparatory beamtime in which the discussed setup is used are presented and compared with simulations. Finally, the obtained beam parameters are used to make predictions for the planned stopping power experiments.

8.1. Stopping power experiments with the LIGHT beamline

The stopping power of ions in dense, highly-ionized matter is one of the key topics in Inertial Confinement Fusion (ICF), since modelling the process in order to optimize the net energy gain requires a precise understanding of the interaction between the Deuterium-Tritium (DT) plasma and the α-particles [Zylstra and Hurricane, 2019; Hurricane et al., 2019]. An approved and universally applicable ion stopping theory could be even more valuable in ICF schemes like heavy-ion fusion [Callahan-Miller and Tabak, 2000] [Hofmann, 2018] or ion-driven fast ignition [Roth et al., 2001; Fernandez et al., 2014], as well as in other partially related research areas like isochoric heating [Sharkov et al., 2018; McGuffey et al., 2020] and plasma proton radiography [MacKinnon et al., 2006; Volpe et al., 2011]. The validation of ion stopping theories requires conclusive experimental data and these are very sparse, especially in the regime, in which the velocities of the probing ions and the plasma electrons or ions are approximately equal [Cayzac et al., 2017; Apiñaniz et al., 2021]. This is because suitable laser-generated plasmas in these measurements are typically very small and highly transient, leading to great demands on the equipment of the experimental area and, in particular, on the plasma probing ion beam.

This is also the cause of the rather large uncertainties in the few experiments reported. For example, in a previous experiment at GSI ([Cayzac et al., 2017]), the micro bunches of the UNILAC were used as the probing ions which had a temporal width of 5.5 ns in this experiment. Since during this 5.5 ns the relevant plasma parameter for the stopping power $(T_\mathrm{e}, n_\mathrm{e}, \bar{Z}_\mathrm{plasma})$ change significantly, the time averaging over the plasma parameters caused rather large uncertainties in the theories, which are compared to the experimental data. Also, the signal-to-noise ratio was relatively high due to the low particle flux in a single micro bunch $(\approx 10^4)$ of the UNILAC. Because of that, it was not possible to use a longer flight distance in the ToF measurement to increase the accuracy of the measured stopping power. Therefore, one goal of this work was to generate an ion beam with the LIGHT beamline for the plasma probing, with a higher particle flux and a shorter temporal width than the UNILAC. In addition, the energy spread of the bunch should be small, and its velocity v_p should be matched to the thermal velocity of the electrons v_th^e in the laser generated plasma

$$v_\mathrm{p} \approx v_\mathrm{th}^\mathrm{e} = \sqrt{\frac{3k_\mathrm{B}T_\mathrm{e}}{m_\mathrm{e}}}, \tag{8.1}$$

since in this regime the stopping power peaks and a strong beam-plasma coupling is achieved, which increases the importance of strong non-perturbative collisions [Cayzac et al., 2017]. Therefore, the existing theories differ the most, thus reducing the measurement accuracy requirements for theory benchmarking [Cayzac et al., 2017]. The extent to which this condition can be met depends primarily on the equipment of the experimental area. For example, the size and temperature of the plasma in stopping power experiments is mainly limited by the laser used to generate the plasma. Thereby it should be noted that although the plasma temperature can be increased by a smaller laser focus, in the case of a flat foil plasma target this decreases the range in which the plasma parameters are spatially homogeneous and the timescale on which the plasma can be investigated. Therefore, for the first stopping power experiments with the LIGHT beamline, the same plasma parameters as in [Cayzac et al., 2017] are chosen ($n_e \approx 5 \times 10^{20}\,\mathrm{cm}^{-3}, T_\mathrm{e} \approx 150\,\mathrm{eV}$), which requires a laser pulse with an energy of 60 J, a wavelength of approximately 527 nm and a pulse length of 7 ns. At the experimental area Z6, two high power laser systems are available, the PHELIX and the *nhelix* laser. Since the PHELIX laser will already be used for the ion acceleration at the LIGHT beamline, the plasma heating will be done by the *nhelix* laser. In order to achieve the required laser pulse parameters with *nhelix*, the system was redesigned as part of this work and is currently under reconstruction.

According to the Equation 8.1, the corresponding energy per mass of the probe ions for an electron plasma temperature of $T_\mathrm{e} \approx 150\,\mathrm{eV}$ is about 0.5 MeV u^{-1}. This is a much lower energy per mass than usually targeted at the LIGHT beamline, especially for protons. In addition, the effective voltage of the RF cavity has a minimum at an energy per mass of 0.5 MeV u^{-1} (see Fig. 5.3). Since the generation and transport of carbon ions with C^{4+} has also been shown to work reliably in previous experiments [Ding, 2018], in this thesis the generation of C^{4+} carbon bunches with 7.2 MeV (0.6 MeV u^{-1}) was targeted. Recently, however, the first experiments with protons in the suitable energy range have also been carried out.

The setup of the LIGHT beamline with the appropriate distances for handling C^{4+} with 7.2 MeV for the plasma probing is shown in Fig 8.1 and will be discussed in the following.

Distance	$d_\mathrm{sol,1}$	$d_\mathrm{sol,2}$	d_end	$d_\mathrm{cav,1}$	$d_\mathrm{cav,2}$
Length	40 mm	2200 mm	3225 mm	1225 mm	2000 mm

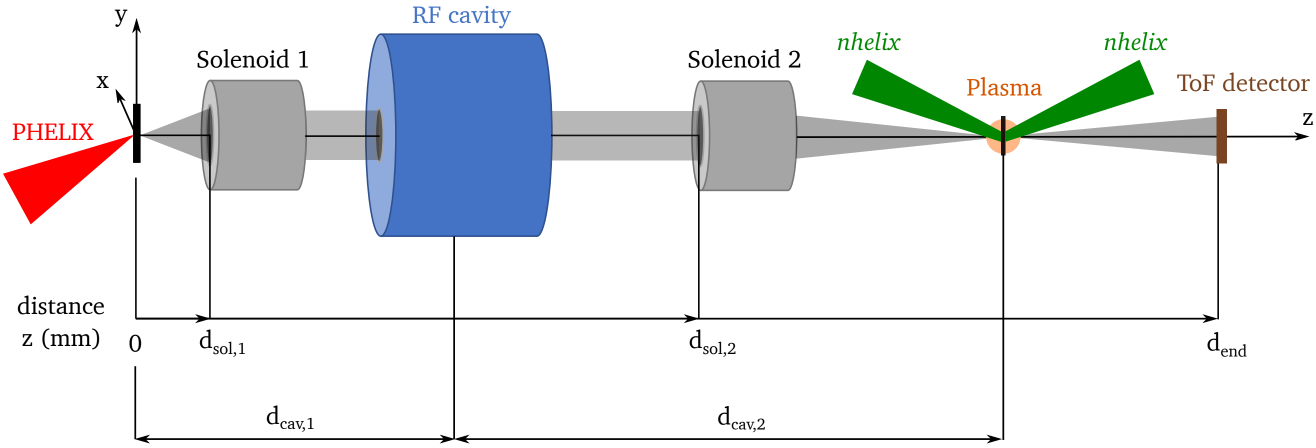

Fig. 8.1: Planned setup for future stopping power experiments at the experimental area Z6 of GSI, in which the plasma probing ion beam is provided by the LIGHT beamline.

The position of the RF cavity is considered first. As discussed in Section 5.3, the energy spread $\Delta E_{\text{linear}}/E$ that can be temporally compressed increases for a shorter distance between the RF cavity and the origin of the beam $d_{\text{cav,1}}$. The distance should therefore be as short as possible. The minimal distance is limited by the maximum RF cavity voltage and the geometrical constraints at the experimental area Z6. For C^{4+} with about 0.5 MeV u^{-1} the required energy transfer of the RF cavity for the temporal compression is in principle relatively low, but since the effective voltage of the RF cavity has a minimum at an energy per mass of 0.5 MeV u^{-1} (see Fig. 5.3) the targeted energy per mass is adapted to 0.6 MeV u^{-1}. Therefore, the velocity of the ions is still very close to the thermal velocity of the plasma electrons and the distance $d_{\text{cav,1}}$ can be chosen as small as it is geometrically possible (1.225 m). The required cavity voltage for the temporal compression U_{tcomp} also depends on the distance between the RF cavity and the plasma target $d_{\text{cav,2}}$ (see Section 5.3). However, this distance does not have a great effect on the resulting beam parameters. Therefore, it is set to 2 m which results in an RF cavity voltage U_{tcomp} of 0.4 MV and thus should favor a stable operation of the RF cavity.

Now the positions for the solenoid magnets are also taken into account. In order to increase the capture efficiency, the first solenoid should be as close to the TNSA target as possible. At the LIGHT beamline, this distance is typically 40 mm, allowing a motorized stage with a lens and a mirror to travel between the TNSA target and the solenoid before each shot to adjust the PHELIX laser (see Focus diagnostic in Fig. 7.7). The ideal position of the second solenoid depends on the size of the plasma target that will be probed by the ion beam. Due to the limited energy of the heating laser (*nhelix*), the region in which the plasma parameters are spatially homogeneous will only be $\sim$ 0.5 mm [Cayzac et al., 2017]. Therefore, the second solenoid has to focus the carbon beam on the plasma to get a sufficient amount of carbon ions to pass through this region. Since the focal spot size increases with the focal length of the solenoid (see Equation 4.31 in Section 4.2), also the distance of the second solenoid to the plasma target should be as short as possible. Unfortunately, the smallest possible distance is about 1 m because otherwise the solenoid would block the beam of the heating laser (see Fig. 8.1).

In the next section simulations of the carbon beam shaping with the discussed setup are presented which will then be compared to experimental results in Section 8.3.

8.2. Simulation studies on the carbon beam shaping

In the following, the reconstruction of a TNSA-generated carbon beam is explained first and then the simulation studies on the carbon beam shaping for the stopping power experiments are presented. In these simulations, the field maps determined with the realistic coil are used for the solenoids (see Section 4.4.3).

8.2.1. Reconstruction of a TNSA-generated carbon beam

The reconstruction of the TNSA-generated carbon beam in the simulation requires the parameters k_B, E_cut, a_2, a_1 and a_0 for each charge state, which in case of carbon ions in the lower MeV-range cannot be measured by RIS (see Section 2.2). Therefore, the parameter k_B and E_cut are taken from the energy spectra shown in Fig. 8.2, which were determined from Thomson parabola measurements in [Ding, 2018].

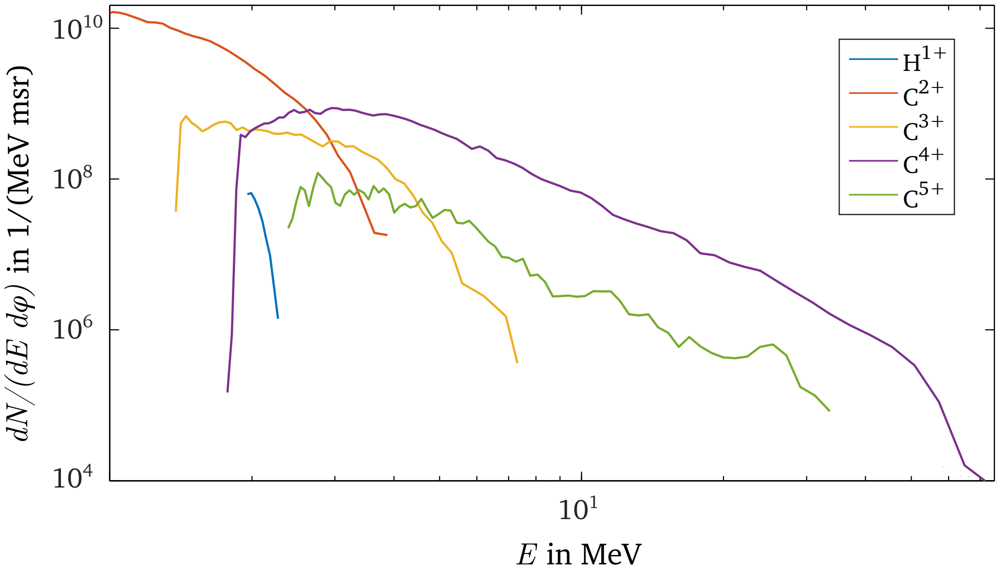

Fig. 8.2: Energy spectra of the TNSA-generated carbon beam at the origin of the LIGHT beamline of GSI [Ding, 2018].

Since these measurements do not provide the parameters a_2, a_1 and a_0 it is assumed, that the maximum and minimum direction divergence are with $\theta_\mathrm{max} = 25°$ and $\theta_\mathrm{min} = 5°$ equal for each charge state, as well as $\theta(E_\mathrm{min}) = \theta_\mathrm{max}$ and $\theta(E_\mathrm{cut}) = \theta_\mathrm{min}$ with a linear dependency on the ion energy. This results in

$$a_2 = 0, \quad a_1 = \frac{\theta_\mathrm{max} - \theta_\mathrm{min}}{E_\mathrm{min} - E_\mathrm{cut}}, \quad a_0 = \theta_\mathrm{max} - a_1 \cdot E_\mathrm{min}. \tag{8.2}$$

The values determined in this way are listed in Table 8.1 and the generated spectra are shown in Fig. 8.3. Thereby, some slight adoptions are made. In the Thomson parabola measurements in [Ding et al., 2018] the acceleration of protons were suppressed. However, in the simulation protons and carbon ions can be considered simultaneously and therefore the parameters of the initial proton beam were chosen as in the previous chapter. In addition, the number of C^{2+} was reduced in order to save computing power.
In the following, the transport of the carbon beam is now considered.

Table 8.1: Parameters that were used to generate a beam with proton and carbon ions in the simulations of this section.

Ions	N	$k_{\mathrm{B}}T$	E_{min}	E_{max}	E_{cut}	a_2	a_1	a_0
H^{1+}	1×10^6	6 MeV	1 MeV	28 MeV	28 MeV	-0.04°/MeV^2	0.41°/MeV	26.47°
C^{2+}	2×10^6	0.5 MeV	0.75 MeV	3.75 MeV	3.75 MeV	0°/MeV^2	-5.80°/MeV	26.74°
C^{3+}	2×10^6	1 MeV	0.75 MeV	6 MeV	7.5 MeV	0°/MeV^2	-3.33°/MeV	30.00°
C^{4+}	3×10^6	6 MeV	2 MeV	60 MeV	60 MeV	0°/MeV^2	-0.34°/MeV	25.68°
C^{5+}	3×10^5	6 MeV	3 MeV	30 MeV	30 MeV	0°/MeV^2	-0.74°/MeV	27.22°

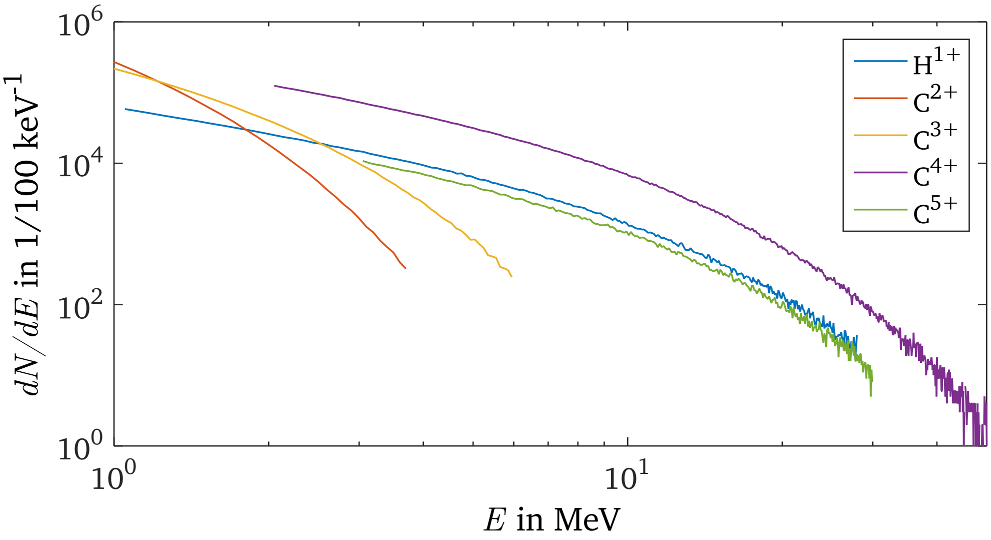

Fig. 8.3: Initial spectra of the carbon beam generated by the parameters shown in Table 8.1.

8.2.2. Transport of laser-accelerated carbon beams

As a first step, the required current of the first solenoid for transporting the C^{4+} with 7.2 MeV is estimated. Therefore, it is assumed that the focal length f of the solenoid magnet is given by Equation 4.8 for each particle and that the magnetic field B_0 is proportional to the current that is supplied to the solenoid magnet (see Equation 4.33). This leads to the following relation:

$$f^{-1} \propto (qB_0/p)^2 \propto (qI/p)^2. \tag{8.3}$$

The fact that the focal length must be identical for all simultaneously transported particles ($f_1 = f_2$) then leads to ($\gamma \approx 1 \rightarrow p = \sqrt{2mE}$):

$$I_2 = \frac{q_1}{q_2}\sqrt{\frac{m_2}{m_1}\frac{E_2}{E_1}} \cdot I_1. \tag{8.4}$$

From Section 4.4 it is known, that the current required to transport protons with 8.3 MeV is $I = 8.5$ kA. Using this as a reference, the required current for transporting C^{4+} with 7.2 MeV results in $I = 7$ kA. The spectra of the transported carbon beam for this current is shown in Fig. 8.4 (behind the second solenoid). Thereby, the initial carbon beam parameters and the setup of the LIGHT beamline are as described in the previous subsections and the RF cavity as well as the second solenoid are only implemented as drift tubes.

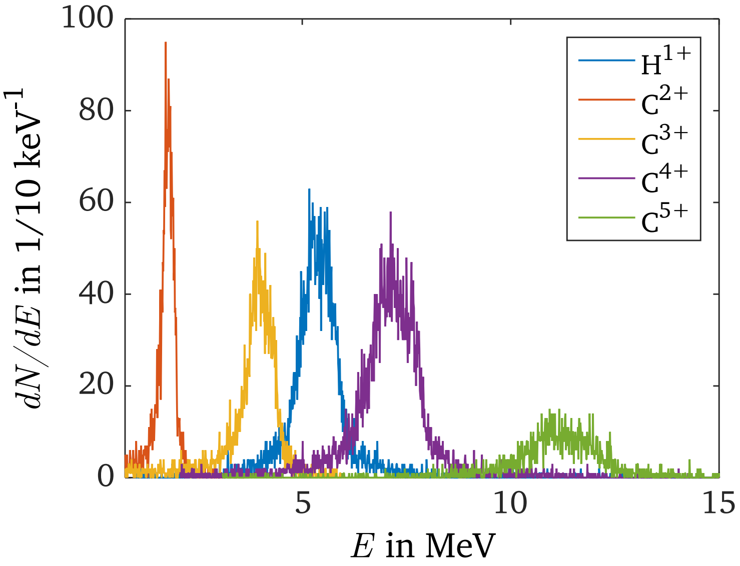

Fig. 8.4: Simulated spectra of the protons and carbon ions that are simultaneously transported through the LIGHT beamline. Thereby, a current of 7 kA is supplied to the first solenoid and the initial beam parameters shown in Table 8.1 are used.

Setting $I_1 = I_2$ in Equation 8.4 results in the following relation between E_1 and E_2:

$$E_2 = \left(\frac{q_2}{q_1}\right)^2 \frac{m_1}{m_2} \cdot E_1, \tag{8.5}$$

which is given for the peak energies in Fig. 8.4. In the next subsection, the focusing of this beam with the second solenoid is investigated.

8.2.3. Transverse focusing of the transported carbon beams

For the simulation of this subsection, the same simulation parameters as in the previous subsection are used, but the second solenoid is simultaneously supplied with a current of 2.95 kA. This current was gradually adjusted in the simulation until the beam size had a minimum at the distance d_{end}. The beam profile at this position (3225 mm from the origin of the beamline) is shown in the left image of Fig. 8.5 in the x-y plane.

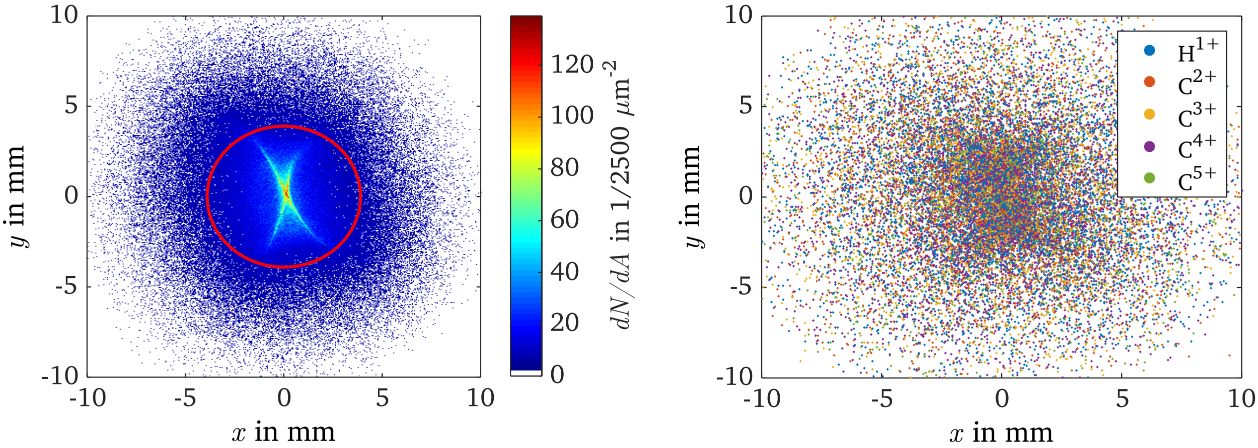

Fig. 8.5: In the left image the number of particles per area of the carbon beam at the end of the LIGHT beamline is shown, and the red circle encloses 50 % of the particles. The color of the particles in the right picture corresponds to their charge state and species.

The red circle in this image encloses 50 % of the particles and had a radius of 3.9 mm. The focal spot is therefore almost eight times larger than the focal spot of the proton beam shown in Section 7.2. The reason for this is the longer focal length of the second solenoid. If the cardinal points are assumed to be in the center of the solenoid, in Section 7.2 the focal length $f_{\text{sol,2}}$ is 175 mm whereas for the setup used in this subsection it is 875 mm. According to Equation 4.31 the focal spot size should therefore be five times larger. The deviation indicates that the cardinal points are not exactly in the center of the solenoid. Calculating the focal length with Equation 4.8 supports this assumption ($f = 86.3$ mm for $I = 7$ kA, $E = 7.2$ MeV, $q = 4$ e and $m = 12$ u).

In the right image of Fig. 8.5 the distribution of the charge state of the particles is shown in the x-y plane which does not reveal any correlations between the charge states and the positions of the particles. This is in accordance to Lorentz's equation, which states that non-relativistic ions ($\gamma \approx 1$) with the same ratio of charge and momentum q/p behave exactly the same in a magnetic field.

In the last subsection of this section the C^{4+} ions with an energy of 7.2 MeV are temporally compressed to increase the particle flux and minimize the temporal width of the beam at the point where the plasma will be generated in future stopping power experiments.

8.2.4. Temporal compression of carbon ions

For the temporal compression, the RF cavity parameters are gradually adjusted until the carbon bunch with a mean energy of 7.2 MeV has its minimum temporal width at the distance d_{end} (3225 mm from the TNSA target). Thereby, the optimal RF cavity voltage was found to be 0.43 MV. The C^{4+} ions of the resulting beam in the E-t phase space are shown in the upper image of Fig. 8.6 and in the lower picture, the time of flight of the particles is illustrated as a histogram.

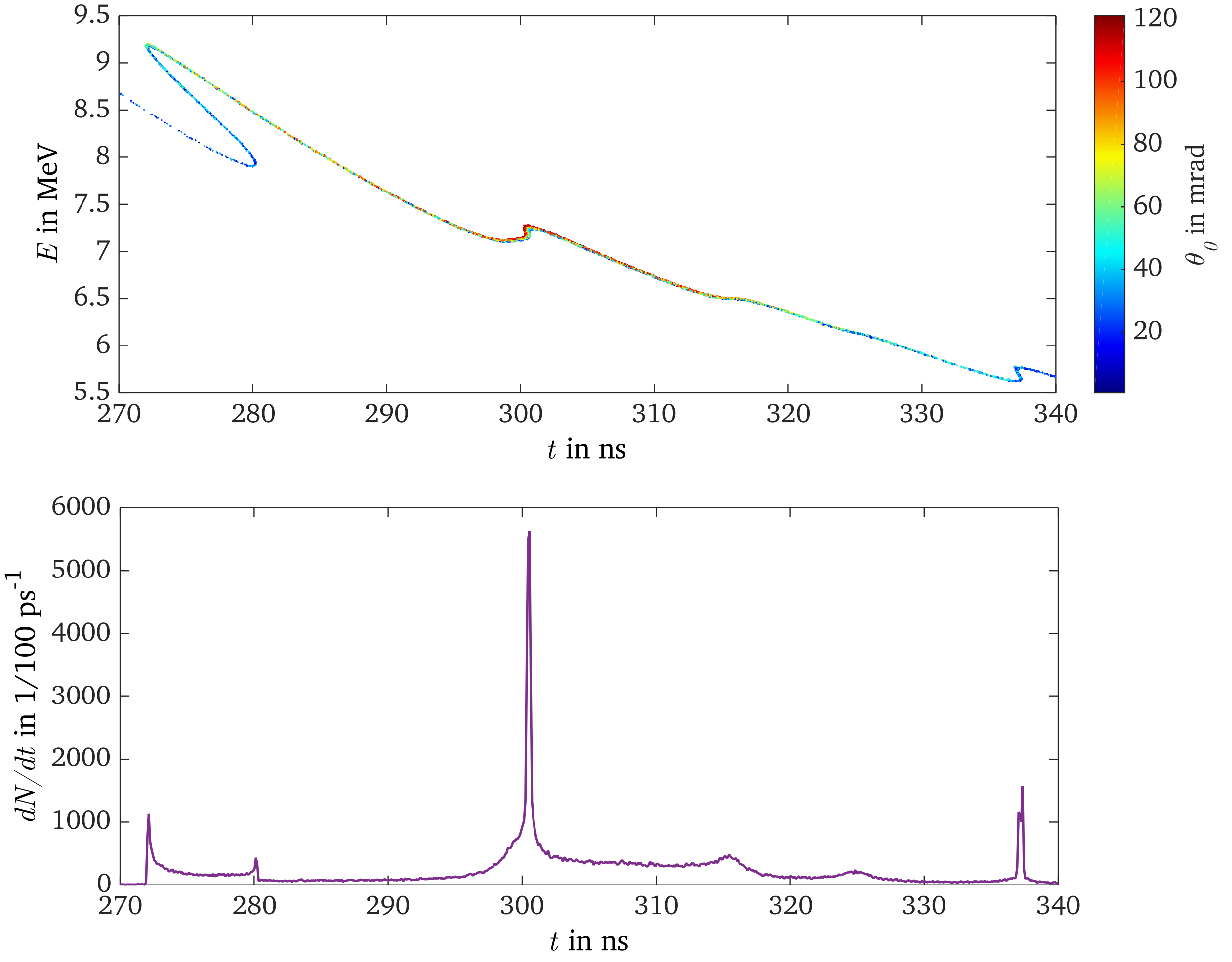

Fig. 8.6: In the upper image, the C^{4+} ions of the transported carbon beam are shown in the E-t phase space at the distance d_{end} (3225 mm from the TNSA target) for an RF cavity voltage of 0.43 MV. Thereby, the color of the particles corresponds to their initial divergence angle θ_0. In the lower picture the time of flight of the particles are illustrated as a histogram.

It can be seen, that not all transported C^{4+} can be compressed to a single bunch, which is due to the long temporal width of the transported C^{4+} within the RF cavity. In this case the temporal width of the transported C^{4+} within the RF cavity is even longer than twice the period duration $2T$ which leads to multiple peaks of the C^{4+} at the illustrated distance d_{end}. Since the relative energy transfer of the RF cavity to the C^{4+} ions with a mean energy of 5.7 MeV and 8.5 MeV is higher (according to Equation 5.14), they have already reached their minimum temporal width at a shorter distance. The additional flight distance then leads to an u-shaped temporal profile of the bunch. For the future stopping power experiments, only the temporal compressed carbon ions with an energy of about 7.2 MeV are relevant. The temporal width of this bunch is 300 ps in the simulation, which is mainly caused by the longer path lengths of particles with higher initial divergence angles. Therefore, particles with the same energy reach the RF cavity at slightly different times and do not experience the same electric field. For the temporal compression of the carbon ions with 7.2 MeV this has a greater effect than for protons with 7.7 MeV (see Section 7.2) due to the lower velocities of the particles.

The most important parameters of the temporal compressed and focused C^{4+} beam in the simulation are summarized in Table 8.2.

Table 8.2: Parameters of the temporal compressed and focused C^{4+} beam that have been determined with the simulations shown in this section.

Parameter	Value
Mean energy	7.2 MeV
Energy spread (full width)	1.94 %
Temporal bunch width	300 ps
Focal spot size (radius, only C^{4+} ions)	3.44 mm

8.3. Experimental results on the carbon beam shaping

In this section the results of a preparatory beamtime for the planned stopping power experiments, which was performed during this work, will be presented and compared to the simulations of the previous section.

8.3.1. Setup for the generation and characterization of the carbon beam

The setup of the LIGHT beamline used in the preparatory beamtime is shown in Fig. 8.7 together with the used diagnostics. The distances are chosen as discussed in the first section of this chapter so that the setup of the LIGHT beamline corresponds to the setup in future stopping power experiments.

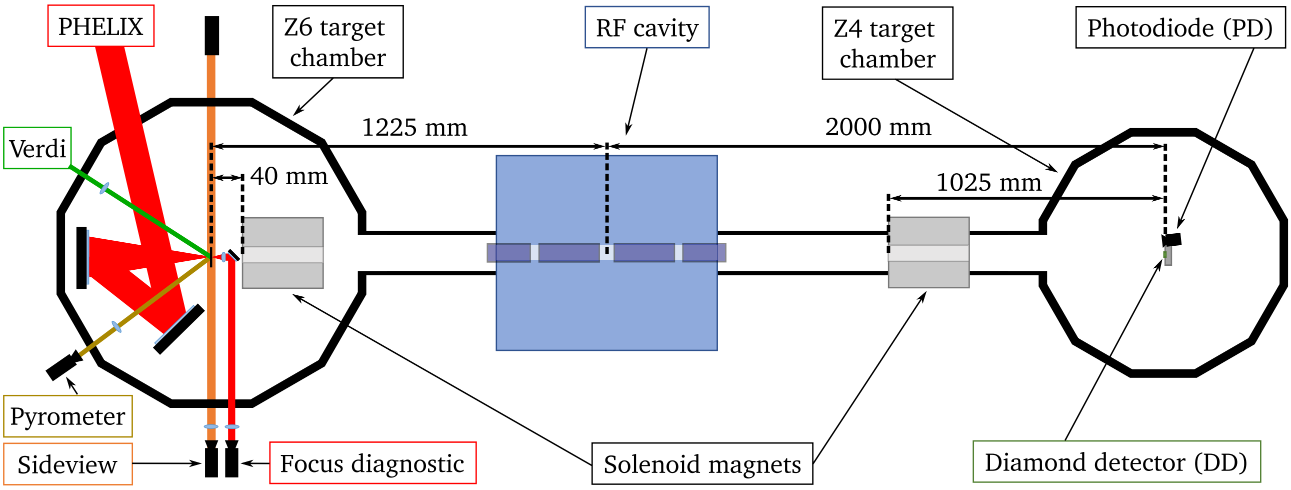

Fig. 8.7: Schematic setup of the LIGHT beamline during a preparatory beamtime for stopping power experiments in January 2021.

Under normal conditions, the hydrogen of the contamination layer on the targets surface is accelerated most efficiently by the TNSA mechanism due to their highest charge to mass ratio. For this reason, the contamination layer has to be removed in order to increase the acceleration efficiency of other ion species [Hegelich et al., 2005; Ding, 2018]. In this work, the contamination layer is evaporated by increasing the temperature of the target well above 1000 °C. Therefore, 10 µm thick tungsten foils with a 0.9 µm carbon coating on its rear side were used as the TNSA target and their temperature were increased by either Ohmic heating or by a heating laser (Verdi G 10 manufactured by the company *Coherent, Inc.*). Thereby, a pyrometer measures the temperature of the target to ensure that the heating is sufficient and the targeted temperature is reached. During the experiment it turned out that the Ohmic heating was much more reliable since in this case the whole target is heated homogeneously whereas in the case of the laser heating it was difficult to verify if the relevant spot was heated. In addition, the mechanical stress from the local heating of the laser caused the target to break in the worst case, since it was kept under tension by the target holder in order to prevent strong deformation due to thermal expansion.
The setup of the other diagnostics are identical as in the experiment that was presented in the last chapter. In the next subsection, the carbon beam transport through the LIGHT beamline is described.

8.3.2. Transport of laser-accelerated carbon beams

Since the RIS cannot distinguish between different carbon ion energies and species (see Section 2.2), the solenoid magnets were set up to transport 5.4 MeV protons, which according to Equation 8.5 and the simulations in Subsection 8.2.2 leads to simultaneous transport of C^{+4} ions with 7.2 MeV. After minimizing the focal spot size in the center of the Z4 target chamber by a stepwise adjustment of the supplied current, everything was set up for the ToF measurements, i.e., the diamond detector was placed in the focal spot and a 2 µm thick Mylar foil was placed 300 mm in front of the diamond detector to eliminate the beam filamentation. According to the SRIM code this leads to a mean scattering angle of 13 mrad for C^{+4} ions with 7.2 MeV which corresponds to a location deviation of 3.9 mm over the 300 mm distance (the radius of the focal spot at this position was about 3.5 mm). As described in the beamtime that was presented in the previous chapter, the photodiode next to the diamond detector measures the electromagnetic radiation of the interaction between the TNSA target and the PHELIX laser. The rising edge of the photodiode signal is then used to determine the starting time of the transported particles. A result of the ToF measurement with this setup is shown in Fig. 8.8 along with the corresponding time of flight of the carbon ions in the simulations of Section 8.2.2.

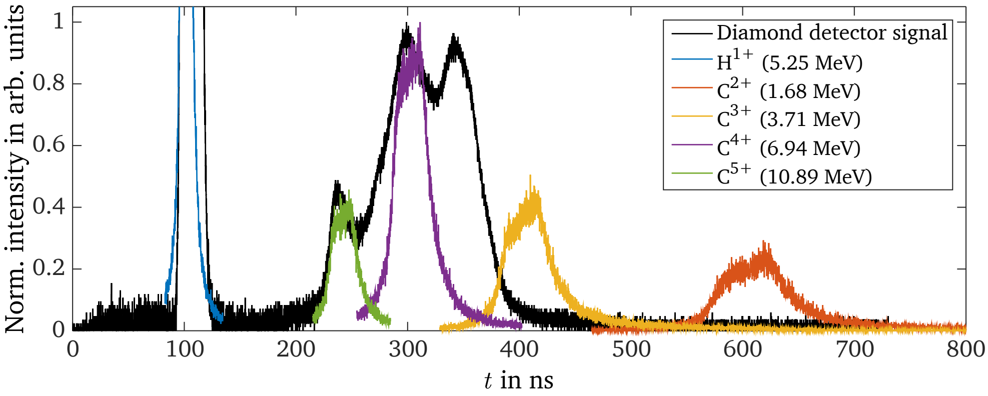

Fig. 8.8: Diamond detector signal that corresponds to the time of flight of the ions that are transported through the LIGHT beamline as well as the time of flight of the transported carbon ions in the simulations.

As can be seen, the first three peaks of the diamond detector signal can be assigned to H^{+1}, C^{+5} and the C^{+4} ions, while the signal of the diamond detector shows no peak at the time when the C^{+3} and C^{+2} ions should arrive. In addition, the diamond detector signal has a peak at 340 ns which can not assigned to transported protons or carbon ions. Based on the high signal for protons, it can be concluded that the contamination layer on the rear side of the target surface was not completely evaporated in this shot. Since the contamination layer typically contains hydrogen, carbon and oxygen, it is possible that the peak in the signal at 340 ns is caused by transported oxygen ions. The Table 8.3 gives an overview of the oxygen ions that are transported simultaneously, provided they have been accelerated by the TNSA mechanism.

Table 8.3: Energy E and ToF t of oxygen ions that are transported simultaneously with 5.4 MeV protons through the LIGHT beamline according to the Equation 8.5.

Ions	O^{+1}	O^{+2}	O^{+3}	O^{+4}	O^{+5}	O^{+6}	O^{+7}	O^{+8}
E	0.32 MeV	1.31 MeV	2.95 MeV	5.25 MeV	8.20 MeV	11.8 MeV	16.1 MeV	21.0 MeV
t	1612 ns	810 ns	540 ns	405 ns	324 ns	270 ns	232 ns	203 ns

Thus, it is very likely that the peak was caused by O^{+5} ions with 8.2 MeV which have a time of flight of 324 ns. However, it remains unclear why the carbon and oxygen ions with low energies, i.e. those with a small charge state are not observed in the ToF measurement. The Thomson parabola spectra measured in [Ding et al., 2018] (see Fig 8.2) show that these ions are generated and accelerated during the TNSA process and according to SRIM all carbon and oxygen ions with more than 1.5 MeV should be able to penetrate the 2 µm thick Mylar foil. So it remains to be clarified if space charge effects or a different response of the detector for low ion energies are the cause of these discrepancies. Since the simulated and measured flight times of the C^{4+} ions are showing a good agreement, it can be assumed that the space charge effects can be neglected for the C^{4+} ion transport. Therefore, in the following, the defocusing due to space charge effects for the C^{4+} ions is compared with those for the C^{3+} ions. For non-relativistic and nonneutralized beams $(\gamma \approx 1,\ f_\mathrm{e} \approx 0)$ Equation 3.32 can be simplified to

$$\kappa_\mathrm{sc} = \frac{qI}{2\pi\epsilon_0 m v^3 r_0^2} = \frac{Nq^2}{2\pi\epsilon_0 m v^3 r_0^2 \tau} \tag{8.6}$$

with $I = qN/\tau$ and τ being the temporal width of the bunch. According to the Thomson parabola spectra measured in [Ding et al., 2018] (see Fig 8.2) and the simulations, there should be twice as much C^{4+} ions than C^{3+} ions $(N_{4+} = 2N_{3+})$. By using the same radius r_0 and temporal width τ for both charge states, the ratio can be determined to $\kappa_\mathrm{sc}^{4+}/\kappa_\mathrm{sc}^{3+} = 1.32$. Thus, the space charge effects for C^{3+} ions are even smaller than for the C^{4+} ions and cannot explain the measurements. For this reason it is very likely that the diamond detector cannot detect ions with low energies.

However, since the transport of C^{4+} ions with 7.2 MeV was successful, the experiment could be continued without any restrictions and in the next subsection, the temporal compression of these ions will be presented.

8.3.3. Temporal compression of the transported carbon beam

For the temporal compression of the C^{4+} ions, the same setup as described in the last subsection was used and the RF cavity voltage and phase were adjusted stepwise. The two shortest diamond detector signals obtained by this procedure are shown in Fig. 8.9 (red and blue line) along with the diamond detector signal of the uncompressed beam (black line) and the temporally compressed beam from the simulation studies in Section 8.2.4 (purple line).

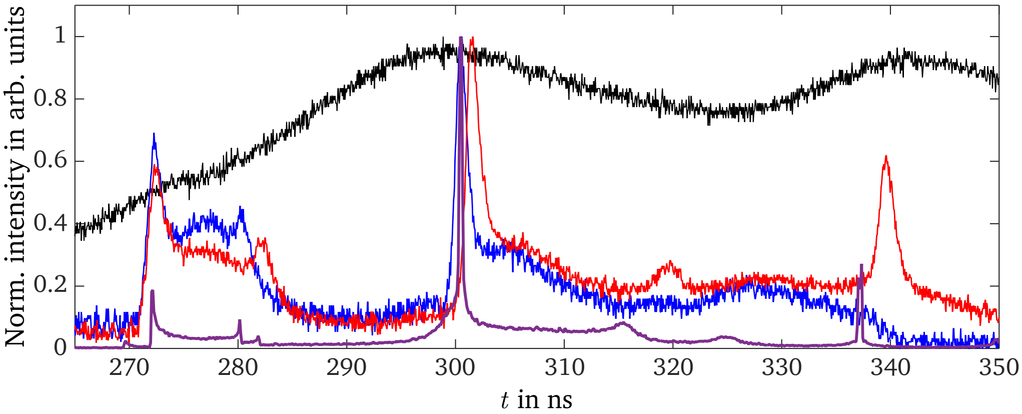

Fig. 8.9: Measured (red and blue line) and simulated (purple line) time of flight of the temporally compressed C^{4+} ions along with the measured time of flight of the uncompressed C^{4+} ions (black line).

As can be seen, the flight times and temporal distributions of the different carbon ion bunches show only slight deviations. However, the temporal widths of the temporal compressed C^{4+} bunch with 7.2 MeV is with 1.23 ns (FWHM of the blue line at $t \approx 300\,\mathrm{ns}$) four times larger than in the simulation. As discussed in Section 7.3, the reason for this deviation is probably due to

- Saturation effects in the diamond detector
- The scattering foil in the ToF measurements
- Space charge effects
- A non-negligible initial emittance of the TNSA-generated ion beam
- Radial dependence of the electric field within the gaps of the RF cavity

The first three points will be considered in more detail in the following. The fourth and the fifth point are partly considered in the appendix.

The energy deviation due to the scattering foil (2 µm Mylar) for 7.2 MeV carbon ions is 0.1 MeV (FWHM) which causes a time of flight deviation of 0.35 ns over the distance between the scattering foil and the diamond detector (300 mm). Thus, the scattering alone cannot explain the deviation between the measured and the simulated temporal bunch widths. To rule out space charge effects as a possible cause for the deviations, the number of carbon ions in the temporally compressed bunch as well as the size of the beam behind the second solenoid has to be known. These beam parameters are estimated with RIS measurements and simulation studies in the following subsection.

8.3.4. Estimation of the number of transported carbon ions

In Fig. 8.10 the deposited energy of the temporally compressed ion beam in the active layer of an RCF which was placed at the position of the diamond detector is shown.

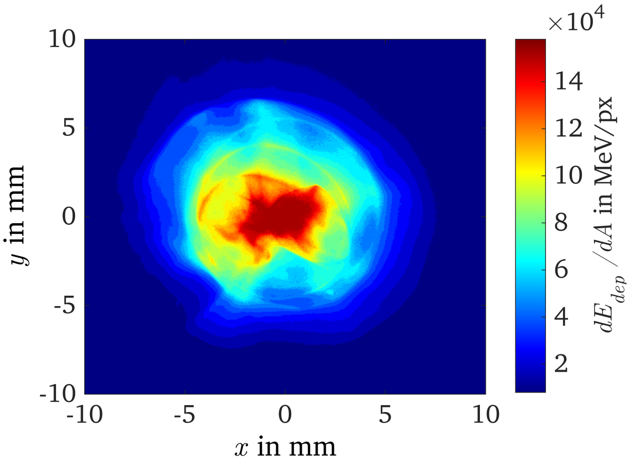

Fig. 8.10: Deposited energy of the transported ion beam at the position of the diamond detector. The smallest circle that contains 50 % of the deposited energy at this position has a radius of 3.77 mm.

The active layer of this RCF has a thickness of 10 µm. In the experiment, this active layer was facing the incident beam without any passive layer in front of it (also the Mylar scattering foil was removed). Thus, according to SRIM all transported carbon and oxygen ions up to an energy of 10 MeV were stopped within this layer and deposited their energy in it. Since even the carbon ions with the maximum measured and simulated energy of 12 MeV are depositing about 80 % of their energy in this active layer, it is assumed that the total deposited energy in the active layer corresponds to the energy of all transported carbon and oxygen ions (the deposited energy of the protons in this layer can be neglected). With this assumption, the number of particles of each energy can be determined for an arbitrary spectrum with relative particle numbers and a maximum energy of 12 MeV.

As discussed in Section 8.3.2 the diamond detector is probably not able to detect carbon ions with low energies. For this reason, is it not possible to determine the energy spectrum of the transported ion beam via the ToF measurements. Therefore, the energy spectrum of the transported carbon beam in the simulation is used for the estimation. In the simulation the transported beam contains 4.3×10^5 carbon ions in total of which 21 % are C^{2+}, 26 % are C^{3+}, 40 % are C^{4+} and 13 % are C^{5+}. Integrating over the entire energy spectrum results in an energy of 2.4×10^6 MeV. The total deposited energy in the active layer is $(2.0 \pm 0.6) \times 10^{10}$ MeV (the large uncertainty is due to a lack of calibration of the RCF used). Therefore, the number of carbon ions in the simulation would have to be 10^4 times higher to replicate the measurement. Assuming that the spectrum of the measured beam matches the spectrum in the simulation, the transported ion beam contains $(3.6 \pm 1.1) \times 10^9$ carbon ions of which then $(1.4 \pm 0.4) \times 10^9$ are C^{4+} ions. Furthermore, according to the simulation 14 % of the transported C^{4+} can be temporally compressed which would thus correspond to $(2.0 \pm 0.6) \times 10^8$ temporally compressed C^{4+} ions in the experiment.

With this estimation, the defocusing strength κ_{sc} and the longitudinal electric field $E_{z,\mathrm{sc}}$ caused by space charge effects can now be determined. For a beam radius of 3.5 mm and a temporal width of 0.3 ns this results in a κ_{sc} of $16\,\mathrm{m}^{-2}$ and a $E_{z,\mathrm{sc}}$ of $0.1\,\mathrm{MV\,m}^{-1}$. Space charge effects can therefore not explain the deviations between the measured and the simulated temporal width of the temporal compressed C^{4+} ions, and it is therefore most likely that the deviation is caused by saturation effects of the diamond detector.

In Table 8.4 the most important parameters of the temporal compressed carbon bunch are summarized. These are used in the following section to make some predictions for the planned stopping power experiments with the LIGHT beamline.

Table 8.4: Parameters of the temporal compressed carbon bunch that was generated during a preparatory beamtime for stopping power experiments with the LIGHT beamline. Also, the beam parameters from simulations are shown (see Section 8.2).

Parameter	Experiment	Simulation
Mean energy	(7.2 ± 0.2) MeV	7.2 MeV
Energy spread (full width of C^{4+} ions)	/	1.94 %
Temporal bunch width	(1.23 ± 0.04) ns	0.3 ns
Focal spot size (50 % of C ions)	(3.77 ± 0.02) mm	3.9 mm
Number of C^{4+} ions	(2.0 ± 0.6) × 10^8	14 % of the transported C^{4+} ions

8.4. Predictions for the planned stopping power experiments

As explained at the beginning of this chapter, the same plasma parameters which were used in the experiment published in [Cayzac et al., 2017] are targeted for the planned stopping power experiments with the LIGHT beamline. Therefore, in the following, the beam parameters of the experiment published in [Cayzac et al., 2017] are compared with the beam parameters that are expected in the planned experiment to illustrate the advantages.
In [Cayzac et al., 2017] the UNILAC of GSI was used as the ion source, which provided nitrogen ions with 3.6 MeV u^{-1}. In front of the plasma, this beam was then reduced in size by a pinhole with a diameter of 0.5 mm. Behind the pinhole, the beam was then degraded to (0.586 ± 0.016) MeV u^{-1} with a 41 µm thick carbon foil. After that, the resulting micro bunches of the nitrogen beam had about 10^3 ions with a Gaussian temporal profile and a FWHM of 5.5 ns. Since the plasma parameters are changing in nanoseconds in the experiment, the main uncertainties in the stopping power calculations are due to the time averaging over the 5.5 ns ion bunch. In addition, the low particle count resulted in a low signal-to-noise ratio, so the distance of the ToF measurement could not be increased further to increase the measurement accuracy. Therefore, the use of the temporally compressed C^{4+} ions of the LIGHT beamline for the plasma probing has several advantages:

- The temporal width of the C^{4+} ions is with 1.23 ns (FWHM) almost five times shorter than the temporal width of the micro bunches of the UNILAC.
- Even though the focal spot size is with 7.52 mm much higher than the 0.5 mm of the pinhole in front of the plasma, according to the simulation $(2.0 \pm 0.6) \times 10^6$ (1 %) of the ions would make it through the pinhole and therefore the LIGHT beamline provides three orders of magnitude more particles in a single bunch than the UNILAC.
- Since the C^{4+} bunch of LIGHT beamline does not have to be degraded by a scattering foil, their energy spread is with 2 % in the same order as the UNILAC bunches even though there are temporally compressed and not energetically compressed.

For these reasons, it is expected that the signal-to-noise ratio as well as the uncertainties in the theoretical stopping power calculations due to the time averaging can be significantly reduced by the performance of the stopping power experiments with the LIGHT beamline. With further investigations on the temporal compression as well as on the ion beam shaping through an appropriate pinhole placement, the temporal width of the C^{4+} bunches can probably even be further reduced. Moreover, with additional ion optics, the setup of the ToF measurement as well as the number of particles that penetrating the plasma can be improved.

This covers all the applications that were examined in the course of this work. In the final chapter, this work is now concluded with a summary and an outlook.

9. Summary and outlook

In the scope of this work, the shaping of laser-accelerated ion beams with the LIGHT beamline was extensively investigated by a comparison of theoretical predictions, numerical simulations, and experimental data. The goal of these investigations was to generate suitable ion beams with the LIGHT beamline for the applications that are currently pursued by the LIGHT collaboration.

In the first part of this thesis, the technologies used at the LIGHT beamline were explained and characterized step by step, namely

- the ion acceleration with the PHELIX laser via the TNSA mechanism,
- the transport of laser-accelerated ion beams with pulsed, high-field solenoid magnets and
- the longitudinal ion beam shaping with an RF cavity.

In this context, the capturing of the TNSA-generated ion beam with the solenoid magnet was investigated in particular detail, since it was expected that the ion beam quality would degrade in this process. Thereby, the chromatic aberration of the solenoid magnet was identified as the most crucial source of the transverse emittance growth (see Table 4.2).
Furthermore, the comparison of the beam profiles in the simulation for different, not perfectly symmetrical magnetic field distributions of the solenoid magnet revealed that the asymmetric magnetic field generated by the connecting cables of the solenoid magnet causes the cross-shaped beam profile in pulsed, high-field solenoid beamlines (see Fig. 4.13). However, when capturing an ion beam with a large initial divergence angle, which is typically the case at the LIGHT beamline, the relative emittance growth due to the magnetic field of the connecting cables is less than 10 % compared to the increase in emittance due to spherical and chromatic aberration (see Table 4.3).
After that, equations were derived which were used to determine the required RF cavity voltage as well as the optimal position of the RF cavity for the energetic and the temporal compression of the transported ion beam at the LIGHT beamline. These were then used to find the optimal setup of the LIGHT beamline for the applications that have been investigated in Part II of this thesis.

The injection of the proton beam into the heavy ion synchrotron SIS18 at GSI was evaluated first as a possible application in the future. Therefore, simulations were used to determine whether it is possible to provide a suitable ion beam with the LIGHT beamline that has a sufficient amount of particles within the acceptance range of the SIS18. This acceptance range is specified as follows [GSI, 2022]:

- Energy spread $\Delta E/E = 0.4\,\%$ (full width)
- Normalized horizontal emittance $\varepsilon^{2\sigma}_{n,xx'} = 3.12\,\mathrm{mm\,mrad}$
- Normalized vertical emittance $\varepsilon^{2\sigma}_{n,xx'} = 9.96\,\mathrm{mm\,mrad}$

According to the simulations, the components and laser parameters currently used at the LIGHT beamline can provide a proton beam with the following parameters:

- Mean energy $E = 11.4\,\text{MeV}$
- Energy spread $\Delta E/E = 0.21\,\%$ (FWHM)
- Normalized horizontal emittance $\varepsilon^{2\sigma}_{n,xx'} = 9.66\,\text{mm mrad}$ (within $\Delta E/E \pm 0.2\,\%$)
- Normalized vertical emittance $\varepsilon^{2\sigma}_{n,yy'} = 8.37\,\text{mm mrad}$ (within $\Delta E/E \pm 0.2\,\%$)
- Number of particles $N = 3.2 \times 10^8$ (within the SIS18 acceptance range)

Since the SIS18 can accommodate more than 10^{10} protons, also proposals have been made to increase the number of particles for this application. The most promising approach in this regard would be to increase the laser pulse energy for the TNSA mechanism at the origin of the LIGHT beamline.

The second application that had been addressed in this thesis was the generation of a high proton flux with the LIGHT beamline. Therefore, in an experimental campaign of this work, a proton beam with an energy of (7.72 ± 0.14) MeV was simultaneously focused and temporally compressed at the LIGHT beamline for the first time. The resulting beam parameters are shown in Table 9.1 along with the beam parameters predicted from numerical simulations.

Table 9.1: Resulting beam parameters of a temporal compressed and focused proton bunch at the LIGHT beamline. The corresponding measurements and simulations from which these values were determined have been performed in this work.

Parameter	Experiment	Simulation	Deviation
Number of protons	$(7.29 \pm 0.64) \times 10^8$	/	/
Mean energy	(7.72 ± 0.14) MeV	7.7 MeV	0.26 %
Energy spread (full width)	(4.91 ± 0.82) %	4.54 %	8.15 %
Temporal bunch width	(742 ± 40) ps	60 ps	> 10
Focal spot size that contains 50 % of protons	(1.38 ± 0.02) mm	1.3 mm	6.15 %

Due to the large deviation between the measured and simulated temporal bunch width (highlighted in yellow), possible causes for this discrepancy were considered. Most of these could be ruled out, so that saturation effects of the diamond detector used in the measurements are the most plausible explanation of this deviation for the time being.

The final application targeted in this work was the generation of a suitable ion beam for measuring the ion-stopping power of transient plasma targets with the LIGHT beamline. For this application C^{4+} ions with an **energy of (7.2 ± 0.2) MeV** were generated, transported, temporally compressed and focused with a setup of the LIGHT beamline that can be used for the stopping power experiments. The resulting bunch had a **focal spot size of (7.52 ± 0.02) mm** and a **temporal width of (1.23 ± 0.04) ns (FWHM)**. Furthermore, it could be estimated that **(2.0 ± 0.6) × 10^6 C^{4+} ions** of this bunch will penetrate the spatially homogeneous region of the plasma under investigation in the planned experiment, i.e., three orders of magnitude more particles than in previous measurements at GSI with a temporal bunch width comparatively almost five times shorter.

Outlook

With the beam parameters achieved in this work, the measurement of the ion-stopping power of dense, highly ionized plasma targets should lead to much lower measurement uncertainties than in previous stopping power experiments performed at GSI. Therefore, the next goal of the LIGHT collaboration is the conduction of a first stopping power experiment with the LIGHT beamline. For this experiment the same plasma parameters as in [Cayzac et al., 2017] are targeted $(n_\mathrm{e} \approx 5 \times 10^{20}\,\mathrm{cm}^{-3}, T_\mathrm{e} \approx 150\,\mathrm{eV})$, which requires a laser pulse with an energy of 60 J, a wavelength of approximately 527 nm and a pulse length of 7 ns. At the experimental area Z6, two high power laser systems are available, the PHELIX and the *nhelix* laser. Since the PHELIX laser will already be used for the ion acceleration at the LIGHT beamline, the plasma heating will be done by the *nhelix* laser. In order to achieve the required laser pulse parameters for plasma generation, the *nhelix* laser system has been redesigned as part of this work and is currently under reconstruction. After the completion of the upgraded *nhelix* system, the first stopping power experiments will be conducted.

The injection of a laser-accelerated ion beam into the SIS18 is the primary long-term goal of the LIGHT collaboration. In this regard, the next steps would be the experimental validation of the simulated beam parameters presented in Chapter 6, as well as the construction of a suitable beamline between the LIGHT beamline and the transfer channel to the SIS18. A first concept for such a beamline has recently been completed.
According to the numerical simulations of this work, the LIGHT beamline should be able to provide proton bunches with 11.4 MeV and an energy spread that is below the acceptance range of the SIS18 $(\Delta E/E = \pm 0.2\,\%)$. Therefore, the implementation of an ion beam diagnostic with a suitable energy resolution at the LIGHT beamline is crucial for an experimental validation. Since the energetic and temporal compression of the transported ion beam with the RF cavity work very similarly, the measurement of the achievable energy spread could also be useful to clarify the reason for the discrepancy between the measured and the simulated temporal ion bunch widths, which have been observed for the temporal compression in the scope of this thesis. Depending on the reason for this discrepancy, it might then be possible to develop concepts that enable ion bunches with temporal widths in the order of 100 ps as predicted by the simulations.

Bibliography

Antici, P., Migliorati, M., Mostacci, A., Picardi, L., Palumbo, L., and Ronsivalle, C. (2011): A compact post-acceleration scheme for laser-generated protons. Physics of Plasmas, **18**(7):073103. URL: http://dx.doi.org/10.1063/1.3574361.

Apiñaniz, J. I., Malko, S., Fedosejevs, R., Cayzac, W., Vaisseau, X., de Luis, D., Gatti, G., McGuffey, C., Bailly-Grandvaux, M., Bhutwala, K., Ospina-Bohorquez, V., Balboa, J., Santos, J. J., Batani, D., Beg, F., Roso, L., Perez-Hernandez, J. A., and Volpe, L. (2021): A quasi-monoenergetic short time duration compact proton source for probing high energy density states of matter. Scientific Reports, **11**(1):1–11. URL: http://dx.doi.org/10.1038/s41598-021-86234-x.

Bagnoud, V., Aurand, B., Blazevic, A., Borneis, S., Bruske, C., Ecker, B., Eisenbarth, U., Fils, J., Frank, A., Gaul, E., Goette, S., Haefner, C., Hahn, T., Harres, K., Heuck, H. M., Hochhaus, D., Hoffmann, D. H., Javorková, D., Kluge, H. J., Kuehl, T., Kunzer, S., Kreutz, M., Merz-Mantwill, T., Neumayer, P., Onkels, E., Reemts, D., Rosmej, O., Roth, M., Stoehlker, T., Tauschwitz, A., Zielbauer, B., Zimmer, D., and Witte, K. (2010): Commissioning and early experiments of the PHELIX facility. Applied Physics B: Lasers and Optics, **100**(1):137–150. URL: http://dx.doi.org/10.1007/S00340-009-3855-7.

Brack, F. E., Kroll, F., Gaus, L., Bernert, C., Beyreuther, E., Cowan, T. E., Karsch, L., Kraft, S., Kunz-Schughart, L. A., Lessmann, E., Metzkes-Ng, J., Obst-Huebl, L., Pawelke, J., Rehwald, M., Schlenvoigt, H. P., Schramm, U., Sobiella, M., Szabó, E. R., Ziegler, T., and Zeil, K. (2020): Spectral and spatial shaping of laser-driven proton beams using a pulsed high-field magnet beamline. Scientific Reports, **10**(1):1–12. URL: http://dx.doi.org/10.1038/s41598-020-65775-7.

Busold, S. (2014): Construction and characterization of a laser-driven proton beamline at GSI. Ph.D. thesis, Technische Universität Darmstadt. URL: http://tuprints.ulb.tu-darmstadt.de/3932/.

Busold, S., Almomani, A., Bagnoud, V., Barth, W., Bedacht, S., Blažević, A., Boine-Frankenheim, O., Brabetz, C., Burris-Mog, T., Cowan, T. E., Deppert, O., Droba, M., Eickhoff, H., Eisenbarth, U., Harres, K., Hoffmeister, G., Hofmann, I., Jaeckel, O., Jaeger, R., Joost, M., Kraft, S., Kroll, F., Kaluza, M., Kester, O., Lecz, Z., Merz, T., Nürnberg, F., Al-Omari, H., Orzhekhovskaya, A., Paulus, G., Polz, J., Ratzinger, U., Roth, M., Schaumann, G., Schmidt, P., Schramm, U., Schreiber, G., Schumacher, D., Stoehlker, T., Tauschwitz, A., Vinzenz, W., Wagner, F., Yaramyshev, S., and Zielbauer, B. (2014a): Shaping laser accelerated ions for future applications – The LIGHT collaboration. Nuclear Instruments and Methods in Physics Research Section A: Accelerators, Spectrometers, Detectors and Associated Equipment, **740**:94–98. URL: http://dx.doi.org/10.1016/J.NIMA.2013.10.025.

Busold, S., Schumacher, D., Brabetz, C., Jahn, D., Kroll, F., Deppert, O., Schramm, U., Cowan, T. E., Blažević, A., Bagnoud, V., and Roth, M. (2015): Towards highest peak intensities for ultra-short MeV-range ion bunches. Scientific Reports, **5**(August). URL: http://dx.doi.org/10.1038/srep12459.

Busold, S., Schumacher, D., Deppert, O., Brabetz, C., Frydrych, S., Kroll, F., Joost, M., Al-Omari, H., Blažević, A., Zielbauer, B., Hofmann, I., Bagnoud, V., Cowan, T. E., and Roth, M. (2013): Focusing and transport of high-intensity multi-MeV proton bunches from a compact laser-driven source. Physical Review Special Topics - Accelerators and Beams, **16**(10). URL: http://dx.doi.org/10.1103/PhysRevSTAB.16.101302.

Busold, S., Schumacher, D., Deppert, O., Brabetz, C., Kroll, F., Blažević, A., Bagnoud, V., and Roth, M. (2014b): Commissioning of a compact laser-based proton beam line for high intensity bunches around 10 MeV. Phys. Rev. ST Accel. Beams, **17**(3):31302. URL: http://dx.doi.org/10.1103/PhysRevSTAB.17.031302.

Callahan-Miller, D. A. and Tabak, M. (2000): Progress in target physics and design for heavy ion fusion. Physics of Plasmas, **7**(5):2083. URL: http://dx.doi.org/10.1063/1.874031.

Cayzac, W., Frank, A., Ortner, A., Bagnoud, V., Basko, M. M., Bedacht, S., Bläser, C., Blažević, A., Busold, S., Deppert, O., Ding, J., Ehret, M., Fiala, P., Frydrych, S., Gericke, D. O., Hallo, L., Helfrich, J., Jahn, D., Kjartansson, E., Knetsch, A., Kraus, D., Malka, G., Neumann, N. W., Pépitone, K., Pepler, D., Sander, S., Schaumann, G., Schlegel, T., Schroeter, N., Schumacher, D., Seibert, M., Tauschwitz, A., Vorberger, J., Wagner, F., Weih, S., Zobus, Y., and Roth, M. (2017): Experimental discrimination of ion stopping models near the Bragg peak in highly ionized matter. Nature Communications, **8**(June). URL: http://dx.doi.org/10.1038/ncomms15693.

Chen, Y.-J. (2003): Final Focus Spot Size in a Solenoid Focusing System. URL: http://dx.doi.org/10.2172/15003857.

Cirrone, G. A., Petringa, G., Catalano, R., Schillaci, F., Allegra, L., Amato, A., Avolio, R., Costa, M., Cuttone, G., Fajstavr, A., Gallo, G., Giuffrida, L., Guarrera, M., Korn, G., Larosa, G., Leanza, R., Lo Vecchio, E., Messina, G., Milluzzo, G., Olsovcova, V., Pulvirenti, S., Pipek, J., Romano, F., Rizzo, D., Russo, A. D., Salamone, S., Scuderi, V., Velyhan, A., Vinciguerra, S., Zakova, M., Zappalà, E., and Margarone, D. (2020): ELIMED-ELIMAIA: The First Open User Irradiation Beamline for Laser-Plasma-Accelerated Ion Beams. Frontiers in Physics, **8**(November 2020):1–8. URL: http://dx.doi.org/10.3389/fphy.2020.564907.

Clark, E. L., Krushelnick, K., Davies, J. R., Zepf, M., Tatarakis, M., Beg, F. N., Machacek, A., Norreys, P. A., Santala, M. I., Watts, I., and Dangor, A. E. (2000): Measurements of Energetic Proton Transport through Magnetized Plasma from Intense Laser Interactions with Solids. Physical Review Letters, **84**(4):670. URL: http://dx.doi.org/10.1103/PhysRevLett.84.670.

Cowan, T. E., Fuchs, J., Ruhl, H., Kemp, A., Audebert, P., Roth, M., Stephens, R., Barton, I., Blazevic, A., Brambrink, E., Cobble, J., Fernández, J., Gauthier, J. C., Geissel, M., Hegelich, M., Kaae, J., Karsch, S., Le Sage, G. P., Letzring, S., Manclossi, M., Meyroneinc, S., Newkirk, A., Pépin, H., and Renard-LeGalloudec, N. (2004): Ultralow emittance, multi-MeV proton beams from a laser virtual-cathode plasma accelerator. Physical Review Letters, **92**(20):1–4. URL: http://dx.doi.org/10.1103/PhysRevLett.92.204801.

Daido, H., Nishiuchi, M., and Pirozhkov, A. S. (2012): Review of laser-driven ion sources and their applications. Reports on Progress in Physics, **75**(5):056401. URL: http://dx.doi.org/10.1088/0034-4885/75/5/056401.

Demtröder, W. (2013): Experimentalphysik 2. Springer-Lehrbuch. Springer Berlin Heidelberg, Berlin, Heidelberg. ISBN 978-3-642-29943-8. URL: http://dx.doi.org/10.1007/978-3-642-29944-5.

Devroye, L. (1986): Non-Uniform Random Variate Generation. Springer New York. URL: http://dx.doi.org/10.1007/978-1-4613-8643-8.

Ding, J. (2018): Generation, Handling and Transport of Laser-Driven Heavy Ion Beams. Ph.D. thesis, Technische Universität Darmstadt. URL: http://tuprints.ulb.tu-darmstadt.de/8214/.

Ding, J., Schumacher, D., Jahn, D., Blažević, A., and Roth, M. (2018): Simulation studies on generation, handling and transport of laser-accelerated carbon ions. Nuclear Instruments and Methods in Physics Research, Section A: Accelerators, Spectrometers, Detectors and Associated Equipment, **909**:168–172. URL: http://dx.doi.org/10.1016/j.nima.2018.02.103.

Dormand, J. R. and Prince, P. J. (1978): New Runge-Kutta algorithms for numerical simulation in dynamical astronomy. Celestial mechanics, **18**(3):223–232. URL: http://dx.doi.org/10.1007/BF01230162.

Dormand, J. R. and Prince, P. J. (1980): A family of embedded Runge-Kutta formulae. Journal of Computational and Applied Mathematics, **6**(1):19–26. URL: http://dx.doi.org/10.1016/0771-050X(80)90013-3.

Dyer, G. M., Bernstein, A. C., Cho, B. I., Osterholz, J., Grigsby, W., Dalton, A., Shepherd, R., Ping, Y., Chen, H., Widmann, K., and Ditmire, T. (2008): Equation-of-state measurement of dense plasmas heated with fast protons. Physical review letters, **101**(1). URL: http://dx.doi.org/10.1103/PHYSREVLETT.101.015002.

Fernandez, J. C., Albright, B. J., Beg, F. N., Foord, M. E., Hegelich, B. M., Honrubia, J. J., Roth, M., Stephens, R. B., and Yin, L. (2014): Fast ignition with laser-driven proton and ion beams. Nuclear Fusion, **54**(5):054006. URL: http://dx.doi.org/10.1088/0029-5515/54/5/054006.

Gibbon, P. (2005): Short Pulse Laser Interactions with Matter. Imperial College Press. URL: http://dx.doi.org/10.1142/p116.

GSI (2022): GSI SIS18 Injection. URL: https://www.gsi.de/en/work/beschleunigerbetrieb/beschleuniger/unilac/unilac/sis_18_injection. Accessed: 29 October 2022.

Hargrove, L. E., Fork, R. L., and Pollack, M. A. (1964): Locking of He-Ne laser modes induced by synchronous intracavity modulation. Applied Physics Letters, **5**(1):4. URL: http://dx.doi.org/10.1063/1.1754025.

Hatchett, S. P., Brown, C. G., Cowan, T. E., Henry, E. A., Johnson, J. S., Key, M. H., Koch, J. A., Langdon, A. B., Lasinski, B. F., Lee, R. W., Mackinnon, A. J., Pennington, D. M., Perry, M. D., Phillips, T. W., Roth, M., Sangster, T. C., Singh, M. S., Snavely, R. A., Stoyer, M. A., Wilks, S. C., and Yasuike, K. (2000): Electron, photon, and ion beams from the relativistic interaction of Petawatt laser pulses with solid targets. Physics of Plasmas, **7**(5):2076. URL: http://dx.doi.org/10.1063/1.874030.

Häuser, J. (1989): Eigenschaften von Spiralresonatoren. Ph.D. thesis, Universität Frankfurt.

Hegelich, B. M., Albright, B., Audebert, P., Blazevic, A., Brambrink, E., Cobble, J., Cowan, T., Fuchs, J., Gauthier, J. C., Gautier, C., Geissel, M., Habs, D., Johnson, R., Karsch, S., Kemp, A., Letzring, S., Roth, M., Schramm, U., Schreiber, J., Witte, K. J., and Fernández, J. C. (2005): Spectral properties of laser-accelerated mid-Z MeV/u ion beams. Physics of Plasmas, **12**(5):1–5. URL: http://dx.doi.org/10.1063/1.1915350.

Hegelich, M., Karsch, S., Pretzler, G., Habs, D., Witte, K., Guenther, W., Allen, M., Blazevic, A., Fuchs, J., Gauthier, J. C., Geissel, M., Audebert, P., Cowan, T., and Roth, M. (2002): MeV ion jets from short-pulse-laser interaction with thin foils. Physical Review Letters, **89**(8):085002/1–085002/4. URL: http://dx.doi.org/10.1103/PhysRevLett.89.085002.

Hinterberger, F. (2008): Physik der Teilchenbeschleuniger und Ionenoptik. Springer-Verlag. ISBN 9783540752813. URL: http://dx.doi.org/10.1007/978-3-540-75282-0.

Hofmann, I. (2018): Review of accelerator driven heavy ion nuclear fusion. Matter and Radiation at Extremes, **3**(1):1. URL: http://dx.doi.org/10.1016/J.MRE.2017.12.001.

Hughes, J. R. and Parsons, J. L. (2020): FLASH Radiotherapy: Current Knowledge and Future Insights Using Proton-Beam Therapy. International Journal of Molecular Sciences 2020, Vol. 21, Page 6492, **21**(18):6492. URL: http://dx.doi.org/10.3390/IJMS21186492.

Hurricane, O. A., Springer, P. T., Patel, P. K., Callahan, D. A., Baker, K., Casey, D. T., Divol, L., Döppner, T., Hinkel, D. E., Hohenberger, M., Berzak Hopkins, L. F., Jarrott, C., Kritcher, A., Le Pape, S., Maclaren, S., Masse, L., Pak, A., Ralph, J., Thomas, C., Volegov, P., and Zylstra, A. (2019): Approaching a burning plasma on the NIF. Physics of Plasmas, **26**(5):052704. URL: http://dx.doi.org/10.1063/1.5087256.

Jahn, D., Schumacher, D., Brabetz, C., Kroll, F., Brack, F. E., Ding, J., Leonhardt, R., Semmler, I., BlaŽević, A., Schramm, U., and Roth, M. (2019): Focusing of multi-MeV, subnanosecond proton bunches from a laser-driven source. Physical Review Accelerators and Beams, **22**(1):1–6. URL: http://dx.doi.org/10.1103/PhysRevAccelBeams.22.011301.

Jahn, D., Träger, M., Kis, M., Brabetz, C., Schumacher, D., Blaević, A., Ciobanu, M., Pomorski, M., Bonnes, U., Busold, S., Kroll, F., Brack, F. E., Schramm, U., and Roth, M. (2018): Chemical-vapor deposited ultra-fast diamond detectors for temporal measurements of ion bunches. Review of Scientific Instruments, **89**(9). URL: http://dx.doi.org/10.1063/1.5048667.

Kalvas, T. (2014): Beam Extraction and Transport. CAS-CERN Accelerator School: Ion Sources - Proceedings. URL: http://dx.doi.org/10.5170/CERN-2013-007.

Kroll, F. (2018): The Study and Development of Pulsed High-field Magnets for Application in Laser-plasma Physics. Ph.D. thesis, Technische Universität Dresden. URL: https://www.hzdr.de/publications/Publ-28306.

Kroll, F., Brack, F. E., Bernert, C., Bock, S., Bodenstein, E., Brüchner, K., Cowan, T. E., Gaus, L., Gebhardt, R., Helbig, U., Karsch, L., Kluge, T., Kraft, S., Krause, M., Lessmann, E., Masood, U., Meister, S., Metzkes-Ng, J., Nossula, A., Pawelke, J., Pietzsch, J., Püschel, T., Reimold, M., Rehwald, M., Richter, C., Schlenvoigt, H. P., Schramm, U., Umlandt, M. E., Ziegler, T., Zeil, K., and Beyreuther, E. (2022): Tumour irradiation in mice with a laser-accelerated proton beam. Nature Physics 2022 18:3, **18**(3):316–322. URL: http://dx.doi.org/10.1038/s41567-022-01520-3.

Kruer, W. L. (2019): The Physics Of Laser Plasma Interactions. CRC Press. ISBN 9781003003243. URL: http://dx.doi.org/10.1201/9781003003243.

Kumar, V. (2009): Understanding the focusing of charged particle beams in a solenoid magnetic field. American Journal of Physics, **77**(8):737. URL: http://dx.doi.org/10.1119/1.3129242.

Lee, E. P. and Coopert, R. K. (1976): General Envelope Equation For Cylindrically Symmetric Charged Particle Beams. Part. Accel., **7**:83–95. URL: https://cds.cern.ch/record/1107845.

Macchi, A. (2013): A Superintense Laser-Plasma Interaction Theory Primer. Springer Dordrecht. ISBN 978-94-007-6124-7. URL: http://dx.doi.org/10.1007/978-94-007-6125-4.

Macchi, A., Borghesi, M., and Passoni, M. (2013): Ion acceleration by superintense laser-plasma interaction. Reviews of Modern Physics, **85**(2):751. URL: http://dx.doi.org/10.1103/RevModPhys.85.751.

MacKinnon, A. J., Patel, P. K., Borghesi, M., Clarke, R. C., Freeman, R. R., Habara, H., Hatchett, S. P., Hey, D., Hicks, D. G., Kar, S., Key, M. H., King, J. A., Lancaster, K., Neely, D., Nikkro, A., Norreys, P. A., Notley, M. M., Phillips, T. W., Romagnani, L., Snavely, R. A., Stephens, R. B., and Town, R. P. (2006): Proton radiography of a laser-driven implosion. Physical review letters, **97**(4). URL: http://dx.doi.org/10.1103/PHYSREVLETT.97.045001.

Maiman, T. H. (1960): Stimulated Optical Radiation in Ruby. Nature 1960 187:4736, **187**(4736):493–494. URL: http://dx.doi.org/10.1038/187493a0.

Maksimchuk, A., Gu, S., Flippo, K., Umstadter, D., and Bychenkov, A. Y. (2000): Forward Ion Acceleration in Thin Films Driven by a High-Intensity Laser. Physical Review Letters, **84**(18):4108. URL: http://dx.doi.org/10.1103/PhysRevLett.84.4108.

Masood, U., Bussmann, M., Cowan, T. E., Enghardt, W., Karsch, L., Kroll, F., Schramm, U., and Pawelke, J. (2014): A compact solution for ion beam therapy with laser accelerated protons. Applied Physics B: Lasers and Optics, **117**(1):41–52. URL: http://dx.doi.org/10.1007/s00340-014-5796-z.

McClung, F. J. and Hellwarth, R. W. (1962): Giant Optical Pulsations from Ruby. Journal of Applied Physics, **33**(3):828. URL: http://dx.doi.org/10.1063/1.1777174.

McGuffey, C., Kim, J., Wei, M. S., Nilson, P. M., Chen, S. N., Fuchs, J., Fitzsimmons, P., Foord, M. E., Mariscal, D., McLean, H. S., Patel, P. K., Stephens, R. B., and Beg, F. N. (2020): Focussing Protons from a Kilojoule Laser for Intense Beam Heating using Proximal Target Structures. Scientific Reports 2020 10:1, **10**(1):1–10. URL: http://dx.doi.org/10.1038/s41598-020-65554-4.

McLaughlin, W. L., Al-Sheikhly, M., Lewis, D. F., Kovács, A., and Wojnárovits, L. (1996): Radiochromic Solid-State Polymerization Reaction. In Irradiation of Polymers, vol. 620 of *ACS Symposium Series*, pp. 11–152. American Chemical Society. ISBN 9780841233775. URL: http://dx.doi.org/doi:10.1021/bk-1996-0620.ch011.

Metternich, M., Nazary, H., Schumacher, D., Brabetz, C., Kroll, F., Brack, F.-E., Ehret, M., Blažević, A., Schramm, U., Bagnoud, V., and Roth, M. (2022): Analyzing the filamentation of MeV-range proton bunches in a laser-driven ion beamline and optimizing their peak intensity. Physical Review Accelerators and Beams, **25**(11):111301. URL: http://dx.doi.org/10.1103/PhysRevAccelBeams.25.111301.

Mulser, P. and Bauer, D. (2010): High Power Laser-Matter Interaction, vol. 238. ISBN 978-3-540-50669-0. URL: http://dx.doi.org/10.1007/978-3-540-46065-7.

Nürnberg, F. (2010): Laser-Accelerated Proton Beams as a New Particle Source. Ph.D. thesis, Technische Universität Darmstadt. URL: https://tuprints.ulb.tu-darmstadt.de/id/eprint/2339.

Nürnberg, F., Schollmeier, M., Brambrink, E., Blažević, A., Carroll, D. C., Flippo, K., Gautier, D. C., Geibel, M., Harres, K., Hegelich, B. M., Lundh, O., Markey, K., McKenna, P., Neely, D., Schreiber, J., and Roth, M. (2009): Radiochromic film imaging spectroscopy of laser-accelerated proton beams. Review of Scientific Instruments, **80**(3):1–13. URL: http://dx.doi.org/10.1063/1.3086424.

Patel, P. K., Mackinnon, A. J., Key, M. H., Cowan, T. E., Foord, M. E., Allen, M., Price, D. F., Ruhl, H., Springer, P. T., and Stephens, R. (2003): Isochoric heating of solid-density matter with an ultrafast proton beam. Physical Review Letters, **91**(12). URL: http://dx.doi.org/10.1103/PhysRevLett.91.125004.

Pelka, A., Gregori, G., Gericke, D. O., Vorberger, J., Glenzer, S. H., Günther, M. M., Harres, K., Heathcote, R., Kritcher, A. L., Kugland, N. L., Li, B., Makita, M., Mithen, J., Neely, D., Niemann, C., Otten, A., Riley, D., Schaumann, G., Schollmeier, M., Tauschwitz, A., and Roth, M. (2010): Ultrafast melting of carbon induced by intense proton beams. Physical Review Letters, **105**(26):265701. URL: http://dx.doi.org/10.1103/PhysRevLett.105.265701.

Rannacher, R. (2017): Numerik partieller Differentialgleichungen. URL: http://nbn-resolving.de/urn:nbn:de:bsz:16-heiup-book-281-3.

Reiser, M., O'Shea, P., Bernal, S., and Kishek, R. (2008): Theory and Design of Charged Particle Beams: Second Edition. Wiley-VCH. ISBN 9783527407415. URL: http://dx.doi.org/10.1002/9783527622047.

Rösch, T. F., Szabó, Z., Haffa, D., Bin, J., Brunner, S., Englbrecht, F. S., Friedl, A. A., Gao, Y., Hartmann, J., Hilz, P., Kreuzer, C., Lindner, F. H., Ostermayr, T. M., Polanek, R., Speicher, M., Szabó, E. R., Taray, D., Tokés, T., Würl, M., Parodi, K., Hideghéty, K., and Schreiber, J. (2020): A feasibility study of zebrafish embryo irradiation with laser-accelerated protons. Review of Scientific Instruments, **91**(6):063303. URL: http://dx.doi.org/10.1063/5.0008512.

Roth, M., Blazevic, A., Brambrink, E., Geissel, M., Cowan, T. E., Fuchs, J., Kemp, A., Ruhl, H., Audebert, P., Cobble, J., Fernandez, J., Hegelich, M., Letzring, S., Ledingham, K., Mckenna, P., Clarke, R., Neely, D., Karsch, S., Habs, D., and Schreiber, J. (2006): Laser Accelerated, High Quality Ion Beams. Hyperfine Interactions 2006 162:1, **162**(1):45–53. URL: http://dx.doi.org/10.1007/S10751-005-9202-4.

Roth, M., Cowan, T. E., Key, M. H., Hatchett, S. P., Brown, C., Fountain, W., Johnson, J., Pennington, D. M., Snavely, R. A., Wilks, S. C., Yasuike, K., Ruhl, H., Pegoraro, F., Bulanov, S. V., Campbell, E. M., Perry, M. D., and Powell, H. (2001): Fast Ignition by Intense Laser-Accelerated Proton Beams. Physical Review Letters, **86**(3):436. URL: http://dx.doi.org/10.1103/PhysRevLett.86.436.

Roth, M., Jung, D., Falk, K., Guler, N., Deppert, O., Devlin, M., Favalli, A., Fernandez, J., Gautier, D., Geissel, M., Haight, R., Hamilton, C. E., Hegelich, B. M., Johnson, R. P., Merrill, F., Schaumann, G., Schoenberg, K., Schollmeier, M., Shimada, T., Taddeucci, T., Tybo, J. L., Wagner, F., Wender, S. A., Wilde, C. H., and Wurden, G. A. (2013): Bright laser-driven neutron source based on the relativistic transparency of solids. Physical Review Letters, **110**(4):044802. URL: http://dx.doi.org/10.1103/PhysRevLett.110.044802.

Scherzer, O. (1936): Über einige Fehler von Elektronenlinsen. Zeitschrift für Physik 1936 101:9, **101**(9):593–603. URL: http://dx.doi.org/10.1007/BF01349606.

Schmitz, B., Metternich, M., and Boine-Frankenheim, O. (2022): Automated reconstruction of the initial distribution of laser accelerated ion beams from radiochromic film (RCF) stacks. Review of Scientific Instruments, **93**(9):093306. URL: http://dx.doi.org/10.1063/5.0094105.

Schollmeier, M., Geissel, M., Sefkow, A. B., and Flippo, K. A. (2014): Improved spectral data unfolding for radiochromic film imaging spectroscopy of laser-accelerated proton beams. Review of Scientific Instruments, **85**(4):043305. URL: http://dx.doi.org/10.1063/1.4870895.

Schollmeier, M. S. (2009): Optimization and control of laser-accelerated proton beams. Ph.D. thesis, Technische Universität, Darmstadt. URL: http://tuprints.ulb.tu-darmstadt.de/1232/.

Schüller, A., Heinrich, S., Fouillade, C., Subiel, A., De Marzi, L., Romano, F., Peier, P., Trachsel, M., Fleta, C., Kranzer, R., Caresana, M., Salvador, S., Busold, S., Schönfeld, A., McEwen, M., Gomez, F., Solc, J., Bailat, C., Linhart, V., Jakubek, J., Pawelke, J., Borghesi, M., Kapsch, R. P., Knyziak, A., Boso, A., Olsovcova, V., Kottler, C., Poppinga, D., Ambrozova, I., Schmitzer, C. S., Rossomme, S., and Vozenin, M. C. (2020): The European Joint Research Project UHDpulse – Metrology for advanced radiotherapy using particle beams with ultra-high pulse dose rates. Physica Medica, **80**:134–150. URL: http://dx.doi.org/10.1016/J.EJMP.2020.09.020.

Shampine, L. F. and Reichelt, M. W. (1997): The MATLAB ODE Suite. SIAM Journal of Scientific Computing, **18**(1):1–22. URL: http://dx.doi.org/10.1137/S1064827594276424.

Sharkov, B. Y., Hoffmann, D. H., Golubev, A. A., and Zhao, Y. (2018): High energy density physics with intense ion beams. Matter and Radiation at Extremes, **1**(1):28. URL: http://dx.doi.org/10.1016/J.MRE.2016.01.002.

Snavely, R. A., Key, M. H., Hatchett, S. P., Cowan, I. E., Roth, M., Phillips, T. W., Stoyer, M. A., Henry, E. A., Sangster, T. C., Singh, M. S., Wilks, S. C., MacKinnon, A., Offenberger, A., Pennington, D. M., Yasuike, K., Langdon, A. B., Lasinski, B. F., Johnson, J., Perry, M. D., and Campbell, E. M. (2000): Intense High-Energy Proton Beams from Petawatt-Laser Irradiation of Solids. Physical Review Letters, **85**(14):2945. URL: http://dx.doi.org/10.1103/PhysRevLett.85.2945.

Snavely, R. A., Zhang, B., Akli, K., Chen, Z., Freeman, R. R., Gu, P., Hatchett, S. P., Hey, D., Hill, J., Key, M. H., Izawa, Y., King, J., Kitagawa, Y., Kodama, R., Langdon, A. B., Lasinski, B. F., Lei, A., MacKinnon, A. J., Patel, P., Stephens, R., Tampo, M., Tanaka, K. A., Town, R., Toyama, Y., Tsutsumi, T., Wilks, S. C., Yabuuchi, T., and Zheng, J. (2007): Laser generated proton beam focusing and high temperature isochoric heating of solid matter. Physics of Plasmas, **14**(9):092703. URL: http://dx.doi.org/10.1063/1.2774001.

Strickland, D. and Mourou, G. (1985): Compression of amplified chirped optical pulses. Optics Communications, **55**(6):447–449. URL: http://dx.doi.org/10.1016/0030-4018(85)90151-8.

Volpe, L., Batani, D., Vauzour, B., Nicolai, P., Santos, J. J., Regan, C., Morace, A., Dorchies, F., Fourment, C., Hulin, S., Perez, F., Baton, S., Lancaster, K., Galimberti, M., Heathcote, R., Tolley, M., Spindloe, C., Koester, P., Labate, L., Gizzi, L. A., Benedetti, C., Sgattoni, A., Richetta, M., Pasley, J., Beg, F., Chawla, S., Higginson, D. P., and MacPhee, A. G. (2011): Proton radiography of laser-driven imploding target in cylindrical geometry. Physics of Plasmas, **18**(1):012704. URL: http://dx.doi.org/10.1063/1.3530596.

Wilks, S. C., Langdon, A. B., Cowan, T. E., Roth, M., Singh, M., Hatchett, S., Key, M. H., Pennington, D., MacKinnon, A., and Snavely, R. A. (2001): Energetic proton generation in ultra-intense laser–solid interactions. Physics of Plasmas, **8**(2):542. URL: http://dx.doi.org/10.1063/1.1333697.

Wille, K. (1996): Physik der Teilchenbeschleuniger und Synchrotronstrahlungsquellen. Vieweg+Teubner Verlag. ISBN 978-3-519-13087-1. URL: http://dx.doi.org/10.1007/978-3-663-11039-2.

Zhu, J. G., Wu, M. J., Zhu, K., Geng, Y. X., Liao, Q., Li, D. Y., Yang, T., Easton, M. J., Li, C. C., Xu, X. H., Shou, Y. R., Yu, J. Q., Gong, Z., Zhao, Y. Y., Wang, P. J., Wang, D. H., Tao, L., Chen, C. E., Ma, W. J., Lu, H. Y., Tajima, T., Mourou, G., Lin, C., and Yan, X. Q. (2020): Demonstration of tailored energy deposition in a laser proton accelerator. Physical Review Accelerators and Beams, **23**(12):1–9. URL: http://dx.doi.org/10.1103/PhysRevAccelBeams.23.121304.

Ziegler, J. F. and Biersack, J. P. (1985): The Stopping and Range of Ions in Matter. Springer, Boston, MA. URL: http://dx.doi.org/10.1007/978-1-4615-8103-1_3.

Zylstra, A. B. and Hurricane, O. A. (2019): On alpha-particle transport in inertial fusion. Physics of Plasmas, **26**(6):062701. URL: http://dx.doi.org/10.1063/1.5101074.

Acknowledgements

An dieser Stelle möchte ich gerne allen Personen danken, die mich während meiner Promotion unterstützt und begleitet haben. Ohne sie wäre diese Arbeit nicht möglich gewesen.

Zunächst möchte ich meinem Doktorvater Prof. Markus Roth danken, der mich in seiner Forschungsgruppe aufnahm und mir die Möglichkeit gab, am LIGHT Projekt zu promovieren. Vielen Dank für dein Vertrauen und für diese spannende und lehrreiche Zeit!

Des Weiteren möchte ich mich bei Prof. Vincent Bagnoud bedanken, für seine Unterstützung, seine Ratschläge und nicht zuletzt für seine Bereitschaft diese Arbeit als Koreferent zu begutachten. Ich hoffe, dass du trotzdem noch Zeit für die ein oder andere Abfahrt in Hirschegg findest.

Ein außerordentlicher Dank geht an Dennis Schumacher, Abel Blažević und Haress Nazary. Die alltägliche Zusammenarbeit mit euch hat mir großen Spaß bereitet und ohne euch wäre diese Arbeit in der Form nicht zustande gekommen. Dennis, an dieser Stelle noch einmal ein ganz besonderer Dank an dich, dass du dir stets die Zeit für mich genommen hast, um über physikalische und technische Fragen zu diskutieren.

Des Weiteren möchte ich Christian Brabetz, Florian Kroll und Florian Brack für die Bereitstellung von jeglichem Equipment, die große Unterstützung bei den Experimenten und die hilfreichen Ratschläge zu meiner ersten Veröffentlichung danken.
Unverzichtbar für diese Experimente war das Lasersystem PHELIX und dessen Mitarbeiter. Vielen Dank für eure stetige Bereitschaft, insbesondere für den 30-45 minütigen Schussmodus!
Ich danke ebenfalls Torsten Abel und Bettina Lommel für die Herstellung der Targets sowie Holger Risch für das Aufkleben der Streufolien.

Ein weiterer Dank geht an Diana Lang für jegliche Hilfe in Sachen Organisation, Einkauf und Versand; an Dirk Reemts für die Beratung bei der Anfertigung meiner fragwürdigen Konstruktionen und den Aufbau der Verstärker an *nhelix*; sowie an Udo Eisenbarth für die Unterstützung bei der Planung des *nhelix* Upgrades.

Ebenso danke ich Sarah Grimm, Kenneth Jähner und Finn Neufeld, die im Rahmen ihrer Bachelor- und Masterarbeiten viele Aufgaben übernommen und mit Bravour gemeistert haben.

Auch wenn aufgrund der Pandemie das gesellige Beisammensein auf einmal nicht mehr möglich war, möchte ich dennoch meinen Kollegen Yannik Zobus und Jonas Ohland danken, die mich im gemeinsamen Büro stets bei Laune gehalten haben und auch immer für Diskussionen zur Verfügung standen. Ich hoffe, dass in diesem Büro bald wieder der alltägliche Wahnsinn einkehrt.

Weiterhin möchte ich auch meiner Studienclique mit Yannik, Markus, Felix, Phillip, Patrick, Max und Sascha danken. Ihr habt mir während meines Grundstudiums unglaublich geholfen am Ball zu bleiben und die durchzechten Nächte - nach diversen, vermeintlich gut gelaufenen Prüfungen - werde ich nie vergessen. Ich bin froh, dass wir es nach wie vor irgendwie schaffen den Kontakt zu halten und hoffe, dass wir unsere jährlichen Treffen noch lange beibehalten werden. Markus, dir an dieser Stelle auch nochmal vielen Dank für deine wenigen, aber hilfreichen Kommentaren sowie für die aufbauenden Worte zu dieser Arbeit.

Liebe Freunde aus der Heimat, allen voran Anton, Basti, Conny, Lars, Marcel und Sascha: Ihr begleitet mich schon mein Leben lang und schafft es stets mich auf andere Gedanken zu bringen. Danke, dass ich mich immer auf euch verlassen kann.

Einen großen Anteil an meinem Weg bis hierher hat selbstverständlich auch meine Familie, meine Eltern Bernd und Andrea sowie mein Bruder Patrick. Ihr habt mich immer unterstützt und gefördert, wo es euch möglich war. Vielen Dank dafür!

Eva, ich bin so glücklich, dich an meiner Seite zu haben. Für deine alltägliche Unterstützung in sämtlichen Lebenslagen und deine verständnisvolle, nicht-nachtragende Art kann ich dir gar nicht genug danken. Vor allem in letzter Zeit hast du mich stets ermutigt und mir den Rücken frei gehalten. Ich danke dir von ganzem Herzen.

A. Appendix

A.1. Influence of the initial beam parameters on the simulation studies

In the simulation studies of this work, the TNSA-generated ion beam was reconstructed with the following parameters (see Section 2.3):

- The maximum energy (cut-off energy) of the TNSA spectrum E_{cut} and its decaying constant $k_{\text{B}}T$
- The scaling parameters for the maximum divergence a_2, a_1 and a_0
- The maximum micro divergence $\Delta\theta_{\text{max}}$ and the start delay Δt_{max}
- The maximum and minimum source size r_{max} and r_{min}

The parameters E_{cut}, $k_{\text{B}}T$, a_2, a_1 and a_0 influence the initial energy and divergence distribution of the particles and can be determined by fits to RIS measurements. Since many simulations in this work were performed prior to the evaluation of RIS measurements shown in Section 2.2, the parameters E_{cut}, $k_{\text{B}}T$, a_2, a_1, and a_0 in these simulations are taken from a TNSA source characterization presented in [Busold, 2014].

The parameters $\Delta\theta_{\text{max}}$, Δt_{max}, r_{min} and r_{max} change the emittance of the ion beam. According to [Cowan et al., 2004] and [Nürnberg et al., 2009] the emittance of TNSA-generated ion beams is very low. For this reason the initial emittance has been neglected in the simulations of this work by setting $\Delta\theta_{\text{max}}$ and Δt_{max} to zero.

Therefore, in the following it will be investigated to what extent a change of these parameters has an influence on the simulation studies of this work. For this purpose, the simulations of Section 7.1 are performed again with the initial beam parameters determined in Section 2.2 (see Table 2.1) and different initial emittances $\varepsilon_{rr'}, \varepsilon_{tE}$ $(r = x \cup y, r' = x' \cup y')$. Thereby, the setup of the LIGHT beamline, the phase and voltage of the RF cavity, and the currents supplied to the solenoid magnets were identical to those used in Section 7.1. The results are shown in Table A.1.

In [Cowan et al., 2004] a longitudinal emittance of $\varepsilon_{tE}^{3\sigma} < 10^{-4}\,\mathrm{eV\,s}$ and a transverse emittance of $\varepsilon_{n,rr'}^{2\sigma} = 0.016\,\mathrm{mm\,mrad}$ are specified for TNSA generated ion beams and in [Nürnberg et al., 2009] the maximum transverse emittance for protons with around 8 MeV is $\varepsilon_{n,rr'}^{2\sigma} = 0.2\,\mathrm{mm\,mrad}$. As can be seen, for these values (marked in yellow) the influence of the initial emittance on the resulting beam parameters is negligible. In this initial emittance range the results are also consistent with those of Section 7.1 (see Table 7.2), thus the deviation of the initial beam parameters specified in [Busold, 2014] and in Section 2.2 are also negligible.

Table A.1: Parameters of the temporal compressed and focused proton beam for different initial emittances $\varepsilon^{2\sigma}_{rr'}$ and $\varepsilon^{3\sigma}_{tE}$. Thereby, τ is the temporal bunch width and r_0 the radius of the focal spot. The initial emittances in the yellow highlighted row are expected for a TNSA-generated ion beam according to [Cowan et al., 2004] and [Nürnberg et al., 2009].

$\varepsilon^{2\sigma}_{n,rr'}$	$\varepsilon^{3\sigma}_{tE}$	E	$\Delta E/E$	τ (FWHM)	r_0 (50 % of protons)
0 mm mrad	0 eV s	7.7 MeV	4.4 %	70 ps	0.69 mm
0.2 mm mrad	10^{-4} eV s	7.7 MeV	4.4 %	70 ps	0.69 mm
2 mm mrad	10^{-3} eV s	7.7 MeV	4.4 %	160 ps	0.68 mm
10 mm mrad	5×10^{-3} eV s	7.7 MeV	4.93 %	700 ps	0.67 mm
30 mm mrad	10^{-2} eV s	7.7 MeV	5.97 %	1.46 ns	0.74 mm

A.2. Influence of a radially dependent energy transfer of the RF cavity on longitudinal beam shaping

In the simulation studies of this work, the electric field within the gaps of the RF cavity was assumed to be spatially constant. In the following, the influence of a more complex electric field distribution on the temporal compression is investigated with simulations. For this purpose, the electric field distribution within the gap is determined for a simplified, stationary charge distribution which will be explained in the following.

For the moment at which the standing wave has its maximum in the RF cavity there is an excess of electrons at the end of one drift tube, whereas at the end of the opposite drift tube there is an electron deficiency at this moment. Within the drift tube the electric field that is caused by this charge distribution counteracts the electric field within the RF cavity and in the gap they add up. It is now assumed that the electric field in the gap is only caused by the electron excess and the electron deficiency at the end of the drift tubes, so the electric field of the standing wave in the RF cavity is neglected. This can be considered as the worst-case scenario, since it can be assumed that the standing wave in the RF cavity is spatially constant in the gap, which would therefore reduce the relative radial dependence of the electric field. The used charge distribution for the middle gap of the RF cavity is shown in Fig. A.1.

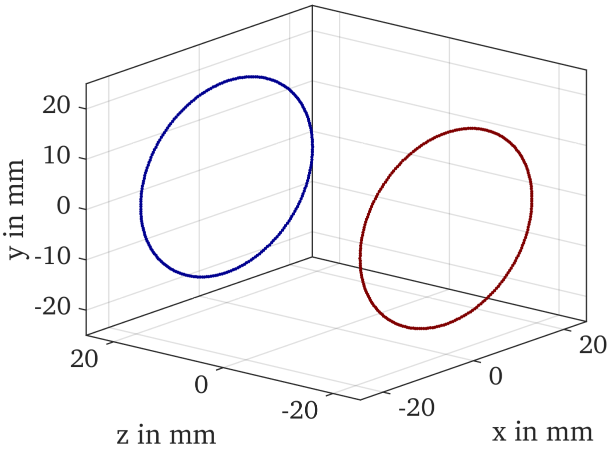

Fig. A.1: Charge distribution that is used to determine the electric field distribution within the middle gap of the RF cavity.

The electric field of this charge distribution is determined by Coulomb's law [Demtröder, 2013]:

$$\mathbf{E}(\mathbf{r}) = \frac{1}{4\pi\epsilon_0} \sum_i^N q_i \frac{\mathbf{r} - \mathbf{r_i}}{|\mathbf{r} - \mathbf{r_i}|^3}. \tag{A.1}$$

Thereby, r_i are the positions of the charges q_i. In the left image of Fig. A.2 the resulting electric field in z-direction E_z is shown in the y-z plane.

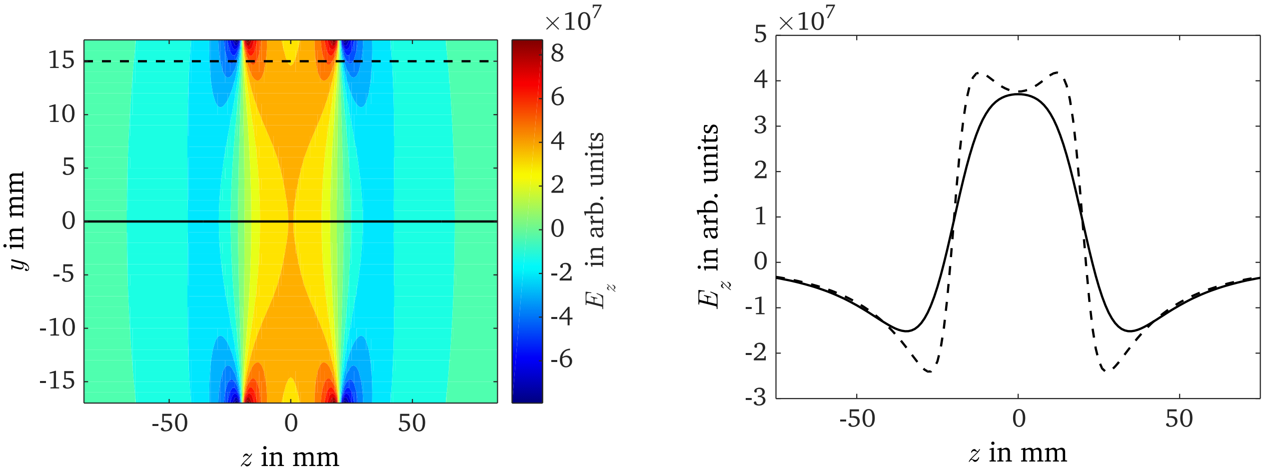

Fig. A.2: The left image shows the electric field E_z determined with the charge distribution shown in Fig. A.1, and the right image shows the electric field E_z plotted along the paths indicated by the black lines in the left image.

As can be seen, in the gap ($z = \pm 20\,\mathrm{mm}$) is a positive electric field whereas in front and behind the gap are small regions in which the electric field is negative. The difference between the electric field in and just outside the gap is larger for a greater radial distance (see right image of Fig. A.2). However, the energy transfer of the electric field to a particle

$$\Delta E_{\text{gap}}(r) = \int_{-\infty}^{\infty} E_z(r, z)\, dz \tag{A.2}$$

is always positive within the aperture of the drift tubes and the deviation between $\Delta E_{\text{gap}}(r_1)$ and $\Delta E_{\text{gap}}(r_2)$ with $r_1 = 0$ and $r_2 = 17.5\,\mathrm{mm}$ is only 5 % as shown in Fig. A.3.

Therefore, for particles whose velocity does not change significantly in the RF cavity, the radial dependence of the energy transfer can be taken into account in the simulation by adjusting the electric field strengths of the gaps $E_{z,\text{gap},i}$ (see Equation 5.27) as follows:

$$\begin{aligned}
E_{z,\text{gap1}} &= E_{z,0} \cdot (1 - 0.7\xi r^2) \cdot \cos(\omega \cdot t + \phi) \\
E_{z,\text{gap2}} &= E_{z,0} \cdot (1 - \xi r^2) \cdot \cos(\omega \cdot t + \phi + \pi) \\
E_{z,\text{gap3}} &= E_{z,0} \cdot (1 - 0.7\xi r^2) \cdot \cos(\omega \cdot t + \phi)
\end{aligned} \tag{A.3}$$

The scaling factor ξ as well as the factor of 0.7 in Equations A.3 can be determined by parabolic fits to $\Delta E_{\text{gap}}(r)/\Delta E_{\text{gap}}(0)$. For the graph in Fig. A.3 it is $\xi = 182\,\mathrm{m}^{-2}$.

To investigate to what extent a radial dependence of the electric field in the gaps has an influence on the simulation studies of this work, the simulations of Section 7.1 were performed again for different values of

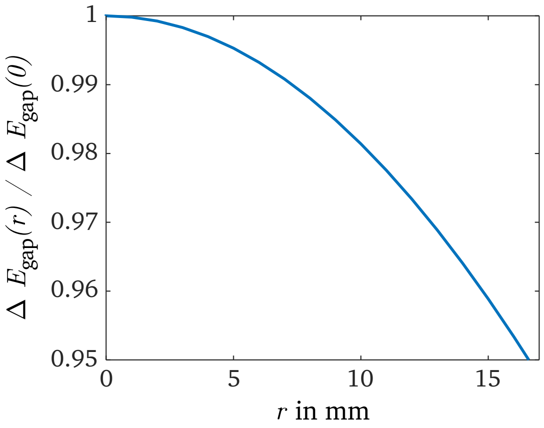

Fig. A.3: Relative energy transfer of the electric field shown in the left image of Fig. A.2 to a particle that has passed the field along the z-direction with a constant distance r to the nominal axis (z-axis).

the scaling factor ξ. Thereby, the setup of the LIGHT beamline, the phase and voltage of the RF cavity, and the currents supplied to the solenoid magnets were identical to those used in Section 7.1. The only beam parameter that changed for a higher ξ is the temporal width of the bunch. The corresponding temporal bunch widths are shown in Table A.2.

Table A.2: Resulting temporal bunch width τ of a temporal compressed proton beam with 7.7 MeV for different radial scaling factors ξ of the electric field in the gaps of the RF cavity. The radial distance r_2 corresponds to the radius of the aperture of the RF cavity (17.5 mm). The yellow row corresponds to the ξ that was determined for the electric field shown in the left image of Fig. A.2.

ξ	$\Delta E/E$ (full width)	τ (FWHM)
0	0	60 ps
$182\,\mathrm{m}^{-2}$	5 %	60 ps
$1000\,\mathrm{m}^{-2}$	25 %	75 ps
$2000\,\mathrm{m}^{-2}$	50 %	150 ps

As can be seen, the temporal bunch width only changes for $\xi > 1000\,\mathrm{m}^{-2}$ and for $\xi = 182\,\mathrm{m}^{-2}$ (yellow row) as derived for the determined electric field distribution in the beginning of this appendix, the effect of the radial dependency of the electric field on the temporal bunch width can be neglected.